Exploring the Electrocatalytic Reduction of Water and Aqueous Nitrite with Water-Soluble, Earth Abundant Metal Complexes and Attempts at Developing an "Electrophotocatalytic" Method for the Reduction of CO_2

By **Jonathan Ferguson**

A thesis submitted in partial fulfillment of the requirements for the degree of Master of Science in Chemistry

Department of Chemistry and Biomolecular Sciences

Faculty of Science

University of Ottawa

Acknowledgements

I would first like to thank my supervisor Dr. Darrin Richeson for giving me this unforgettable experience to grow as a scientist. Thank you for the mentorship and guidance you have given me over the past few years. I have genuinely enjoyed my time in your lab and will always look at my time here as priceless. I couldn't have asked for a better mentor.

Special thanks go out to the amazing friends I've made over the course of my academic career: SN, JB, SO, VM, PB, HC, and AY thank you for the time we've spent together and the memories we share. To AQ, PC, and MV – you have been there for me to pick me up from my lowest points and instill motivation and confidence when I've needed it most; Thank you for the love and kindness you have never stopped giving to me since we've crossed paths. To all of my friends, I am so happy to have met you all and to have the pleasure of forming such strong bonds with each of you.

To my family, notably my mother, who's love and kindness has never stopped touching my heart, I owe you everything for the opportunity and support to pursue what I want from this journey, for that I will always be grateful.

To the Richeson lab, I will miss you! Thank you for the conversations and home baked goods we've indulged in, the failures we've endured, and the victories we've shared. I am happy to call this group mine. And lastly, thank you to Dr. Wendy Pell and her team at the undergraduate teaching lab for their expert guidance and for allowing me to use their equipment when needed.

Abstract

The importance of addressing environmental issues such as lowering the emission of greenhouse gases, preventing eutrophication of aquatic life due to high concetrations of nitrogen oxyanions, and producing sustainable energy is at an all-time high. With a concentration on employing earth abundant metals, a Mn(I) complex was synthesized with an integrated photocatalyst in an attempt at developing a new electrophotocatalytic system. Additionally, a Ni(II) pincer complex was synthesized and structurally and computationally characterized as well as observed to perform electrocatalytic hydrogen generation in water. Lastly, with inspiration from the Ni(II) pincer complex, two macrocyclic complexes, one with a Ni(II) center and the other with a Co(II) center, were structurally characterized and observed to electrocatalytically reduce aqueous nitrite at neutral pH. DFT calculations were also performed to elucidate the nitrite reduction reaction mechanism.

Table of Contents

List of Figures

Chapter 1: Introduction

Chapter 2: Attempts at Developing an "Electrophotocatalytic" System

Chapter 3: Electrocatalytic Hydrogen Production in Neutral Water using an Aqueous Ni(II) pincer complex

Chapter 4: Reduction of Nitrite with Earth Abundant Water Soluble Molecular Electrocatalysts

List of Schemes

Chapter 2: Attempts at Developing an "Electrophotocatalytic" System

Chapter 3: Electrocatalytic Hydrogen Production in Neutral Water using an Aqueous Ni(II) pincer complex

Chapter 4: Reduction of Nitrite with Earth Abundant Water Soluble Molecular Electrocatalysts

List of Tables

Chapter 1: Introduction

Chapter 2: Attempts at Developing an "Electrophotocatalytic" System

Chapter 3: Electrocatalytic Hydrogen Production in Neutral Water using an Aqueous Ni(II) pincer complex

Chapter 4: Reduction of Nitrite with Earth Abundant Water-Soluble Molecular Electrocatalysts

List of Abbreviations

CPC	Controlled Potential Coulometry
CV	Cyclic Voltammetry
DFT	Density Functional Theory
E^o	Potential
$E_{1/2}$	Half-Wave Potential
SOMO	Singly Occupied Molecular Orbital
HOMO	Highest Occupied Molecular Orbital
LUMO	Lowest Unoccopied Molecular Orbital
MET	Multiple Electron Transfer
MHz	Mega Hertz
M	Molar
mM	Millimolar
NMR	Nuclear Magnetic Resonance
PCET	Proton Coupled Electron Transfer
Ppm	Parts per million
SED	Sacrificial Electron Donor
SET	Single Electron Tranfer
SCE	Standard Calomel Electrode
TEA	Triethylamine
UV	Ultraviolet Light
X	Halogen

Chapter 1: Introduction

Motivation:

With society's energy demands dramatically increasing over the past few decades, there has been an upward spike in waste production, greenhouse gas emissions, and human-made nitrogen resulting from the industrialization of chemical processes in order to meet these needs. Two problems in particular that garner widespread attention across the globe are the emission of CO_2, a thermodynamically stable greenhouse gas that contributes to global warming, and excess nitrogen from fertilizer runoff which can form nitrates and nitrites that pollute waterways and contribute to an increase in an excess of nitrogen in the global nitrogen cycle.[1-4] Because of this, there has been widespread efforts to develop methods of mitigating and reversing the damage done to the Earth's environment because of these industrial chemical processes.[5-9] Due to the thermodynamic stability of both CO_2 and NO_2^-, scientists have looked towards the development of innovative catalytic systems to reduce these environmentally hazardous chemicals into useful products.[7-11]

CO_2 as a Greenhouse Gas & Its Reduction

The Earth faces a dangerous problem as the monumental amount of CO_2 emitted into the atmosphere increases along with the further acidification of oceans due to them being one of the largest sinks of atmospheric CO_2 on Earth. Competition for the depleting fossil fuel reserves is also only increasing leading to a one of the world's largest sources of energy becoming increasingly expensive, and eventually unattainable.[12,13] In contrast, CO_2 does have the potential to be an abundant and renewable C1 feedstock with a variety of applications. Thus, the catalytic conversion of this thermodynamically stable compound to useful fuels has the potential to

balance the amount of CO_2 across the globe and provide an avenue for further scientific innovation.

The reduction pathway of CO_2 has many endpoints, most commonly, CO_2 reduction reactions end in the production of carbon monoxide (CO), methanol, formaldehyde, and formic acid (HCOOH).[14] Due to the extremely strong C=O bond, with a bond energy of 750 kJ/mol, the reduction of this abundant yet thermodynamically stable compound is known to be challenging. The use of electrochemical reduction to pursue the one electron reduction of CO_2 to CO_2^- boasts a potential of -2.14 V (vs SCE) which is not a favourable route. Other methods of CO_2 reduction employ the use of a proton donor to assist with multiple electron transfer (MET) reactions. From the table below, the use of a proton donor for MET is more favourable with respect to the previous pathway.[15-17]

Table 1: Reduction Potentials of Common CO_2 Reduction Reactions (CO_2RR)

CO_2RR Scheme	Reduction Potential for MET (E^o (V vs SCE))
$CO_2 + 2H^+ + 2e^- \rightarrow CO + H_2O$	-0.77 V
$CO2 + 8H^+ + 8e^- \rightarrow CH_4 + 2H_2O$	-0.48 V
$CO_2 + 2H^+ + 2e^- \rightarrow HCOOH$	-0.85 V

Although the reduction potential of these reactions has become more positive, and thus more favourable, when related to Gibb's free energy ($\Delta G = -(nFE^o)$, these reactions are non-spontaneous.

The use of homogeneous molecular catalysts as a method to reduce the energy required to reach the activation barrier, and thus reduce the overpotential of the CO_2 reduction reactions has become widespread as scientists aim for carbon neutrality. These molecular catalysts serve to overcome the kinetic barrier by promoting proton-coupled electron transfer (PCET) and

activating CO_2. PCET occurs through the transfer of electrons from one atom to another, so instead of reducing at -2.14 V (vs SCE) in single electron reduction, or -0.77V (vs SCE) in MET for CO_2 to CO, a catalyst would be reduced at a much lower potential and would transfer electrons directly to CO_2 thereby reducing it for a fraction of the energy cost. Catalysts allow for CO_2 to bind to the metal center leading to intramolecular electron and proton transfer which is quicker and requires less energy.[17]

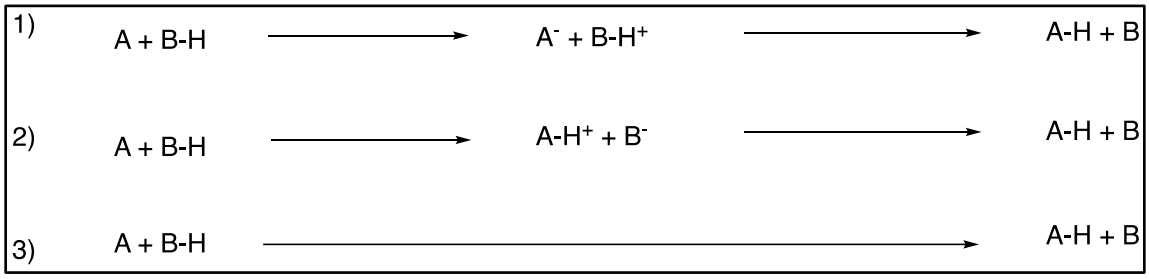

Figure 1: Depiction showing the different pathways between 1) electron transfer, 2) proton transfer, and 3) proton-coupled electron transfer (PCET). PCET occurs in essentially one step as opposed to discrete electron and proton transfer mechanisms which occur in two.

NO_3^- and NO_2^- as Water Contaminants and their Reduction

Because of the massive scale of the Haber-Bosch process, the global nitrogen cycle has seen a dramatic increase in human-made nitrogen content which has begun to overshadow the production of bioavailable nitrogen.[18] While the Haber-Bosch process is a necessity for the planet's growing population, due to the significance of the ammonia produced for use in ammonia-based fertilizers, there has been detrimental side-effects on the planet's ecosystems. One of these side effects is fertilizer run off which makes its way into waterways, lakes, rivers, and oceans which fertilize blooms of algae, resulting in oxygen depletion in these bodies of water, thus rendering them as aquatic dead zones. Along with eutrophication, nitrogen oxyanions like nitrite pose a significant health risk towards both aquatic and land organisms. Nitrites, although typically short-lived, can cause diseases such as brown blood disease which leads to the poisoning and accelerated death of fish if they experience prolonged exposure to high

concentrations. [19] However, nitrite poisoning is not exclusive to aquatic life. When nitrite concentrations are high enough in the human body to enter the blood stream, it can oxidize hemoglobin, leading to a condition called methemoglobinemia which prevents the hemoglobin from delivering oxygen to cells.[19,20] There are other potential harmful results of high nitrite levels in the body such as birth defects, thyroid disease, and colon cancer. [19] Because of these effects, governments and scientists have invested resources into methods to mitigate the amount of nitrogen oxyanions that may end up in lakes and our drinking water.

One of the potential remedies to this widespread problem is the electrochemical reduction of nitrite into valuable chemical building blocks like NH_2OH and NH_3, and inert materials such as N_2. Like CO_2, the reduction of NO_2^- can take several routes resulting in various products.[11]

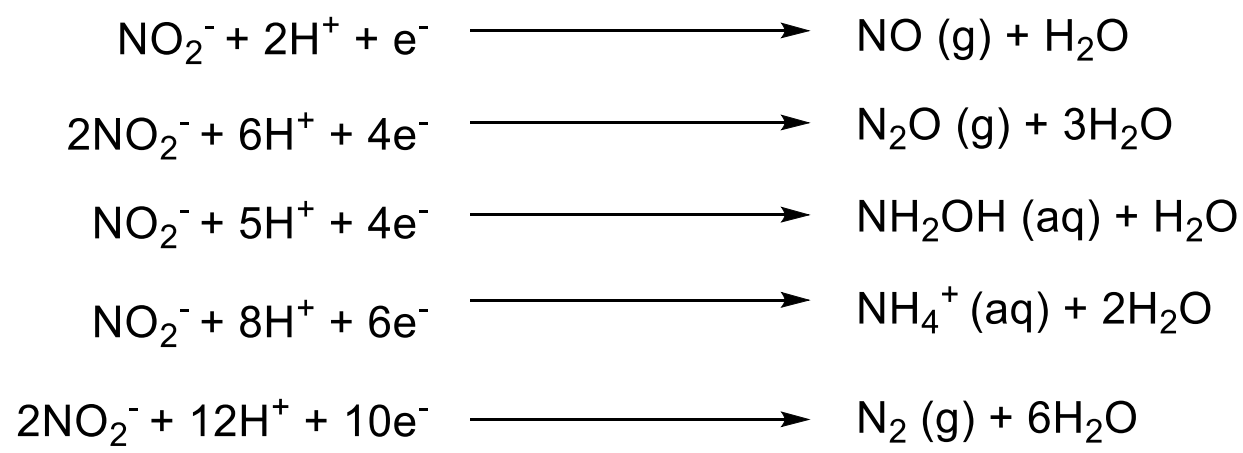

Figure 2: Generic depiction of the electrochemical reduction of NO_2^- to various products

To make the electrochemical reduction of NO_2^- more efficient, transition metal complexes are being employed as a method of not only reducing this harmful chemical, but also to elucidate the mechanisms of these transformations. Depending on the catalyst, several products are available, and are often in competition. Also, depending on the pH of the solution, the formation of certain products may be favoured over others.[21,22] For instance, the reduction of protons, a hydrogen evolution reaction (HER), is pH dependent and are often in competition with

nitrate and nitrite electroreduction reactions. It has been shown that in acidic media, HER can lower the Faradaic efficiency of the nitrate/nitrite reduction reaction. Additionally, Xing et al. demonstrated that in alkaline media (lower availability of H^+), the reduction of nitrate halts at NO_2^- whereas in acidic media (higher availability of H^+) nitrite reduction is favoured and leads to reduction products such as NH_4^+, N_2, N_2O, etc. Thus, the use of buffer systems in nitrate and nitrite reduction reactions is a necessity to control the pH of the system and aid in revealing mechanistic insights towards pH dependent product formation. Smith et al. also showed that some buffers have an impact on the reaction mechanism by participating as an intermolecular proton shuttle, thus opening doors towards more intricate catalytic nitrite reduction systems.[23]

Earth Abundant Metals as Catalysts

As chemistry leans towards a more environmentally responsible, green approach, researchers have placed increasing emphasis on developing catalysts that are efficient and sustainable. Sustainability has become an increasingly important characteristic of molecular catalysts based on factors such as abundance and price. The most abundant of these metals are Fe, Ni, and Co with natural abundances of 32%, 1.8% and 0.88% respectively.[24] Other transition metals such as Mn, Cu and Mo are often easy to obtain and are relatively sustainable compared to precious metals like Re, Ir, and Ru which have concentrations in the parts-per-billions. Due to the abundance of these metals, it is not surprising that they are commonly explored for reactivity in many catalytic transformations like nitrate and nitrite reduction reactions, CO_2 reduction reactions, water splitting and hydrogen evolution reactions, cross-coupling reactions, polymerisations, and many others.[8,25-29]

Scope and Content of this Thesis

This thesis consists of three projects each of which focus on a broadly targeted area of electrocatalysis using earth abundant metals as the catalyst center to promote sustainability. Specifically, chapter 2 focuses on the reduction of CO_2 gas to value-added products, chapter 3 on the production of H_2 from water, and chapter 4 on the reduction of nitrite to useful chemical building blocks. Each of these areas presents a significant challenge that society faces with respect to improving the overall quality of the environment and human health.

The first project was aimed at using electrophotocatalysis to reduce CO_2 by employing a transition metal complex bearing an integrated chromophore on one of its ligands. The approach behind this endeavour was to exploit the extreme reducing power of a photocatalyst in its radical anionic state, and by attaching it directly to a π–conjugated ligand, with the goal of increased lifetime and reaction rate.

The second project explored the use of water as a renewable and green proton source and solvent to generate H_2 using a Ni(II) diiminopyridine complex. Part of this project investigated the mechanism of how this metal complex performed hydrogen generation in both aqueous solution and organic solution using acetonitrile and trifluoroacetic acid (TFA) as the proton donor.

The third project was a new endeavour for our group which looked at reducing nitrite (NO_2^-) in neutral aqueous solution using a Ni or Co macrocyclic complex featuring a diiminopyridine core. Part of this project was to elucidate the nitrite reduction mechanism to help us understand part of the nitrogen cycle.

References

(1) Vitousek, P. M.; Mooney, H. A.; Lubchenco, J.; Melillo, J. M. Human Domination of Earth's Ecosystems. *Science* **1997**, *277* (5325), 494–499. https://doi.org/10.1126/science.277.5325.494.

(2) *Nitrate in Drinking Water - MN Dept. of Health*. https://www.health.state.mn.us/communities/environment/water/contaminants/nitrate.html (accessed 2023-05-30).

(3) Singh, S.; Anil, A. G.; Kumar, V.; Kapoor, D.; Subramanian, S.; Singh, J.; Ramamurthy, P. C. Nitrates in the Environment: A Critical Review of Their Distribution, Sensing Techniques, Ecological Effects and Remediation. *Chemosphere* **2022**, *287*, 131996. https://doi.org/10.1016/j.chemosphere.2021.131996.

(4) Trewavas, A. Fertilizer: No-till Farming Could Reduce Run-Off. *Nature* **2004**, *427* (6970), 99–99. https://doi.org/10.1038/427099c.

(5) Sun, Z.; Ma, T.; Tao, H.; Fan, Q.; Han, B. Fundamentals and Challenges of Electrochemical CO_2 Reduction Using Two-Dimensional Materials. *Chem* **2017**, *3* (4), 560–587. https://doi.org/10.1016/j.chempr.2017.09.009.

(6) Wu, J.; Huang, Y.; Ye, W.; Li, Y. CO_2 Reduction: From the Electrochemical to Photochemical Approach. *Adv. Sci.* **2017**, *4* (11), 1700194. https://doi.org/10.1002/advs.201700194.

(7) Genovese, C.; Ampelli, C.; Perathoner, S.; Centi, G. Mechanism of C–C Bond Formation in the Electrocatalytic Reduction of CO_2 to Acetic Acid. A Challenging Reaction to Use Renewable Energy with Chemistry. *Green Chem.* **2017**, *19* (10), 2406–2415. https://doi.org/10.1039/C6GC03422E.

(8) Stroka, J. R.; Kandemir, B.; Matson, E. M.; Bren, K. L. Electrocatalytic Multielectron Nitrite Reduction in Water by an Iron Complex. *ACS Catal.* **2020**, *10* (23), 13968–13972. https://doi.org/10.1021/acscatal.0c03600.

(9) Meng, S.-L.; Zhang, C.; Ye, C.; Li, J.-H.; Zhou, S.; Zhu, L.; Li, X.-B.; Tung, C.-H.; Wu, L.-Z. Cobaloximes: Selective Nitrite Reduction Catalysts for Tandem Ammonia Synthesis. *Energy Environ. Sci.* **2023**, *16* (4), 1590–1596. https://doi.org/10.1039/D2EE03956G.

(10) Kroneck, P. M. H. Nature's Nitrite-to-Ammonia Expressway, with No Stop at Dinitrogen. *J Biol Inorg Chem* **2022**, *27* (1), 1–21. https://doi.org/10.1007/s00775-021-01921-4.

(11) Zhang, X.; Wang, Y.; Wang, Y.; Guo, Y.; Xie, X.; Yu, Y.; Zhang, B. Recent Advances in Electrocatalytic Nitrite Reduction. *Chem. Commun.* **2022**, *58* (17), 2777–2787. https://doi.org/10.1039/D1CC06690K.

(12) Jangam, A.; Das, S.; Dewangan, N.; Hongmanorom, P.; Hui, W. M.; Kawi, S. Conversion of CO2 to C1 Chemicals: Catalyst Design, Kinetics and Mechanism Aspects of the Reactions. *Catalysis Today* **2020**, *358*, 3–29. https://doi.org/10.1016/j.cattod.2019.08.049.

(13) Muthuramalingam, S.; Velusamy, M.; Mayilmurugan, R. Fixation of Atmospheric CO_2 as C1-Feedstock by Nickel(II) Complexes. *Dalton Trans.* **2021**, *50* (23), 7984–7994. https://doi.org/10.1039/D0DT03887C.

(14) Kortlever, R.; Shen, J.; Schouten, K. J. P.; Calle-Vallejo, F.; Koper, M. T. M. Catalysts and Reaction Pathways for the Electrochemical Reduction of Carbon Dioxide. *J. Phys. Chem. Lett.* **2015**, *6* (20), 4073–4082. https://doi.org/10.1021/acs.jpclett.5b01559.

(15) Sordakis, K.; Tang, C.; Vogt, L. K.; Junge, H.; Dyson, P. J.; Beller, M.; Laurenczy, G. Homogeneous Catalysis for Sustainable Hydrogen Storage in Formic Acid and Alcohols. *Chem Rev* **2018**, *118* (2), 372–433. https://doi.org/10.1021/acs.chemrev.7b00182.

(16) Zhong, H.; Iguchi, M.; Chatterjee, M.; Himeda, Y.; Xu, Q.; Kawanami, H. Formic Acid-Based Liquid Organic Hydrogen Carrier System with Heterogeneous Catalysts. *Adv. Sustainable Syst.* **2018**, *2* (2), 1700161. https://doi.org/10.1002/adsu.201700161.

(17) Barton Cole, E.; Lakkaraju, P. S.; Rampulla, D. M.; Morris, A. J.; Abelev, E.; Bocarsly, A. B. Using a One-Electron Shuttle for the Multielectron Reduction of CO_2 to Methanol: Kinetic, Mechanistic, and Structural Insights. *J. Am. Chem. Soc.* **2010**, *132* (33), 11539–11551. https://doi.org/10.1021/ja1023496.

(18) Smith, C.; Hill, A. K.; Torrente-Murciano, L. Current and Future Role of Haber–Bosch Ammonia in a Carbon-Free Energy Landscape. *Energy Environ. Sci.* **2020**, *13* (2), 331–344. https://doi.org/10.1039/C9EE02873K.

(19) Yang, X.; Wu, X.; Hao, H.; He, Z. Mechanisms and Assessment of Water Eutrophication. *J Zhejiang Univ Sci B* **2008**, *9* (3), 197–209. https://doi.org/10.1631/jzus.B0710626.

(20) Glibert, P. M.; Maranger, R.; Sobota, D. J.; Bouwman, L. The Haber Bosch–Harmful Algal Bloom (HB–HAB) Link. *Environ. Res. Lett.* **2014**, *9* (10), 105001. https://doi.org/10.1088/1748-9326/9/10/105001.

(21) Hu, H.-Y.; Goto, N.; Fujie, K. Effect of Ph on the Reduction of Nitrite in Water by Metallic Iron. *Water Research* **2001**, *35* (11), 2789–2793. https://doi.org/10.1016/S0043-1354(00)00570-4.

(22) Clark, C. A.; Reddy, C. P.; Xu, H.; Heck, K. N.; Luo, G.; Senftle, T. P.; Wong, M. S. Mechanistic Insights into pH-Controlled Nitrite Reduction to Ammonia and Hydrazine over Rhodium. *ACS Catal.* **2020**, *10* (1), 494–509. https://doi.org/10.1021/acscatal.9b03239.

(23) Braley, S. E.; Kwon, H.-Y.; Xu, S.; Dalton, E. Z.; Jakubikova, E.; Smith, J. M. Buffer Assists Electrocatalytic Nitrite Reduction by a Cobalt Macrocycle Complex. *Inorg. Chem.* **2022**, *61* (33), 12998–13006. https://doi.org/10.1021/acs.inorgchem.2c00909.

(24) Morgan, J. W.; Anders, E. Chemical Composition of Earth, Venus, and Mercury. *Proc. Natl. Acad. Sci. U.S.A.* **1980**, *77* (12), 6973–6977. https://doi.org/10.1073/pnas.77.12.6973.

(25) Li, Y.-Y.; Yu, S.-L.; Shen, W.-Y.; Gao, J.-X. Iron-, Cobalt-, and Nickel-Catalyzed Asymmetric Transfer Hydrogenation and Asymmetric Hydrogenation of Ketones. *Acc. Chem. Res.* **2015**, *48* (9), 2587–2598. https://doi.org/10.1021/acs.accounts.5b00043.

(26) Tollefson, E. J.; Hanna, L. E.; Jarvo, E. R. Stereospecific Nickel-Catalyzed Cross-Coupling Reactions of Benzylic Ethers and Esters. *Acc. Chem. Res.* **2015**, *48* (8), 2344–2353. https://doi.org/10.1021/acs.accounts.5b00223.

(27) Xu, S.; Kwon, H.-Y.; Ashley, D. C.; Chen, C.-H.; Jakubikova, E.; Smith, J. M. Intramolecular Hydrogen Bonding Facilitates Electrocatalytic Reduction of Nitrite in Aqueous Solutions. *Inorg. Chem.* **2019**, *58* (14), 9443–9451. https://doi.org/10.1021/acs.inorgchem.9b01274.

(28) Norouziyanlakvan, S.; Ferguson, J.; Richeson, D. Electrocatalytic Hydrogen Production from Neutral Water Using an Aqueous Ni(II) Pincer Complex. *Catal. Sci. Technol.* **2022**, *12* (24), 7494–7500. https://doi.org/10.1039/D2CY01504H.

(29) Yu, J.; Le, T. A.; Tran, N. Q.; Lee, H. Earth-Abundant Transition-Metal-Based Bifunctional Electrocatalysts for Overall Water Splitting in Alkaline Media. *Chem. Eur. J.* **2020**, *26* (29), 6423–6436. https://doi.org/10.1002/chem.202000209.

Chapter 2: Attempts at Developing an "Electrophotocatalytic" System

Introduction:

The use of photocatalysis for the catalytic conversion of CO_2 has been utilized for decades and is a well-established field in chemistry. Part of the attraction of photocatalysis is due to the use of light as a low-cost and sustainable method to activate reaction pathways. Apart from these benefits, photochemistry in general is relatively easy to access and setup.[1-3] A typical photocatalytic system is constructed in the following way: A light source which provides an unlimited amount of light at a specific wavelength which is used to initiate the reaction cycle by photoexciting a photosensitizer (PS*) which is reductively quenched by a sacrificial electron donor (SED) that provides electrons to the photosensitizer (PS^-). The reduced PS^- transports electrons to a catalyst reducing it, and converting this species into an active catalyst ready to react with a substrate. One of the limiting factors of using this approach is having to use a sacrificial electron donor (SED) since they are non-recyclable and are converted to waste once they transfer the electron.[4,5] Another key issue with a photocatalytic setup is having to depend on the collision and subsequent interaction between photosensitizer and catalyst which can limit their reactivity and overall product yield.

Electrocatalysis on the other hand utilizes electricity to supply electrons to a catalyst to initiate the catalytic cycle. One of the main objectives of electrocatalysis is to reduce the electrical potential necessary for reactions to occur which can provide a greener and sustainable alternative of supplying electrons when compared to using a sacrificial electron donor in a photocatalytic system. However, to supply electrons using electricity requires a large amount of energy which is not a very economical approach. Thus, the employment of electrocatalysts to

reduce the potential required to initiate and speed up a reaction has become commonplace in electrolysis.[6,7]

The design of a catalytic system has many concerns, and an economical approach plays a large part in the consideration of materials used in designing such a system. Many electrocatalytic and photocatalytic systems use transition metal complexes for the transfer of electrons; however many of these systems employ precious metals such as rhenium, iridium and ruthenium which are not very cost efficient or sustainable when considering abundancy and potential to scale up a reaction system.[8-10]

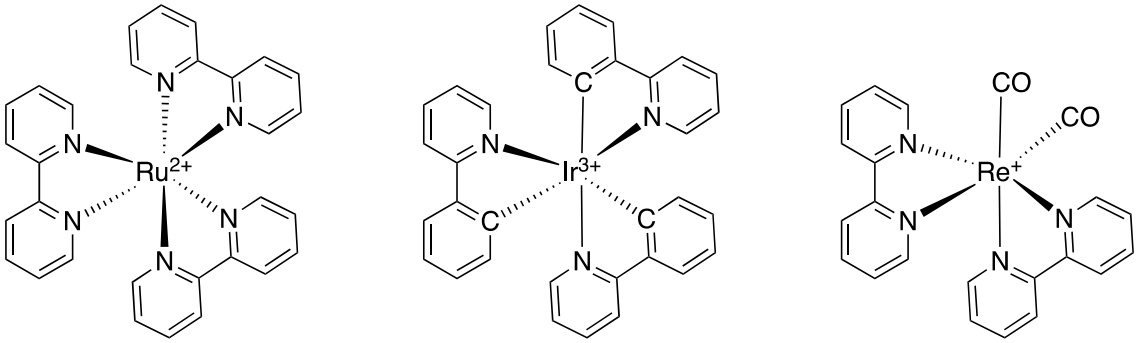

Figure 1: Examples of well-known transition metal catalysts containing a precious metal.

In order to address these issues, chemists often look seek catalysts that have metals that are more Earth abundant and accessible. Metals such as Mn which have a concentration of 750 ppm are considered relatively Earth abundant. For comparison, ruthenium, iridium, and rhenium make up only 1.18 ppm, 840 ppb, and 60 ppb of the Earth's mass.[11] Thus, with sustainability and accessibility in mind, we chose to prepare an Mn complex as a potential catalyst.

Electrophotochemistry

Lambert et al. recently published a successful attempt at employing the principles of tandem cathodic reduction and photoexcitation of a known photosensitizer to act as a strong reducing agent. In their work they utilized dicyanoanthracene (DCA) which has a reduction potential of $E_{1/2}$ = -0.82 V (vs SCE), but as a radical anion has a reducing power of -3.20 V (vs

SCE). The extremely high reducing power of this radical anion is speculated to be due to a SOMO-HOMO inversion that takes place, resulting in a half-filled bonding orbital and filled anti-bonding orbital (Figure 2) leaving the electronic structure of the radical anion of DCA to be highly unstable.[12]

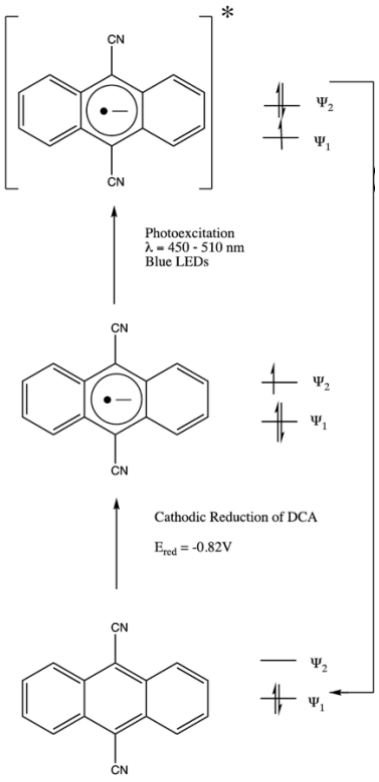

Figure 2: Generic depiction of the electrochemical reduction and tandem photoexcitation of dicyanoanthracene (DCA).

We attempted to take advantage of this approach and to use the radical anion DCA to reduce a catalyst, which would then reduce CO_2 into useful products. Unfortunately, we did not have success in this effort.

This type of electrophotocatalysis was also explored by Wickens et al. with the use of several photoreductants that demonstrated extreme reducing potentials when experiencing

tandem electrolysis and photolysis. The Wickens group put to the test four photocatalysts for the radical coupling of aryl chlorides that are shown in Figure 3.[13]

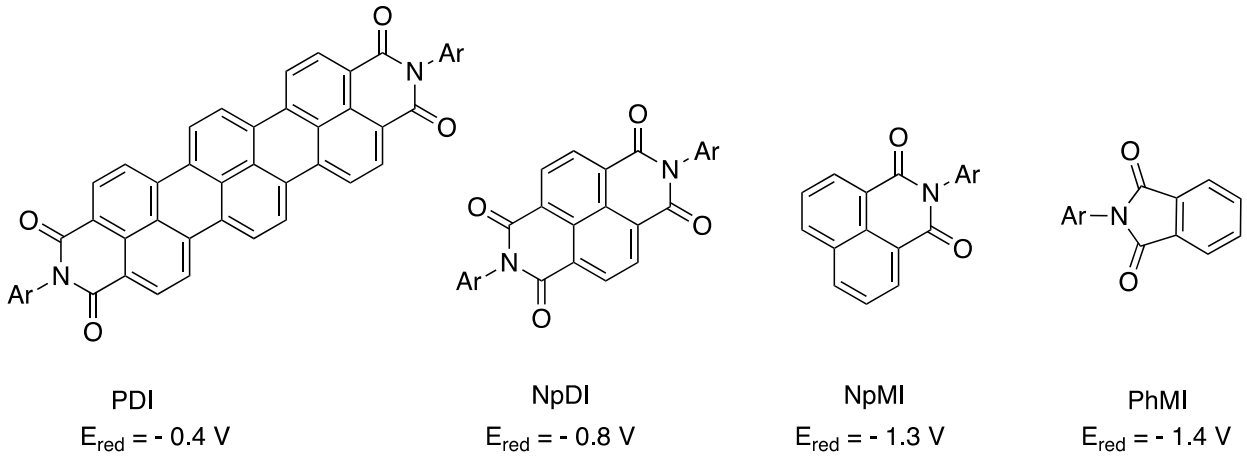

Figure 3: Photocatalysts used for the radical coupling of aryl chlorides.

During experimentation, they found that **NpMI** was the highest performing photocatalyst which could provide a reduction potential as high as -3.40 V (vs SCE) when reduced and photoexcited. NpMI is also easily reducible with an E_{red} of -1.30 V (vs SCE) thus offering the possibility of providing a low potential input with a stronger reduction potential upon excitation. This concept was demonstrated by the high yields during aryl chloride phosphorylation and heteroarylation. With the success of **NpMI** as an effective reducing agent capable of reaching extremely negative potentials, we aimed at incorporating this valuable characteristic into a ligand.

Our strategy for mitigating the effects of low lifetime and collisions between molecules was to attach the photosensitizer to an electrocatalyst that was documented to be successful for CO_2 reduction. This concept was previously reported by Castello et al. when they demonstrated the effectiveness of having an organic chromophore and metal complex bichromophore system.

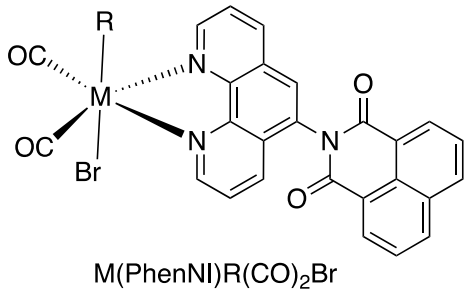

Figure 4: Metal complex bearing the PhenNI (or NIphen) ligand. NI is the naphalimide portion of the ligand.

After investigation, they found that the bichromophore system increased the triplet lifetime up to 3000-fold when compared to using just the organic chromophore due to thermal equilibrium between ^{3}MLCT-^{3}LC.[14] With the intention of taking advantage of the extreme reducing power of **NpMI** that the Wickens group demonstrated and the increased lifetime that the **NIphen** ligand provided by having a photocatalyst as part of a metal complex, we thought it would be worthwhile to determine whether we could use these properties for the reduction of CO_2 and generation of H_2.

Overview

In this chapter, we will explore our attempts at combining the methods and characteristics of both photocatalysis and electrocatalysis to design a system that can simultaneously reduce and photoexcite a photosensitizer with a reduction potential lower than that of a known CO_2 reducing electrocatalyst.

Results & Discussion:

Synthesis and Structural Characterization

For this project we aimed to synthesize a non-traditional photocatalyst using an earth abundant metal that has previously been demonstrated to electrochemically reduce CO_2. Our first target was the synthesis of the PhenNI ligand.

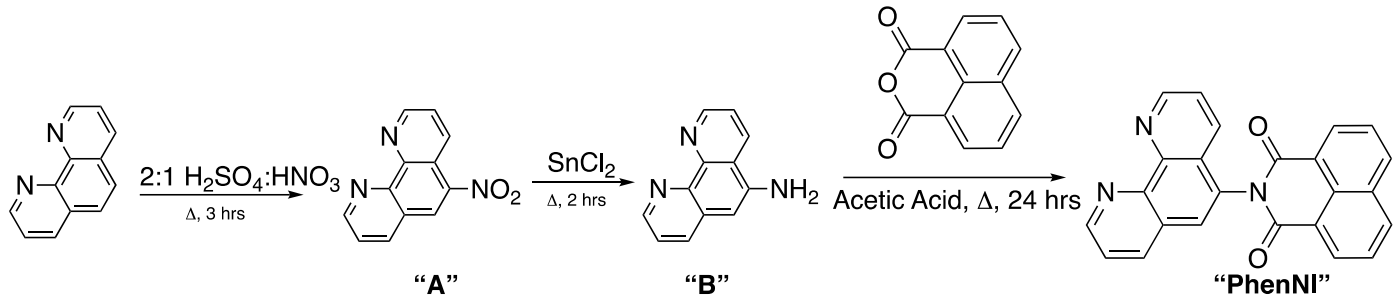

Scheme 1: Reaction scheme for the synthesis of PhenNI

Synthesis of 5-nitro-1,10-phenanthroline (**A**):

To a solution of 1,10-phenanthroline dissolved in 30 mL sulfuric acid, 15 mL of fuming nitric acid was added slowly at 160 ºC. The solution was kept stirring at 160 ºC for 3 hours then carefully poured into ice water. Saturated NaOH solution was added until the pH was adjusted to 3, and the target molecule precipitated. The product was filtered and washed with cold water then dried in vacuo. The proton NMR spectrum (Figure 5) is in accordance with the literature.[15]

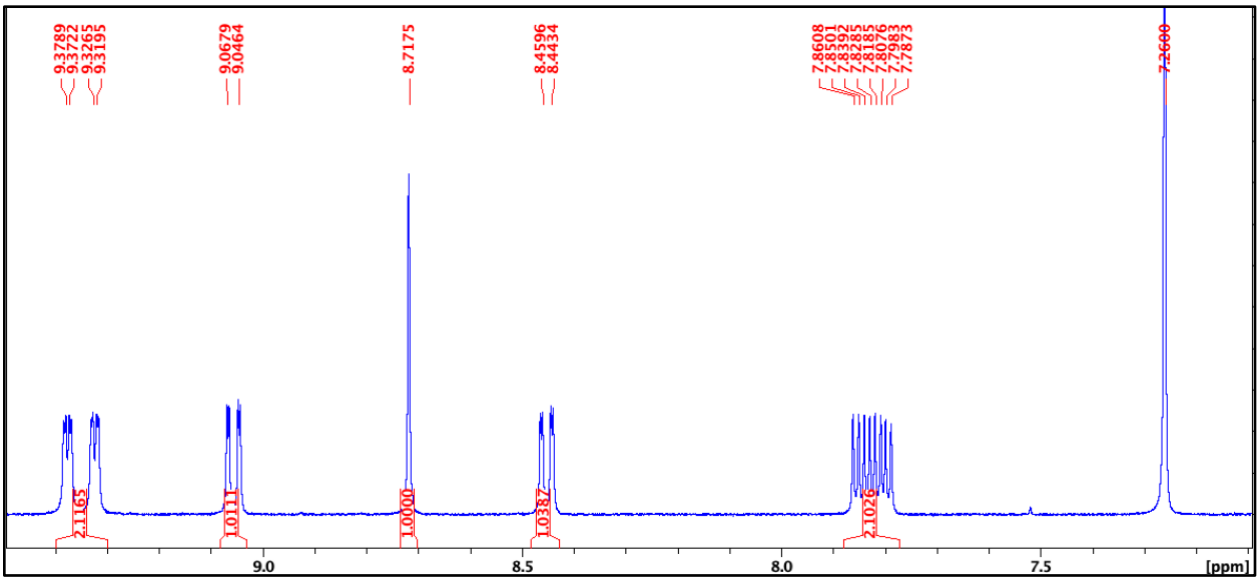

Figure 5: 1H NMR spectrum of 5-nitro-1,10-phenanthroline in $CDCl_3$.

Synthesis of 5-amino-1,10-phenanthroline (**B**):

While stirring, 3.6 g (0.016 mole) of **A** was added to 15.2 g (0.08 mole) of $SnCl_2$ dissolved in 46 ml of conc. hydrochloric acid . The solution was stirred for 1 h at 80 - 90 ºC then cooled and

treated with a 40% solution of NaOH followed by addition of 250 g of crushed ice. The residue was filtered off, washed with water to a neutral pH, and recrystallized from ethanol. The proton NMR spectrum (Figure 6) is in accordance with the literature.[16]

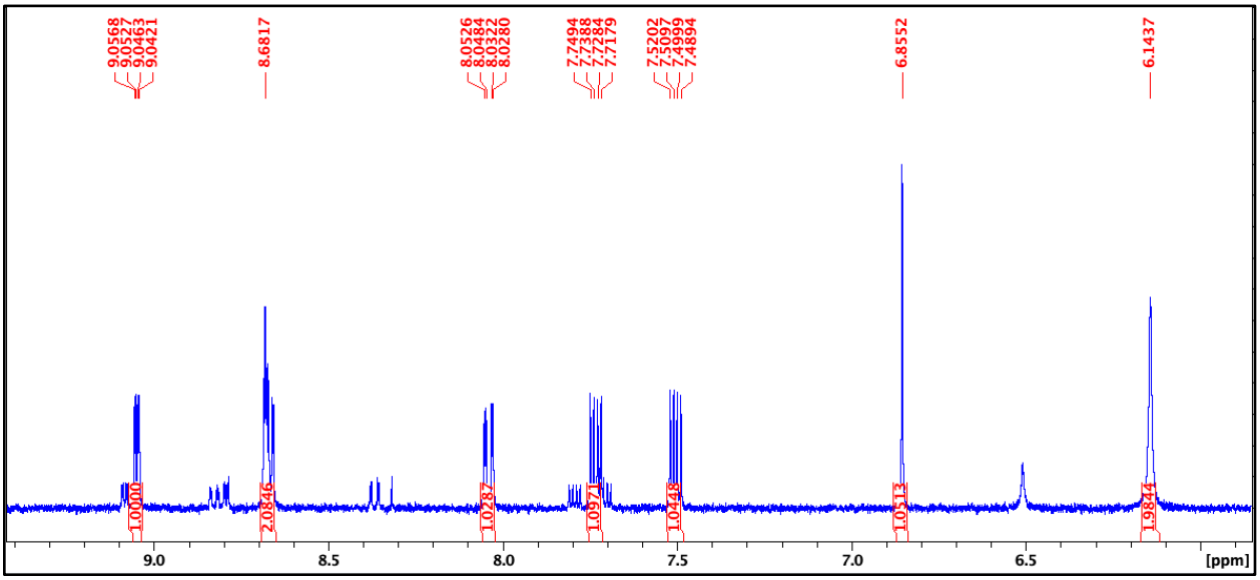

Figure 6: 1H NMR spectrum of 5-amino-1,10-phenanthroline in $CDCl_3$.

Synthesis of **PhenNI** ligand:

4.4 mmol of 5-Amino-1,10-phenanthroline (**B**), 4 mmol 1,8-naphthalic anhydride, and 25 mL of glacial acetic acid were added to a 50 mL pressure vessel and heated to 150 °C for 24 hours. After cooling to RT, 15 mL of distilled water was added to the solution and the light brown precipitate was filtered on a glass frit. The solid was washed with 200 mL of water and dried overnight in vacuo to give an off-white solid. The proton NMR spectrum is in accordance with the literature.[17]

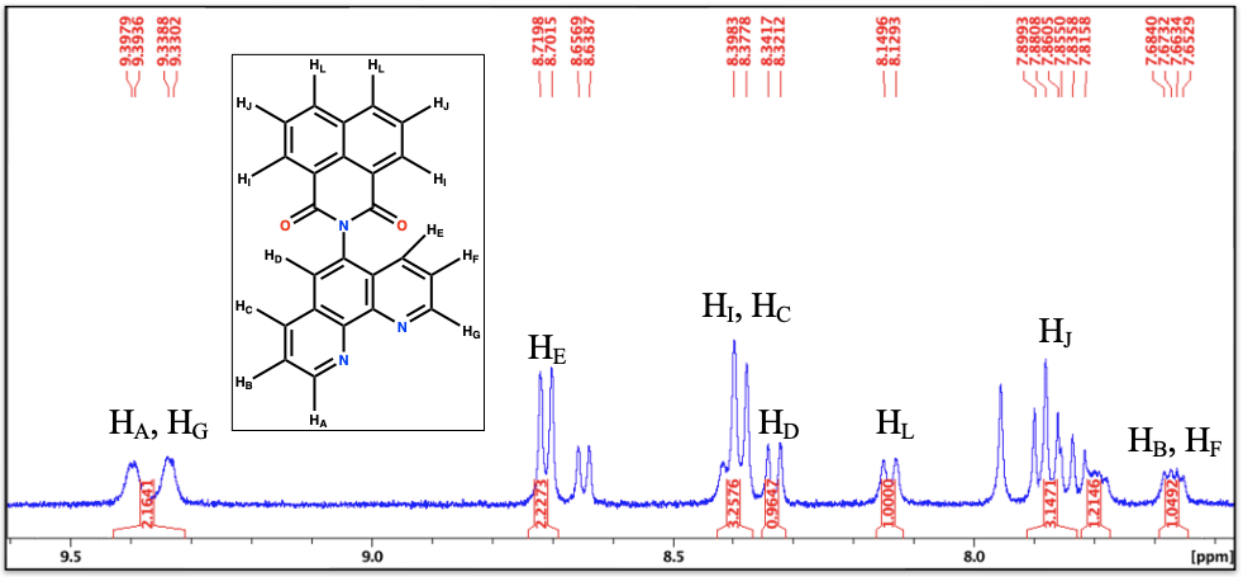

Figure 7: NMR spectrum of PhenNI in $CDCl_3$ with identified peaks.

With confirmation that we made the PhenNI ligand (Figure 7), our next target was the synthesis of a documented CO_2 reducing electrocatalyst. It is well known that $Mn(bipy)CO_3X$ (X = Br, Cl) are capable of electrochemically reducing CO_2 at very negative potentials (E_{red} = -1.5V to -2.5V vs Ag/Ag^+) depending on the bound alpha-diimine ligand.[18] Our concept behind this is to replace the bipy ligand with PhenNI (Scheme 2) and electrochemically reduce the naphathalimide (NI) component followed by subsequent photoexcitation which could provide a large enough negative reduction potential for the Mn(I) center to carry out CO_2 reduction.

Synthesis of MnPhenNI (**1**):

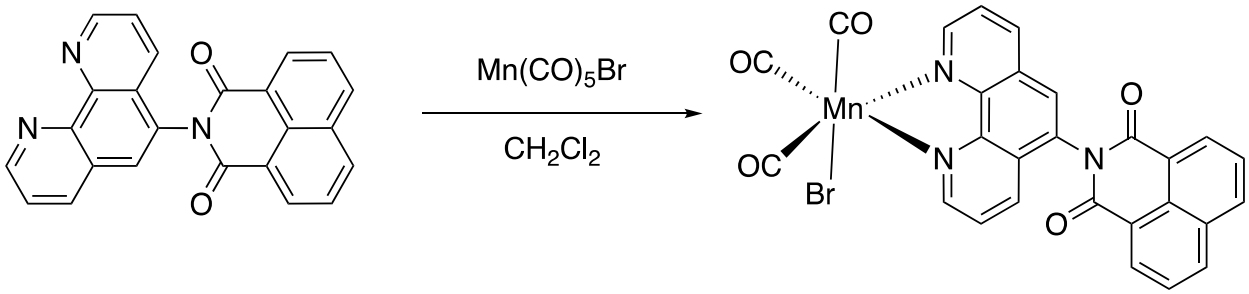

Scheme 2: Reaction scheme for the synthesis of MnPhenNI

The manganese-PhenNI complex was synthesized by stirring solution with a 1.1:1 molar ratio of the 1,8-naphthalic anhydride-N-1,10-phenanthroline (PhenNI) ligand to $Mn(CO)_5Br$ dissolved in dichloromethane in the absence of light and air. Obtaining crystals suitable for x-ray diffraction is currently an ongoing investigation.

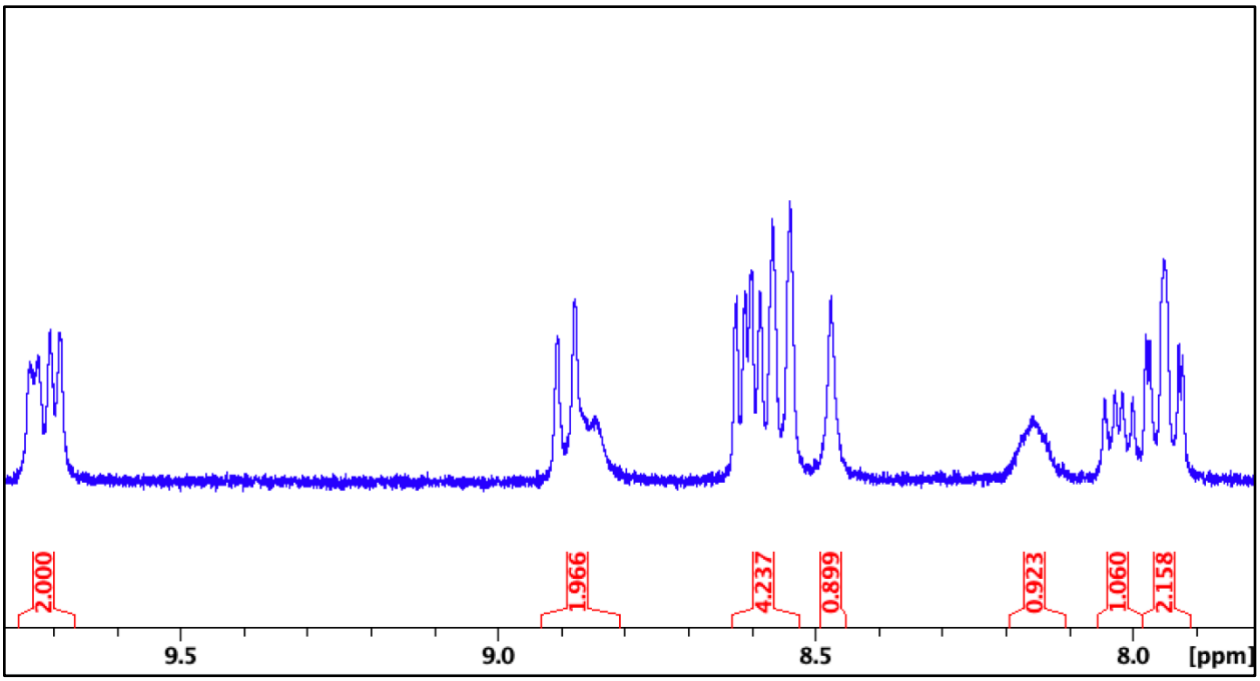

Figure 8: 1H NMR Spectrum of MnPhenNI in Acetone-d6. The sample was prepared in a glovebox free of air and moisture and wrapped with aluminum foil to keep it from reacting with light.

UV-Vis Electronic Spectrum

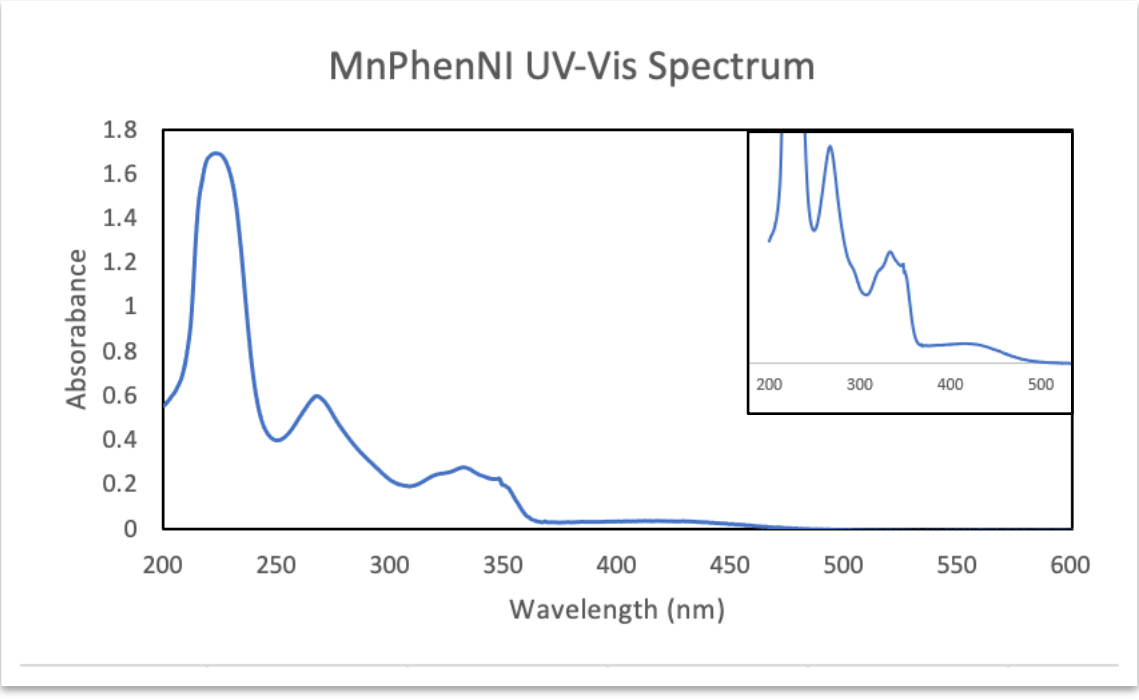

Figure 9: UV-Vis spectrum of Mn-PhenNI in CH_3CN

After the use of ^1H NMR spectroscopy to provide evidence that the complex was synthesized (Figure 8), a UV-Vis measurement on MnPhenNI (Figure 9) was carried out in order to determine the wavelength of light that would be used to photoexcited the "naphthalene imide" chromophore during catalytic experimentation, and to provide us further evidence that the complex was made. The NI chromophore has a ligand-centered $\pi - \pi^*$ transition at 332nm which lines up to the literature. The maximum absorbance peaks at 225nm and 265nm match the literature for the Mn(II)(1,10-phenanthroline) complex.[19] The broad featureless peak at 413nm is the $d\pi(Mn) - \pi^*(phen)$ MLCT transition.[19] With the evidence provided by both NMR and UV-Vis, we were confident we made the correct complex.

Since we are aiming to simultaneously reduce and photoexcite the PhenNI, we would be looking to use light at a wavelength of about 330nm which would be in the range of UV light.

Electrochemical Characterization and "Electrophotocatalysis"

Cyclic voltammetry experiments were conducted in the absence of light on MnPhenNI which revealed 5 reduction peaks at -1.44, -1.65, -1.98, -2.41, and -2.74 V and two oxidation peaks at -1.57 and -2.63 V. Although there are several redox events present, we were only concerned with two of them in which the phenNI ligand is reduced and the complex shows catalytic current enhancement with the addition of a proton donor under both N_2 and CO_2. According to Tschierlei , et al., the reversible reduction peak at $E_{1/2}$ = -1.60 V (vs. Fc^0/Fc^+) corresponds to the attached phenNI ligand, and lines up perfectly with reversible peak at -1.60 V in CV found in Figure 10.[20]

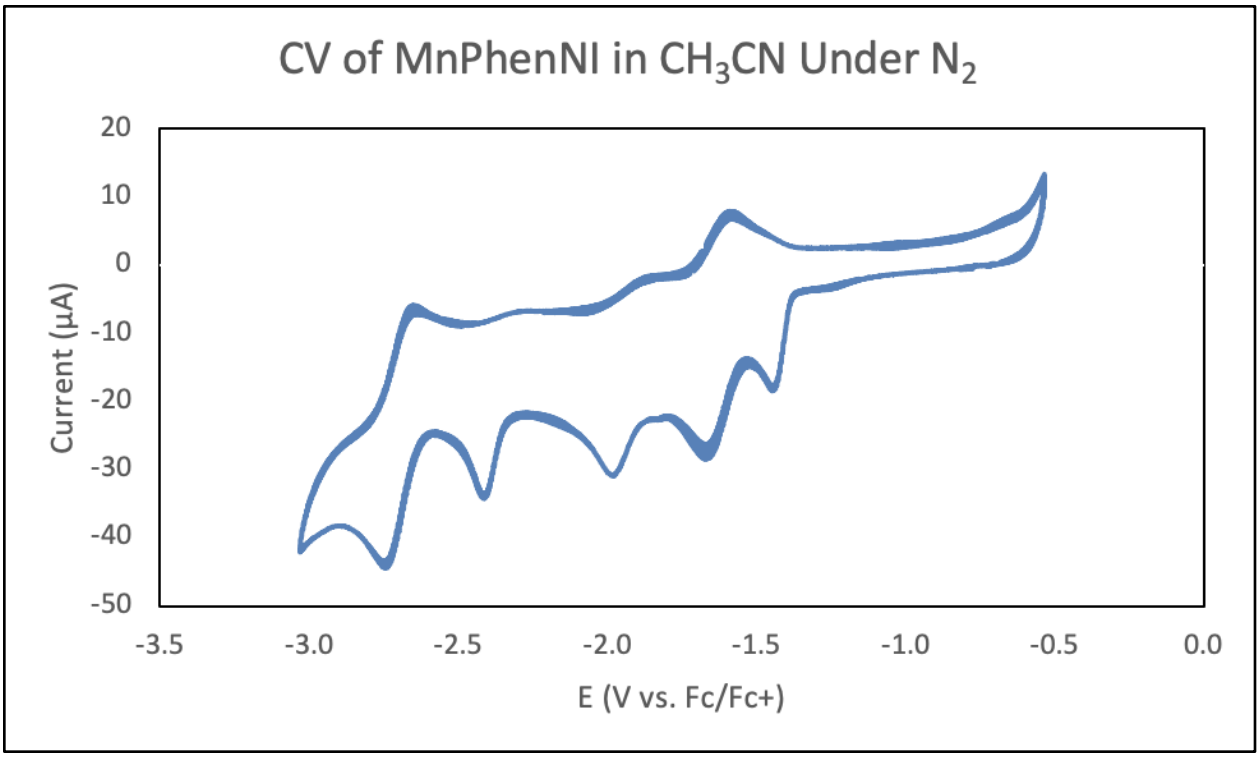

Figure 10: CV of MnPhenNI in CH_3CN (vs. Fc^0/Fc^+) under inert dinitrogen atmosphere with 0.1 M $TBAPF_6$ as the supporting electrolyte.

To further understand the reactivity of MnPhenNI, CV experiments with increasing aliquots of water were done to determine whether it can generate hydrogen using water as a proton source. Under a dinitrogen atmosphere, there was an apparent current enhancement at E = -2.74 V (vs. Fc^0/Fc^+). After 0.5 mL of water was added to the system, the enhancement began to decline and revert to enhancement like that of when the system had 0.3 mL of water introduced to it (Figure 11 below). Having the reduction peak of PhenNI at a significantly less negative potential (-1.60 V (vs Fc^0/Fc^+) compared to the enhancement in current from the addition of water at -2.74 V (vs. Fc^0/Fc^+) indicated to us that there is a possibility in utilizing this attached photosensitizer to our advantage.

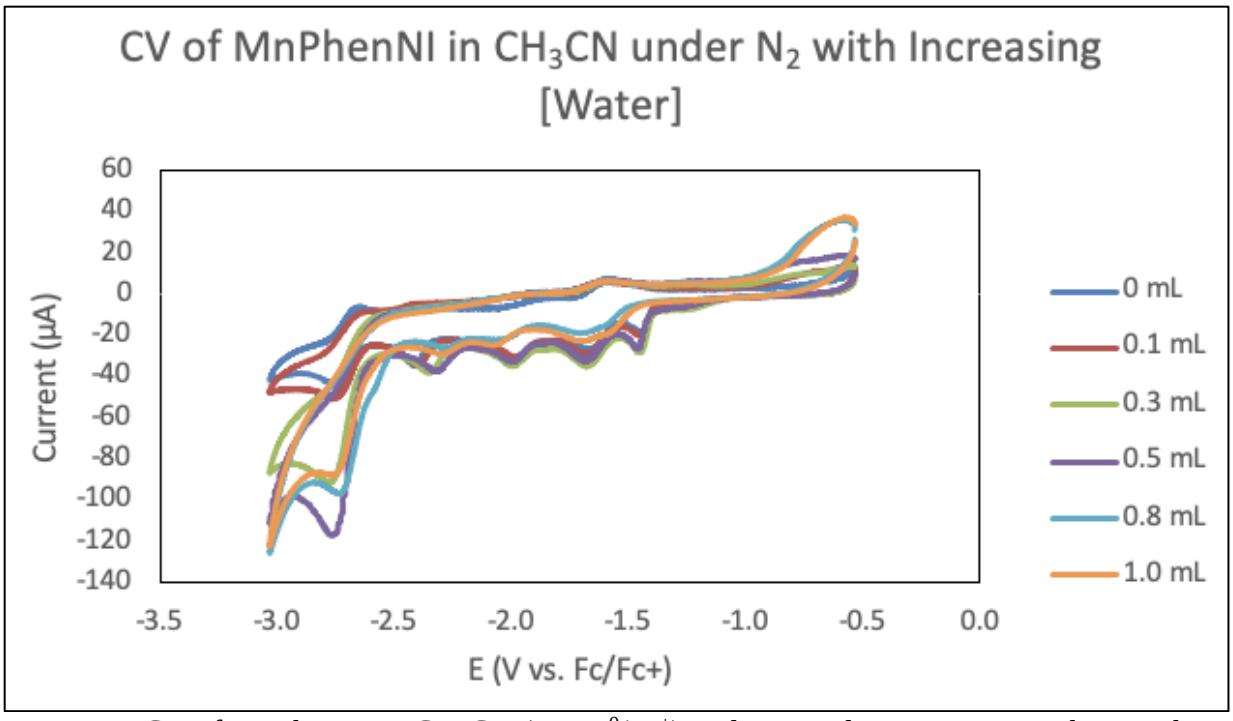

Figure 11: CV of MnPhenNI in CH_3CN (vs. Fc^0/Fc^+) under inert dinitrogen atmosphere with increasing aliquots of water with 0.1 M $TBAPF_6$ as the supporting electrolyte.

We also conducted CV experiments with MnPhenNI to determine if there is any catalytic activity when CO_2 is introduced to the system as a substrate. A change in electrochemical activity occurred after the introduction of CO_2 which resulted in a cathodic shift (shifted more negative) of the reduction peaks which is an expected signature for complexes with CO_2 reduction capabilities. The enhancement in the last reduction peak occurs in an area similar to that of other Mn(alpha-diimine) species that reduce CO_2. With this change in activity, we decided to continue investigating the reactivity of this complex when a proton source was introduced. Interestingly, after addition of water as a proton source, the complex lost almost all its electrochemical characteristics (Figure 13 below). This led to confusing results as it did not seem to be consistent with the electrochemical reduction of CO_2 by Mn(I)(1,10-phenanthroline)CO_3Br and other Mn(alpha-diimine) species demonstrated by Bocarsly et al.[19]

Regardless of this outcome, we decided to move forward with CPE experiments to further confirm the catalytic activity of this complex.

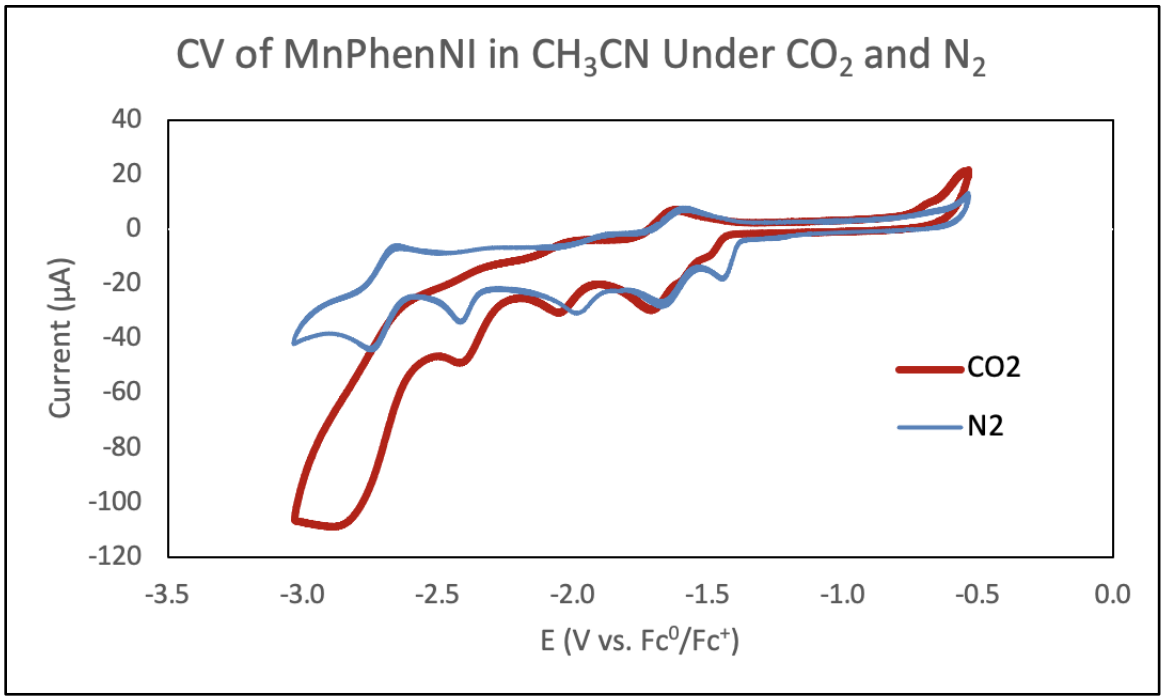

Figure 12: CV of MnPhenNI in CH_3CN (vs. Fc^0/Fc^+) under N_2 and CO_2 atmosphere water with 0.1 M $TBAPF_6$ as the supporting electrolyte.

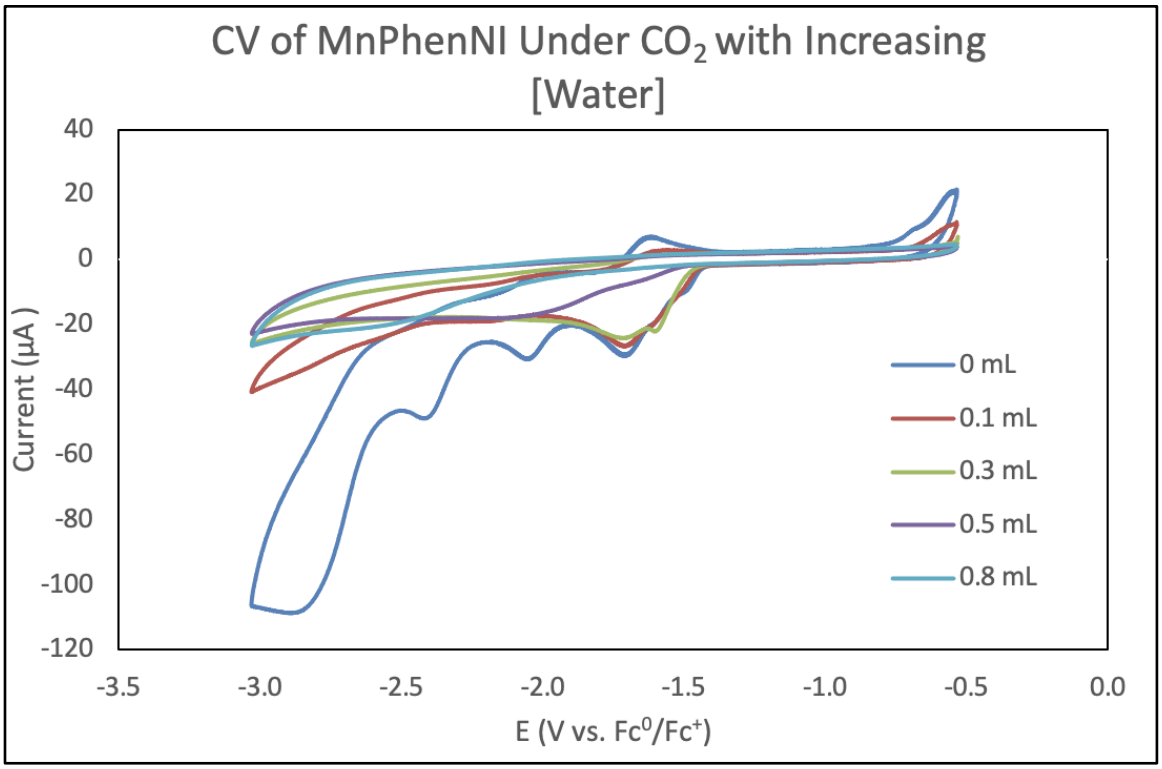

Figure 13: CV of MnPhenNI in CH_3CN (vs. Fc^0/Fc^+) under CO_2 atmosphere with increasing aliquots of water with 0.1 M $TBAPF_6$ as the supporting electrolyte.

The results for this endeavour are summarized in Table 1. All reactions were setup in an air- and moisture-free glovebox with 15 mL of dry CH3CN, 1 mM complex, and 1.0M $TBAPF_6$ as the supporting electrolyte. All reactions were run for 18 hours under the specified light and electrode potential.

Table 1: Table of Results for the "Electrophotocatalytic" attempts.

	Proton Donor	**Substrate**	**Electron Donor**	**E (V vs. Fc^+/Fc^0)**	**Light**	**µmol H2**	**µmol CO**
1	H_2O	CO_2	-	-1.6	Blue	4.0	-
2	H_2O	CO_2	-	-1.6	Blue	14	-
3	H_2O	N_2	-	-1.6	Blue	2.4	-
4	H_2O	N_2	-	-1.6	UV	-	-
5	H_2O	CO_2	-	-1.6	UV	-	-
6	H_2O	CO_2	TEA	-	Blue	-	-
7	H_2O	N_2	TEA	-	Blue	-	-
8	H_2O	CO_2	TEA	-	UV	-	-
9	H_2O	N_2	TEA	-	UV	-	-

In general, the experiments were carried out at -1.60 V (vs. Fc^0/Fc^+) under either a N_2 or CO_2 atmosphere with a 20:1 ratio of $CH_3CN:H_2O$ solution. These measurements documented the formation of H_2 as the only observed gas phase product. Measurements 1 through 3 showed H_2 as the main product albeit in an underwhelming yield with a maximum value of 14.3 µmol when blue light was employed in tandem with potential applied at E = -1.60 V (vs. Fc^0/Fc^+). Interestingly, experiment 2 yielded the most H_2 even though the CV (Figure 13 above) showed degradation of the complex when water was introduced to the CO_2 saturated system. Because of this result, we speculate that some of MnPhenNI complex did happen to be reduced by a photoexcited NI-anion leading to the reduction of water. However, since the reaction resulted in such a low yield this was unlikely the case. After such a low yield of H_2, we thought maybe the NI portion of the ligand was not being reduced properly. It was at this point we decided to determine whether our system was flawed by utilizing a sacrificial electron donor like in a typical photochemical experiment (Entries 6 – 9). Unfortunately, this led to no positive results either.

When comparing the results between entries 4 and 5 to 8 and 9, the experiments that employed UV light which is in the range at which the NI chromophore absorbs light, there was also no positive result showcasing catalytic activity. Additionally, throughout experimentation, the colour of the solution gradually shifted from bright yellow to deep orange, and then to colorless with white precipitate. We speculated that the NI chromophore was not being exposed to enough light to be photoexcited and thus was not able to reach its radical intermediate state meaning providing an electron for it to be reduced it would lead to no activity. However, after investigation, it was found that Mn(I) complexes with bound CO and diimine ligands react negatively to photolysis in the UV light range which results in dissociation of both the diimine

and CO ligands from the metal.[21] Due to this discovery we decided to halt further experimentation and discontinue the project.

Conclusions and Future Work

These results demonstrated the lack of ability for the MnPhenNI complex to act as a catalyst for CO_2 reduction and H_2 generation using the electrophotocatalytic method due to its degradation from UV light and when irradiated with blue light, showed no signs of catalysis. In the future, the use of a more robust and well-established complex, such as one using a rhenium(I) complex highlighted by Castellano et al. would potentially be an avenue worth pursuing. Additionally, the use of a photocatalyst not bound to the 1,10-phenanthroline ligand that has already been shown to exhibit extreme reducing power, such as NpMI, would be an interesting venture as to whether these compounds can reduce transition metal complexes and enable them to activate and reduce CO_2.

Experimental:

Electrochemistry and Electrophotochemistry

All cyclic voltammetry experiments were carried out in a single compartment cell of approximately 50 mL volume under an atmosphere of dinitrogen. Samples were prepared a glovebox, sealed, and covered in tinfoil to protect the sample from light during cyclic voltammetry. Measurements were carried out using a VersaSTAT (Princeton Applied Research) potentiostat. A conventional three electrode system was employed consisting of a glassy carbon electrode (diameter = 0.4 cm), used as the working electrode, a Pt wire, or a glassy carbon rod as the counter electrode, and a silver wire as the pseudo-reference electrode was used and referenced to the ferrocene/ferrocenium couple internal standard. For bulk electrocatalytic experiments, a glassy carbon rod (diameter = 0.4cm; length = 2cm) was used as the working

electrode, a coiled Pt wire as the auxiliary electrode, and were referenced to a silver wire acting as a pseudo-reference electrode.

For the Electrophotochemistry experiments, the electrochemical setup remained the same however with the addition of either a blue LED light or the use of a Xenon lamp providing white light which was used to access the UV-light region.

References

(1) Yang, X.; Wang, D. Photocatalysis: From Fundamental Principles to Materials and Applications. *ACS Appl. Energy Mater.* **2018**, *1* (12), 6657–6693. https://doi.org/10.1021/acsaem.8b01345.

(2) Lingampalli, S. R.; Ayyub, M. M.; Rao, C. N. R. Recent Progress in the Photocatalytic Reduction of Carbon Dioxide. *ACS Omega* **2017**, *2* (6), 2740–2748. https://doi.org/10.1021/acsomega.7b00721.

(3) Ulmer, U.; Dingle, T.; Duchesne, P. N.; Morris, R. H.; Tavasoli, A.; Wood, T.; Ozin, G. A. Fundamentals and Applications of Photocatalytic CO2 Methanation. *Nat Commun* **2019**, *10* (1), 3169. https://doi.org/10.1038/s41467-019-10996-2.

(4) Ge, P.; Hojeij, M.; Scanlon, M. D.; Girault, H. H. Photo-recycling the Sacrificial Electron Donor: Towards Sustainable Hydrogen Evolution in a Biphasic System. *ChemPhysChem* **2020**, *21* (24), 2630–2633. https://doi.org/10.1002/cphc.202000844.

(5) Wang, L.; Rörich, I.; Ramanan, C.; Blom, P. W. M.; Huang, W.; Li, R.; Zhang, K. A. I. Electron Donor-Free Photoredox Catalysis via an Electron Transfer Cascade by Cooperative Organic Photocatalysts. *Catal. Sci. Technol.* **2018**, *8* (14), 3539–3547. https://doi.org/10.1039/C8CY01072B.

(6) Banoth, P.; Kandula, C.; Kollu, P. Introduction to Electrocatalysts. In *ACS Symposium Series*; Gupta, R. K., Ed.; American Chemical Society: Washington, DC, 2022; Vol. 1432, pp 1–37. https://doi.org/10.1021/bk-2022-1432.ch001.

(7) Krischer, K.; Savinova, E. R. Fundamentals of Electrocatalysis. In *Handbook of Heterogeneous Catalysis*; Weinheim, Germany, 2008;. https://doi.org/10.1002/9783527610044.hetcat0101.

(8) Rotundo, L.; Grills, D. C.; Gobetto, R.; Priola, E.; Nervi, C.; Polyansky, D. E.; Fujita, E. Photochemical CO 2 Reduction Using Rhenium(I) Tricarbonyl Complexes with Bipyridyl-Type

Ligands with and without Second Coordination Sphere Effects. *ChemPhotoChem* **2021**, *5* (6), 526–537. https://doi.org/10.1002/cptc.202000307.

(9) He, J.; Bai, Z.-Q.; Yuan, P.-F.; Wu, L.-Z.; Liu, Q. Highly Efficient Iridium-Based Photosensitizers for Thia-Paternò–Büchi Reaction and Aza-Photocyclization. *ACS Catal.* **2021**, *11* (1), 446–455. https://doi.org/10.1021/acscatal.0c05005.

(10) Prier, C. K.; Rankic, D. A.; MacMillan, D. W. C. Visible Light Photoredox Catalysis with Transition Metal Complexes: Applications in Organic Synthesis. *Chem Rev* **2013**, *113* (7), 5322–5363. https://doi.org/10.1021/cr300503r.

(11) Morgan, J. W.; Anders, E. Chemical Composition of Earth, Venus, and Mercury. *Proc. Natl. Acad. Sci. U.S.A.* **1980**, *77* (12), 6973–6977. https://doi.org/10.1073/pnas.77.12.6973.

(12) Kim, H.; Kim, H.; Lambert, T. H.; Lin, S. Reductive Electrophotocatalysis: Merging Electricity and Light To Achieve Extreme Reduction Potentials. *J. Am. Chem. Soc.* **2020**, *142* (5), 2087–2092. https://doi.org/10.1021/jacs.9b10678.

(13) Cowper, N. G. W.; Chernowsky, C. P.; Williams, O. P.; Wickens, Z. K. Potent Reductants via Electron-Primed Photoredox Catalysis: Unlocking Aryl Chlorides for Radical Coupling. *J. Am. Chem. Soc.* **2020**, *142* (5), 2093–2099. https://doi.org/10.1021/jacs.9b12328.

(14) Yarnell, J. E.; Deaton, J. C.; McCusker, C. E.; Castellano, F. N. Bidirectional "Ping-Pong" Energy Transfer and 3000-Fold Lifetime Enhancement in a Re(I) Charge Transfer Complex. *Inorg. Chem.* **2011**, *50* (16), 7820–7830. https://doi.org/10.1021/ic200974h.

(15) Liu, D.; Yu, H.; Wang, Z.; Nie, Q. Synthesis and Fluorescence Properties of Novel 1,10-Phenanthroline-Functionalized Polyaryletherketone and Its Rare Earth Complexes: Phenanthroline-Functionalized PEK and Its Rare Earth Complexes. *Polym. Int.* **2010**, *59* (7), 937–944. https://doi.org/10.1002/pi.2810.

(16) Shamshinova, V. V.; Kokorin, A. I.; Kolosova, E. M.; Yaroslavov, A. A. Synthesis of Polymers Containing O-Phenanthroline Groups and Study of Their Complexing with Copper(II) Ions. *Russ Chem Bull* **1986**, *35* (12), 2476–2479. https://doi.org/10.1007/BF01474201.

(17) Yarnell, J. E.; Wells, K. A.; Palmer, J. R.; Breaux, J. M.; Castellano, F. N. Excited-State Triplet Equilibria in a Series of Re(I)-Naphthalimide Bichromophores. *J. Phys. Chem. B* **2019**, *123* (35), 7611–7627. https://doi.org/10.1021/acs.jpcb.9b05688.

(18) Tignor, S. E.; Kuo, H.-Y.; Lee, T. S.; Scholes, G. D.; Bocarsly, A. B. Manganese-Based Catalysts with Varying Ligand Substituents for the Electrochemical Reduction of CO_2 to CO. *Organometallics* **2019**, *38* (6), 1292–1299. https://doi.org/10.1021/acs.organomet.8b00554.

(19) Pérez-Arredondo, M. de la L.; González-Ponce, M. del R.; Ana Zanor, G.; Ramirez Vazquez, J. A.; Segoviano-Garfias, J. J. N. Complex Formation Equilibria of 2,2′-Bipyridyl and

1,10-Phenanthroline with Manganese(II) in Methanol. *Karbala International Journal of Modern Science* **2015**, *1* (3), 178–186. https://doi.org/10.1016/j.kijoms.2015.11.005.

(20) Yang, Y.; Doettinger, F.; Kleeberg, C.; Frey, W.; Karnahl, M.; Tschierlei, S. How the Way a Naphthalimide Unit Is Implemented Affects the Photophysical and -Catalytic Properties of Cu(I) Photosensitizers. *Front. Chem.* **2022**, *10*, 936863. https://doi.org/10.3389/fchem.2022.936863.

(21) Kuo, H.-Y.; Lee, T. S.; Chu, A. T.; Tignor, S. E.; Scholes, G. D.; Bocarsly, A. B. A Cyanide-Bridged Di-Manganese Carbonyl Complex That Photochemically Reduces CO_2 to CO. *Dalton Trans.* **2019**, *48* (4), 1226–1236. https://doi.org/10.1039/C8DT03358G.

Chapter 3: Electrocatalytic Hydrogen Production in Neutral Water using an Aqueous Ni(II) pincer complex

Preamble and Context:

This chapter is based on a project that was initiated by Somayeh Norouziyanlakvan (SN), a PhD student in the lab. This work has been published in Catalysis Science and Engineering and can be accessed at https://doi.org/10.1039/d2cy01504h . My major contributions were to perform all controlled potential coulometry experiments, gas analysis, product characterization and quantification, and all figures related to those tasks. These experiments were key to completion of this project. SN performed the initial complex synthesis and characterization and the first electrochemical measurements that indicated catalytic behavior. DFT calculations and their analysis were performed by Dr. Darrin Richeson (DR) with feedback from both SN and myself. The manuscript was prepared by DR, SN and myself.

Introduction:

Energy consumption in today's rapidly expanding economy and worldwide population is a topic of increasing significance. While energy demands have been largely met through fossil fuel combustion, it is now established that the resulting greenhouse gases that are emitted into the atmosphere are a leading cause of climate change and harmful to life on Earth. Hydrogen can provide a clean source of energy that could address these issues. The electrocatalytic hydrogen evolution reaction (HER) from water, could provide a sustainable and green approach to providing renewable energy.

In this context, researchers strive to discover and evaluate efficient catalysts for HER with a particular focus on employing earth abundant metal complexes for this goal. While some

hydrogen evolution catalysts require large negative potentials and acidic conditions to operate, there are reported molybdenum, cobalt and nickel complexes that are capable of hydrogen generation at less negative potentials.[1–7] Unfortunately, most of these catalysts are only soluble in organic solvents or utilize organic acids to achieve H_2 production. A more sustainable approach and a challenging ongoing effort targets hydrogen generation catalysts that are soluble in water and require no added proton sources. There are a limited number of reported electrocatalysts that are active for HER in neutral water.[8–15] Long. et al. reported a molybdenum-oxo catalyst for generating hydrogen from water without any added acid or organic cosolvents with a high turnover number (TON).[16] In 2011, Chang. et al. reported a cobalt complex supported by a pentadentate polypyridyl ligand "$PY5Me_2$" which showcases a 100% Faradaic efficiency and high stability and activity for the HER from neutral water.[17]

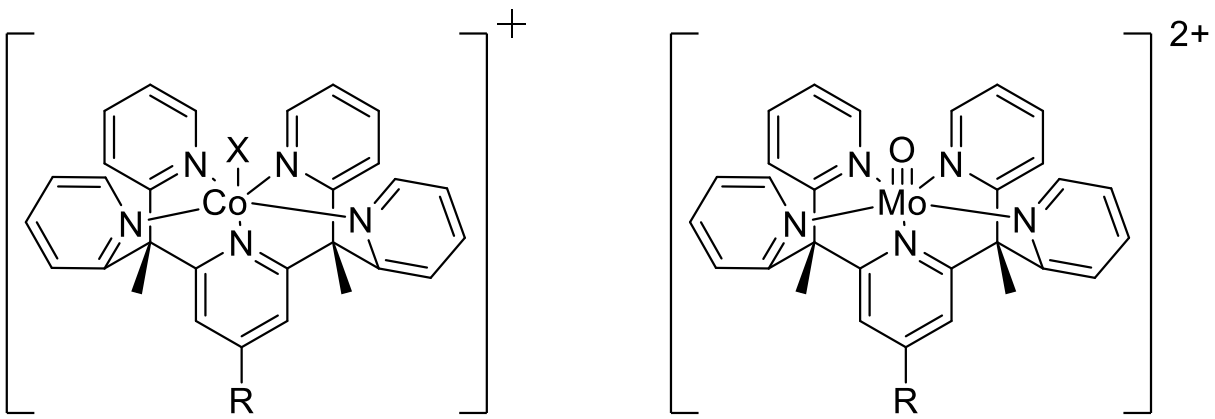

Scheme 1: Catalysts bearing the $PY5Me_2$ ligand used for HER.

Nickel complexes are attractive targets for the HER in an aqueous environment partly due to the role of Ni in hydrogenase enzymes as well as their documented activity as hydrogen evolution catalysts.[18,19] We envisioned that appropriate ligand design could be employed to prepare Ni complexes as water soluble catalysts. For example, diiminopyridine (DIMPY) ligands

are well-known pincer ligands that support a wide range of metal complexes and are established as non-innocent ligands, which are capable of operating as an electron reservoir and often exhibit high catalytic activity and selectivity.[20] Furthermore, Ni complexes of these ligands are well-known and are often stable in aqueous solution. Finally, Ni DIMPY complexes are reported to be effective catalysts for H_2 production. However, these reports are either in organic solvents or acidic aqueous media.[14,21,22] As a result of these features we undertook to investigate the HER activity of a simple Ni(II) diminopyridine complex in neutral pH, aqueous saline solution and discovered that this compound produced hydrogen from water at potentials as low as -1.0 V versus. Ag/AgCl electrode.

Results & Discussion:

The target complex [Ni(κ^3-2,6-{PhNCMe}$_2$(NC_5H_3)Br_2] (**1**) was readily prepared by adding $NiBr_2$ to a room temperature toluene solution of the diiminopyridine ligand, 2,6-{PhNCMe}$_2$(NC_5H_3) as shown in Fig. 1. In addition to the synthesis, SN obtained the single crystal X-ray analysis of this orange product, and the results are shown in Fig. 1.

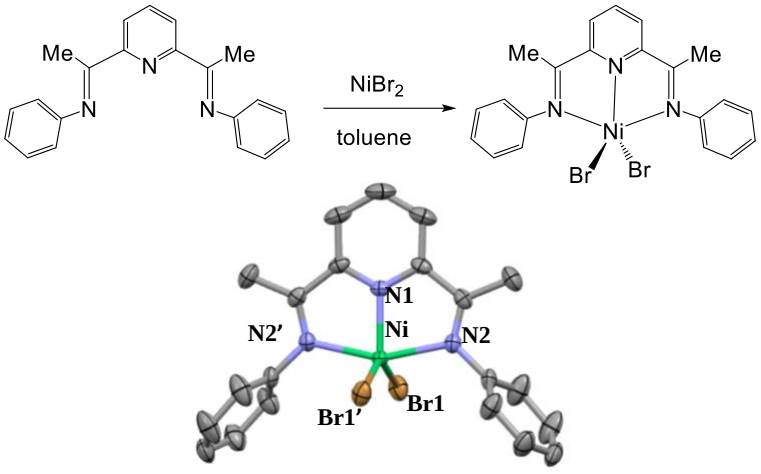

Figure 1: Reaction scheme for the preparation of [Ni(κ^3-2,6-{PhNCMe}$_2$(NC_5H_3)Br_2] (**1**) and a representation of the single crystal XRD structure of **1** with selected atoms labeled and hydrogens atoms omitted for clarity.

Although this compound had previously been reported in the literature it had not been structurally characterized.[23] The structural analysis confirmed that compound **1** presented a trigonal bipyramidal Ni(II) center with a coordination environment consisting of a neutral planar tridentate diminopyridine and two bromo ligands (Fig. 1). Selected bonding parameters are given in Table 1. Not surprisingly, the bonding parameters were similar to the dichloro analogue, [Ni(κ^3-2,6-{PhNCMe}$_2$(NC_5H_3)Cl_2].[22]

Table 1: Selected Bond lengths (Å) and angles (°) for (**1**).

Bond lengths [Å]		**Bond angles [°]**	
Br(1)-Ni(1)	2.3967	N(1)-Ni(1)-N(2)	78.1
Ni(1)-N(1)	1.947	Br(1)-Ni(1)-N(1)	112.41
Ni(1)-N(2)	2.114	Br(1)-Ni(1)-N(2)	96.40
N(1)-C(3)	1.338	Br(1)-Ni(1)-Br(2)	135.18
N(2)-C(4)	1.278(4)	Ni(1)-N(1)-C(3)	118.8
N(2)-C(6)	1.436(4)	Ni(1)-N(2)-C(4)	114.7
C(1)-C(2)	1.381	Ni(1)-N(2)-C(6)	123.7
C(2)-C(3)	1.388(4)	C(4)-N(2)-C(6)	121.5(3)
C(4)-C(5)	1.491(5)	C(3)-C(4)-C(5)	119.8(3)

Interestingly and consistent with a five-coordinate Ni(II), **1** was paramagnetic in the solid state. However, in solution, compound **1** gave a ^{1}H NMR spectrum consistent with a symmetrical ligand and suggesting autoionization to yield a low-spin diamagnetic Ni(II) species, [Ni(κ^3-2,6-{PhNCMe}$_2$(NC_5H_3)Br]$^+$ (**1'**$^+$) schematically represented in Figure 2. [14,22,24] Support for these

observations came from attempts to computationally optimize structure **1** (DFT, B3LYP, def2-TZVP) using the PCM model for solvation in acetonitrile, which resulted in spontaneous dissociation of one of the Br^- ligands and rearrangement of the Ni center to a square planar geometry (Figure 2).

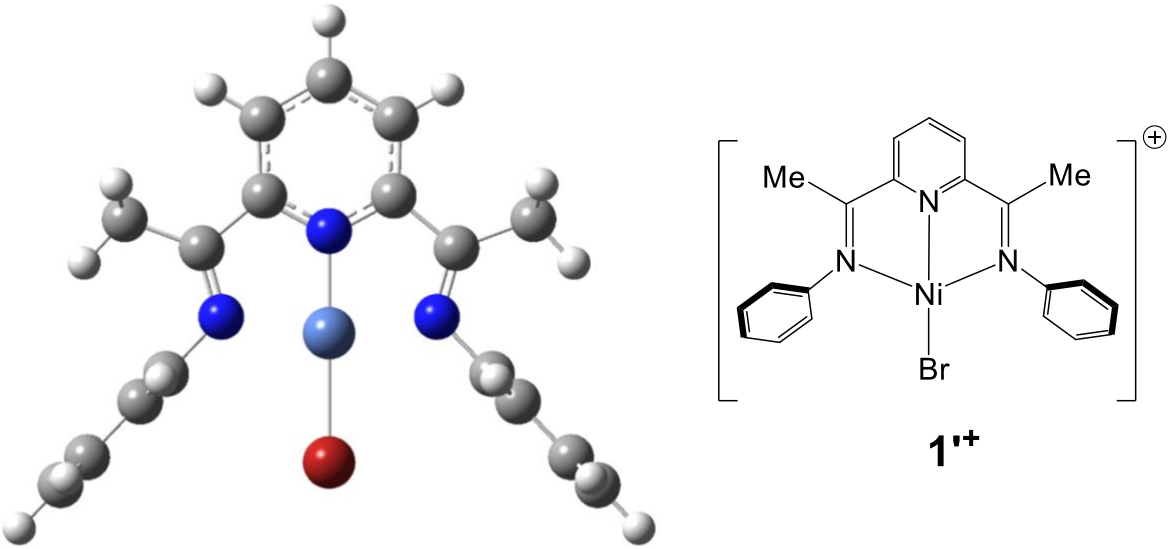

Figure 2: Structural figures for compounds $1'^{+}$ and the result form computational optimization. (DFT, B3LYP, def2-TZVP) using the PCM model for solvation in acetonitrile.

In coordinating solvents, such as water, these cations are known to undergo a subsequent ligand substitution reaction of the bromo ligand by water to yield square planar Ni aquo species $[Ni(\kappa^3\text{-}2,6\text{-}\{PhNCMe\}_2(NC_5H_3)(OH_2)]^{2+}$, **1'(OH$_2$)$^{2+}$** (Figure 3).[14] This aquo complex was also successfully optimized, confirmed by frequency calculations, yielding a structure that is the complement of **1'**$^{+}$ (Fig. S3, Table S4). These results support that in polar/coordinating solvents **1** is a precursor to square planar Ni(II) species.

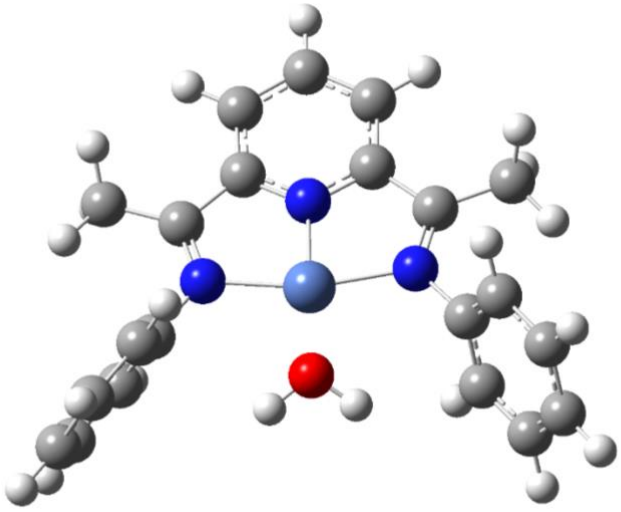

Figure 3: Computationally optimized [Ni(κ^3-2,6-{PhNCMe}$_2$(NC_5H_3)(OH_2)]$^{2+}$ (**1'(OH_2)$^{2+}$**) (DFT, B3LYP, def2-TZVP, PCM in water).

Electrochemical Characterization

The initial electrochemical characterization was carried out by SN and was performed on a 1mM solution in anhydrous acetonitrile with 0.1M Bu4NPF6 as the supporting electrolyte and using a glassy carbon (GC) working electrode, Pt counter electrode, and an Ag pseudo-reference electrode, which was externally referenced to the Fc+/0 couple. The resulting cyclic voltammogram (CV) is displayed in Figure 4. As shown in the blue trace, **1'**$^+$ displayed two reversible reduction events with $E_{1/2}$ = -0.75V and -1.15 V versus. $Fc^{+/0}$. Both redox events displayed a linear relationship of the square root of scan speed ($\nu^{1/2}$) versus current (i) consistent with a diffusion-controlled process. [25]

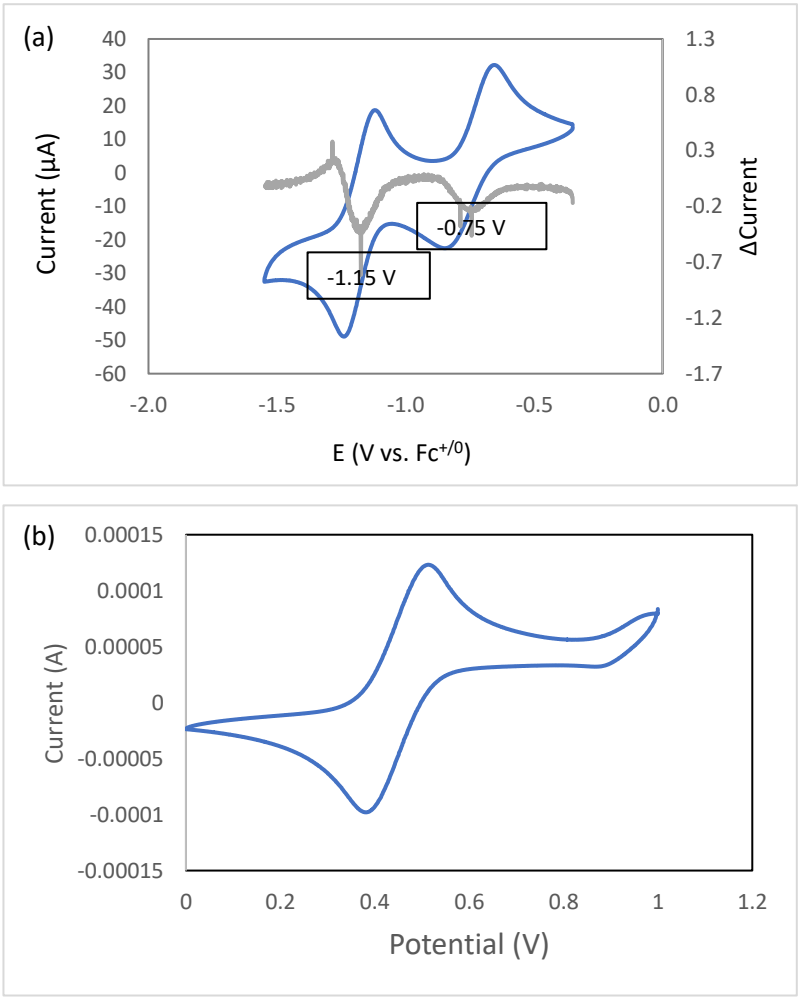

Figure 4: (a) Cyclic voltammogram of [Ni(κ^3-2,6-{PhNCMe}$_2$(NC$_5$H$_3$)Br]$^+$ (**1'**$^+$) (1mM) in CH$_3$CN with 100mM TBAPF$_6$ using a glassy carbon (GC) working electrode. Potentials are referenced to Fc/Fc$^+$. A quasireversible and reversible reduction peaks were observed with $E_{1/2}$ of -0.75 V and -1.15 V, respectively. The gray markers represent application of the method of first principles to the blue curve. Minima denote inflection points in the catalytic curve and indicate the associated onset potential and current enhancement. (b) Cyclic voltammogram of ferrocene (1mM) as a reference in CH$_3$CN with 100mM TBAPF$_6$ using a glassy carbon (GC) working electrode. The DE_p value was 131mV.

All these observations are consistent with reported electrochemical characterization of related diiminopyridine Ni(II) species. The first reduction has been assigned to addition of an electron to a ligand centered orbital while the second electron is placed in a metal-centered (dx^2-y^2) orbital.[14,22] These results were confirmed by a computational optimization of the doubly reduced species, [Ni(κ^3-2,6-{PhNCMe}$_2$(NC$_5$H$_3$)Br]$^-$ (**1'**$^-$), which gave a triplet state with one

singly occupied molecular orbital (SOMO) being a ligand -centered π* orbital delocalized across the pyridyl (48%) and imine (40%) moieties and the other being a metal-centered SOMO dominated by Ni dx^2-y^2 (41%) that was σ* in nature.

A central goal of our efforts is to employ water as a sustainable and green solvent and this prompted the electrochemical characterization of the aquo complex $[Ni(\kappa3\text{-}2,6\text{-}\{PhNCMe\}_2(NC_5H_3)(OH_2)]^{2+}$, **1'(OH$_2$)$^{2+}$** that would be generated by dissolving **1** in water. A CV of an aqueous solution of **1** (1mM) with KBr (100mM) as supporting electrolyte under cathodic potentials is shown in Fig. 5(a). Identical measurements were obtained in water and in aqueous phosphate buffer (pH=7). Here, two irreversible reduction events along with a single oxidation were observed. To more accurately assign the onset potentials for these reductions the reduction potential inflection points were identified by the derivative of the E vs. i plots using the method of first principles. These inflection points were used for the assignment of the potentials -0.95 V and -1.05 V versus. Ag/AgCl.[26] Significantly, the two reductions follow the Randles–Ševčík equation, yielding a linear relation for i versus. $\nu^{1/2}$ as expected for a homogeneous diffusion-controlled process at the electrode/solution interface.

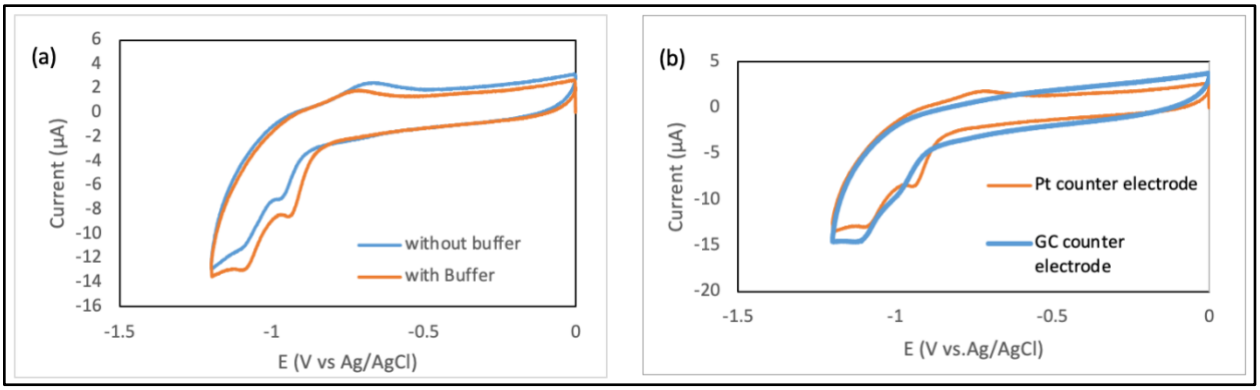

Figure 5: Cyclic voltammogram of complex $[Ni(\kappa^3\text{-}2,6\text{-}\{PhNCMe\}_2(NC_5H_3)(OH_2)]^{2+}$ (**1'(OH$_2$)$^{2+}$**) (1mM) in presence of 100mM KBr in H_2O using a glassy carbon (GC) working electrode, Ag/AgCl reference electrode. (a) Using a Pt counter electrode with (orange) and without (blue) 0.3M phosphate buffer pH=7. (b) Comparison of using Pt or GC counter electrode under the same conditions. Reductions at -0.95 V and -1.05 V and oxidation at -0.5V.

The nature of the doubly reduced aquo species (1'(OH_2)) was examined through a computational optimization using the B3LYP functional, def2-TZVP basis set with the PCM solvation model in water. Frequency analysis validated that this led to a minimum structure. As observed for **1'**$^{+}$, the lower energy electronic state for **1'(OH_2)** was a triplet state. The frontier orbitals of 1'(OH_2) are shown in Figure 6 and were dominated by five metal centered d orbitals and two π* orbitals of the ligand. The two singly occupied molecular orbitals (SOMOs) are constituted from the Ni dx^2-y^2 that was σ* in nature and a π* ligand centered on pyridyl and imine groups. The next four lower energy molecular orbitals (MO 98-101) were Ni centered dxy dyz, dxz and dz^2, respectively, and consistent with a square planar ligand field. This interpretation suggests that the starting Ni(II) species, [Ni(κ^3-2,6-{PhNCMe}$_2$$NC_5H_3$)($OH_2$)]$^{2+}$ (**1'(OH_2)$^{2+}$**), was reduced to a formally d^9 Ni(I) complex bearing a negatively charged diiminopyridine ligand, [Ni(κ^3-2,6-{PhNCMe}$_2$$NC_5H_3$)($OH_2$)] (**1'($OH_2$)**). As expected, the reduced complex displayed slightly decreased ligand/metal Mayer bond orders and increased bond distances compared to the original cation, **1'(OH_2)$^{2+}$** (Table 2).

Table 2: Selected bond parameters for computationally optimized [Ni(κ^3-2,6-{PhNCMe}$_2$$NC_5H_3$)($OH_2$)] (**1'($OH_2$)**). The product of the second reduction of **1'(OH_2)$^{2+}$**).

Bond	**Length(Å)**	**Mayer Bond order**
Ni-N_{py}	1.913	0.6058021
Ni-N_{imine}	2.087	0.4681138
Ni-N_{imine}	2.127	0.4131332
Ni-O	2.101	0.2051176

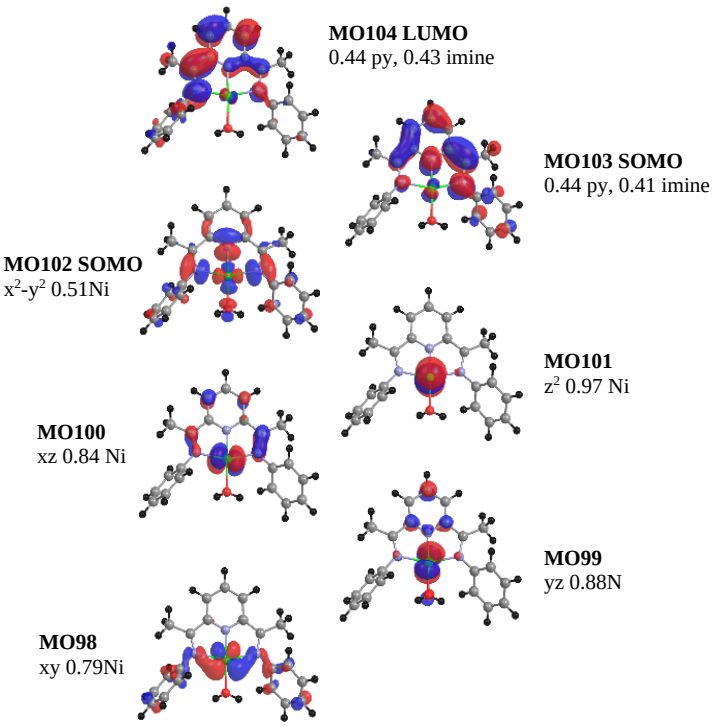

Figure 6: Frontier molecular orbitals obtained for the optimization of [Ni(κ^3-2,6-{PhNCMe}$_2$NC$_5$H$_3$)(OH$_2$)] (**1'(OH$_2$)**), the second reduction of (**1'(OH$_2$)$^{2+}$**). Obtained using the B3LYP functional, def2TZVP basis set and PCM model for solvation in water. Major fragment orbital contributions were visualized using the Chemissian program using a 0.03 isosurface.

Electrocatalytic H_2 Production

The examination of the ability of **1** to function as a precatalyst for electrocatalytic H_2 generation was first examined in nonaqueous polar solvents. Dissolution in acetonitrile (MeCN), led to the cationic species $[Ni(\kappa^3\text{-}2,6\text{-}\{PhNCMe\}_2(NC_5H_3)Br]^+$ (**1'**$^+$). The literature contains reports that related complexes are capable of reducing acidic protons to hydrogen and we found that **1'**$^+$ was able to generate H_2 using trifluoracetic acid (TFA) as the proton source in MeCN. Figure 7 shows the effect of added TFA on the cyclic voltammograms of acetonitrile solution of **1'**$^+$ and indicates a large catalytic wave at E = -1.20 V versus $Fc^{+/0}$.

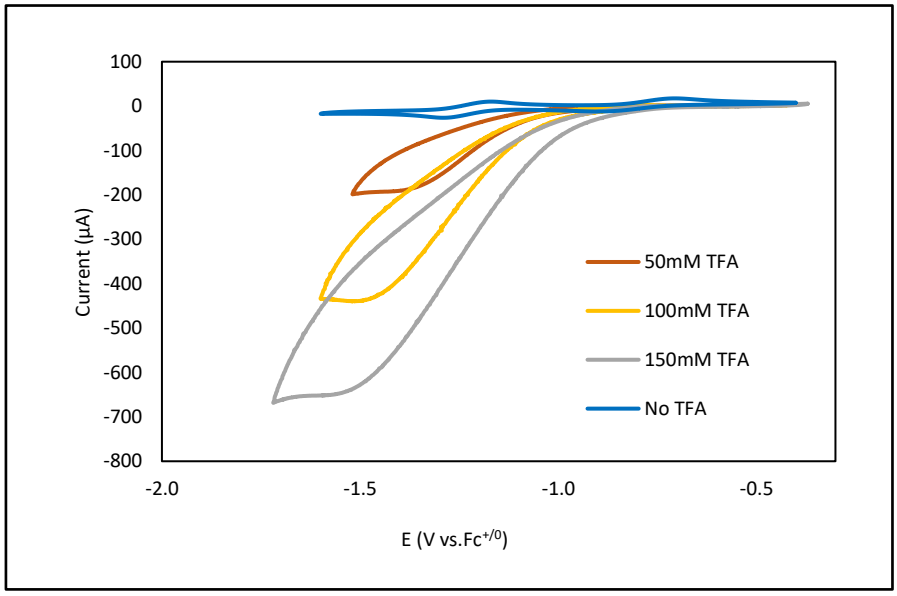

Figure 7: Cyclic voltammograms of **1'**$^+$ (1mM) in presence of $TBAPF_6$ (100mM) in CH_3CN using a GC working electrode (blue) and with various concentrations of trifluoroacetic acid (TFA). Potentials were referenced $Fc^{+/0}$.

The overpotential for the proton reduction can be determined by first calculating the theoretical proton reduction potential value, $E^T_{1/2}$, in acetonitrile, obtained from equation 1, and subtracting this value from the experimental onset potential.[27,28] For TFA in acetonitrile, the *pKa* value is 12.7 and the homoconjugation constant, K_c is $10^{3.7}$, ε_D is the

relative diffusion rate of products to reactants, C^0 is the concentration of proton source, and $C^0_{H_2}$ is the maximum concentration of H_2 in solution. Using these values the $E^T_{1/2}$ is -645 mV corresponding to an overpotential of 555 mV for **1'**$^+$.

$$E^T_{1/2} = E^0_{H^+/H_2} - (\frac{2.303RT}{F})pK_a + e_D + (\frac{RT}{2F})ln(K_c^2 C^0 C^0_{H_2}) \quad (\mathbf{1})$$

The effect of increasing TFA concentration on the catalytic current, i_{cat}, and the TFA concentration dependence of i_{cat}/i_p were also determined. A plot of catalytic current (i_{cat}) as a function of acid concentration revealed an initial linear acid concentration dependence that begins to plateau at ~0.5M TFA where the reaction shifts to a pseudo-zero order rate indicative of saturation conditions (Figure 8).

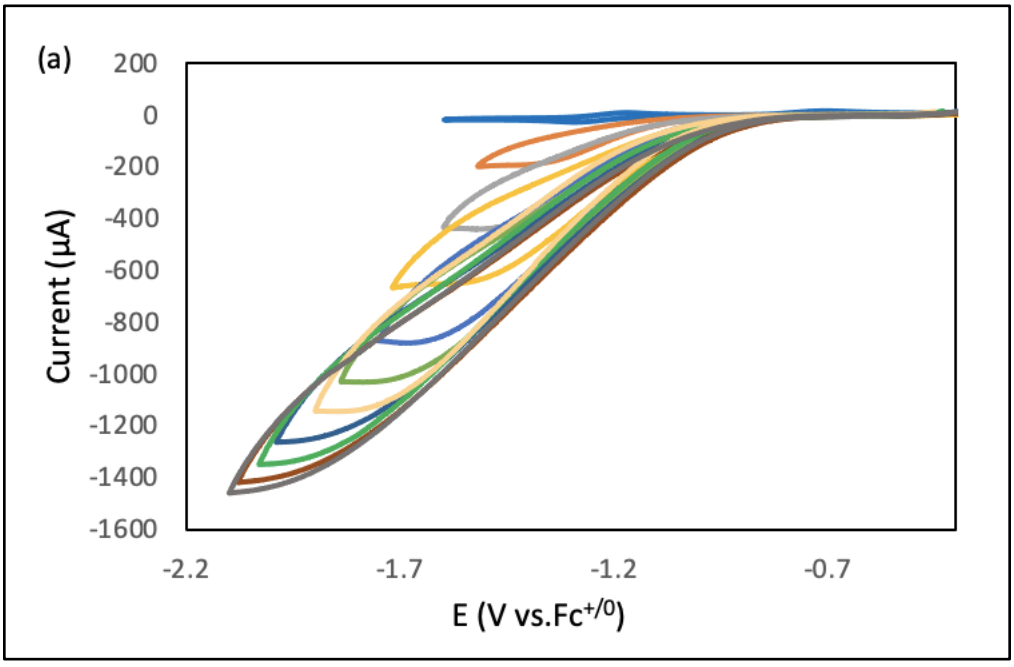

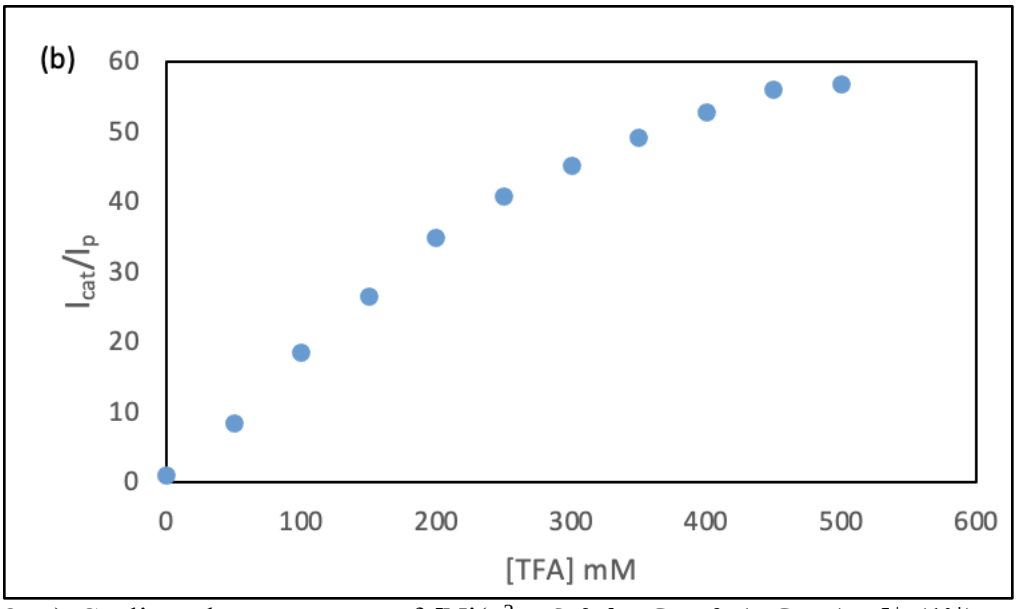

Figure 8: a) Cyclic voltammograms of [Ni(κ^3-2,6-{PhNCMe}$_2$(NC_5H_3)Br]$^+$ (**1'**$^+$) with varying concentrations of TFA in CH_3CN with 0.1 M tetrabutylammonium hexafluorophosphate ($TBAPF_6$) supporting electrolyte at 100 mV/s using a glassy carbon (GC) working electrode. (b) Corresponding plot of i_{cat}/i_p vs TFA concentration.

This relationship can be expressed using equation 2 where TOF is the catalyst turnover frequency and n is the scan rate.[29,30] In the case of **1'**$^+$ at υ = 100 mV/s the TOF for hydrogen production from TFA at -1.2V of 639 s^{-1}.

$$\frac{i_{cat}}{i_p} = \frac{2}{0.446}\sqrt{\frac{RT(TOF)}{F\upsilon}} \quad (2)$$

A controlled potential coulometry (CPC) experiment demonstrated that under these conditions and over 2 hours, **1'**$^+$ catalytically produced 512µmol of H_2 with an 85% Faradaic efficiency (FE).

Our next avenue of investigation was to shift the hydrogen source to water which represents a sustainable source for H_2 production and provides an ideal solvent for the electrocatalytic reaction. Therefore, we initiated an exploration of the ability of Ni(κ^3-2,6-{PhNCMe}$_2$$NC_5H_3$)($OH_2$)]$^{2+}$ (**1'(OH$_2$)$^{2+}$**) for electrocatalytic hydrogen generation in aqueous solutions. Clearly the consumption of protons from water would lead to an increase

in hydroxide ions and an increase in solution pH. This was documented by two experiments. First, the pH of a controlled potential coulometry experiment with **1'(OH$_2$)$^{2+}$** was monitored for 2 hours and showed a steady increase of pH from 6.5 to 7.2. Second, the current response during a controlled potential electrolysis was monitored for both buffered (0.3M phosphate, pH 7) and unbuffered solutions of **1'(OH$_2$)$^{2+}$**. The buffered solution displayed a substantial increase in current compared to the unbuffered system. Importantly, the presence of buffer had no significant effect on the CV behavior of **1'(OH$_2$)$^{2+}$** as previously shown in Figure 5(a).

Electrocatalytic hydrogen production with **1'(OH$_2$)$^{2+}$** was confirmed by coulometry in buffered (pH 7) saline (KBr) solution at -1.1 V versus Ag/AgCl. The effect of using a buffered solution resulted in a significant quantitative effect for H_2 production leading to a ten-fold increase in H_2 and an improvement in Faradaic efficiency to 96% (Table 3).

Table 3: Bulk results for **1** at -1.0V (V vs. 3.0M KCl Ag/AgCl) with varying catalyst concentrations and times.

[cat] (mM)	E (V vs. Ag/AgCl)	time (h)	µmol H2	Faradaic Efficiency (%)	Solution
1	-1.1	2	4.43	89	No buffer
0.5	-1.1	2	34.74	76	0.3M Phosphate buffer
1	-1.1	2	45.43	96	0.3M Phosphate buffer
1	-1.1	18	415	23	0.3M Phosphate buffer
1	-1.2	2	110	78	0.3M Phosphate buffer
2	-1.2	2	19.17	77	0.3M Phosphate buffer

The catalytic behavior of **1'(OH$_2$)$^{2+}$** and the absence of interference from the Pt counter electrode was further supported by two CPC measurements - one carried out in the absence of added complex, which yielded only trace amounts of H_2 and another in which a

GC rod was used as the counter electrode and where 40mmol of H_2 (FE = 72%) was produced in 2 hours.

The homogeneous behavior of **1'(OH$_2$)$^{2+}$** was further supported by several control experiments. Repeated linear sweep voltammetry measurements of the catalyst/substrate systems were carried out to confirm catalytic current enhancement. Following these sweeps, the electrode was removed, carefully rinsed with clean solvent, and placed into a fresh solution containing substrate but no catalyst. Voltammetry measurements on these catalyst free systems did not exhibit any electrochemical events, indicating that the catalyst had not deposited on the electrode surface following electrolysis. These measurements indicated that the catalyst had not transformed during electrolysis. Finally, CV measurements on aqueous solutions of **1** (0.5 to 1mM) with 100 mM KBr showed an increase in peak current with an increase in nickel concentration, which is consistent with a homogeneous system.

Proposed Mechanism for H_2 Production from Water

A proposed mechanism for the catalytic H_2 generation by **1'(OH$_2$)$^{2+}$** is presented in Figure 9. DFT Calculations provided additional support for this proposition with [Ni(κ^3-2,6-{PhNCMe}$_2$(NC_5H_3)Br_2] (**1**) as a precatalyst. As shown in Figure 9, the square planar d^8 complex [Ni(κ^3-2,6-{PhNCMe}$_2$(NC_5H_3)OH_2)]$^{2+}$ (**1'(OH$_2$)$^{2+}$**) arises from the dissolution of **1** in water. The production of H_2 at -1.1V versus Ag/AgCl correlates with the second reduction of **1'(OH$_2$)$^{2+}$** and computations supported that this doubly reduced species a triplet state with the frontier orbitals shown in Fig. 6.

At this stage the **1'(OH$_2$)** is an electron-rich, basic complex that can abstract a proton from water. The highest energy lone electron pair is a nonbonding pair in a Ni-centered dz^2 orbital (Fig. 6,

MO 101). Addition of a proton to this site would lead to a cationic species [Ni(κ^3-2,6-{PhNCMe}$_2$(NC_5H_3)(OH_2)(H)]$^+$, shown as **A** in equation 3. Attempts to carry out a computational optimization for the proposed species **A** using B3LYP/def2TZVP and modelling with water solvation, spontaneously led to a rearrangement with loss of the coordinated aquo ligand and formation of square planar hydride species, [Ni(κ^3-2,6-{PhNCMe}$_2$$NC_5H_3$)H]$^+$ (**Ni(II)H**).

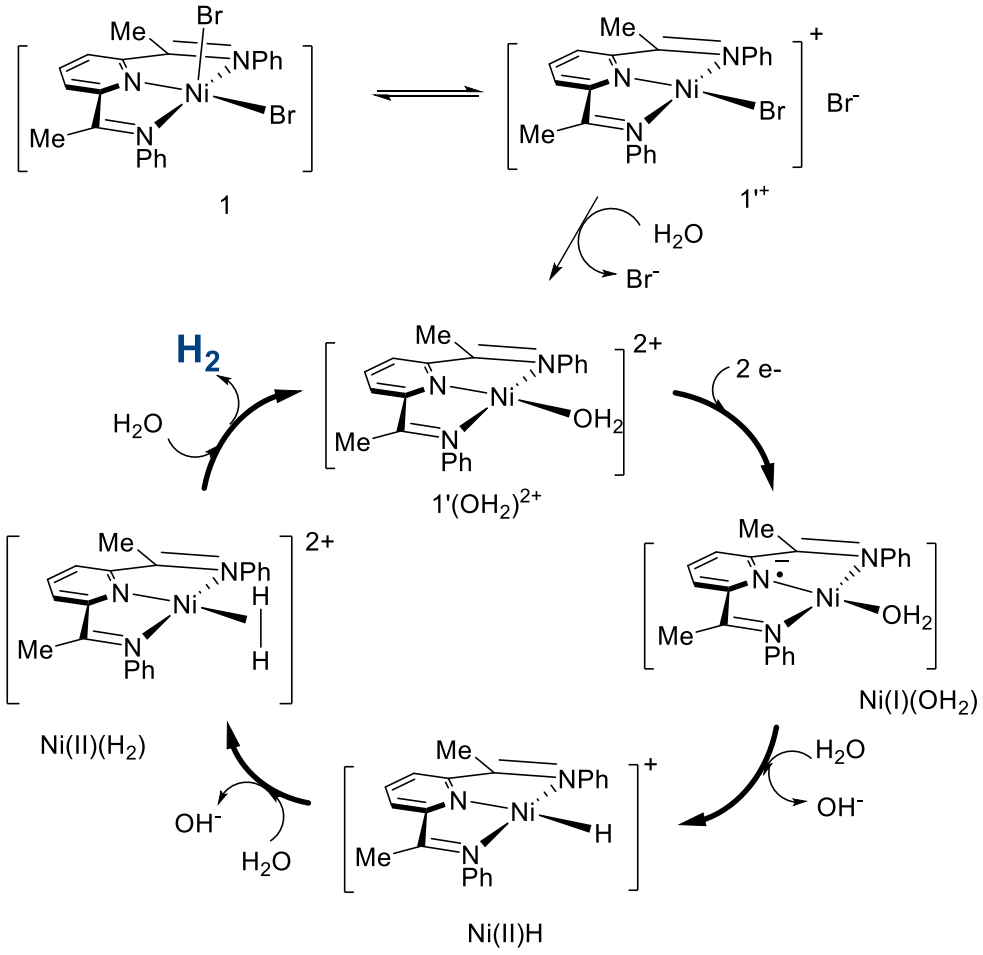

Figure 9: A computationally supported (B3LYP/def2TZVP/PCM(water)) proposed mechanism for the electrocatalytic hydrogen evolution from [Ni(κ^3-2,6-{PhNCMe}$_2$(NC_5H_3)(OH_2)]$^{2+}$ with H_2O as the substrate and solvent.

This proposed species has the Ni center in a divalent oxidation state and a d^8 configuration. A molecular orbital analysis confirmed that the HOMO is Ni-centered and largely dz^2 in character

with the LUMO derived from a π* MO on the pyridyl and imine groups. The remaining metal d-centered orbitals reflect the ligand field splitting expected for a square planar Ni. With the highest energy electron pair in a dz^2-based MO, proton abstraction from water could be envisioned as the next reaction step.

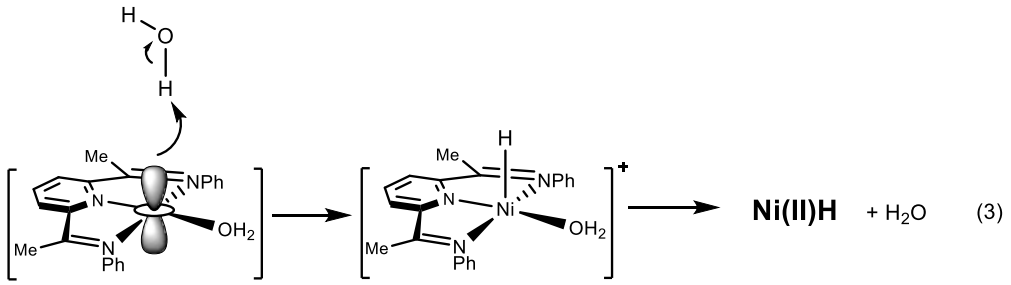

Equation 3: Addition of a proton to the Ni dz^2 leading to the formation of a cationic species

Once again, addition of a proton to Ni along this z-axis with an attempted computational optimization (B3LYP/def2TZVP/PCM(water)) of such a proposed species resulted in a smooth impromptu molecular rearrangement to a minimum energy structure as a dihydrogen complex, $[Ni(\kappa^3\text{-}2,6\text{-}\{PhNCMe\}_2NC_5H_3)(H_2)]^+$ (**Ni(II)(H_2)**) (Fig. 9). Simple substitution by water and release of H_2 from **Ni(II)(H_2)** regenerates the Ni^{II}, d^8 starting material, **1'(OH_2)$^{2+}$** , to close the cycle.

Proposed Mechanism for H_2 Production from TFA in Acetonitrile

A computational analysis informed our proposed mechanism and suggested some key differences from the reaction observed in water. The results of this analysis are presented in Figure **10**. Again, starting from $[Ni(\kappa^3\text{-}2,6\text{-}\{PhNCMe\}_2(NC_5H_3)Br_2]$ (**1**) as a precatalyst the square planar d^8 complex $[Ni(\kappa^3\text{-}2,6\text{-}\{PhNCMe\}_2(NC_5H_3)Br)]^+$ (**1'$^+$**) arises from the dissolution of **1** in acetonitrile. The production of H_2 at -1.2V versus $Fc^{+/0}$ corresponds to the second reduction of **1'$^+$**

and calculations supported that this doubly reduced species exists in a triplet state ground state with SOMO orbitals.

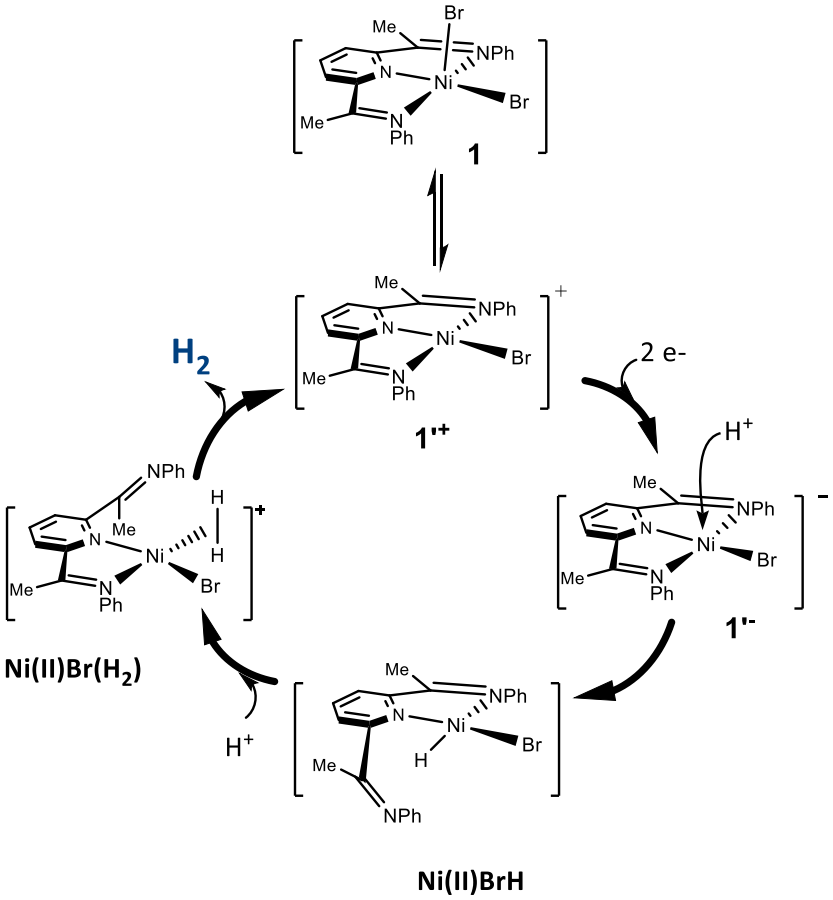

Figure 10: A computationally supported (B3LYP/def2TZVP/PCM(acetonitrile)) proposed mechanism for the electrocatalytic hydrogen evolution from $[Ni(\kappa^3\text{-}2,6\text{-}\{PhNCMe\}_2(NC_5H_3)Br]^+$ with TFA as the substrate and acetonitrile as the solvent.

This electron-rich, basic complex highest energy lone electron pair is a nonbonding pair in a Ni-centered dz^2 orbital. Addition of a proton to this site and allowing the complex to freely optimize using B3LYP/def2TZVP resulted in a ready rearrangement releasing one of the pincer ligand arms, forming a square planar hydride species, $[Ni(\kappa^2\text{-}2,6\text{-}\{PhNCMe\}_2NC_5H_3)BrH]$ (**Ni(II)BrH**). This proposed species has the

Ni center in a divalent oxidation state and a d^8 configuration. The addition of a second proton to Ni, along this z-axis, followed by a computational optimization (B3LYP/def2TZVP/PCM(acetonitrile)) resulted in the smooth uninitiated rearrangement to yield a minimum energy structure as a dihydrogen complex, [Ni(κ^2-2,6-{PhNCMe}$_2$NC$_5$H$_3$)Br(H$_2$)]$^+$ (**Ni(II)Br(H$_2$)**). After formation of the proposed dihydrogen complex, simple coordination of the free imine arm would release H_2 and regenerate the starting species, completing this cycle.

Conclusions

The work reported in this chapter has revealed some fundamental and practical features for electrocatalytic hydrogen generation from water employing a unique, air-stable Ni species. This Ni (II) complex, [Ni(κ^3-2,6-{PhNCMe}$_2$(NC$_5$H$_3$)Br$_2$] (**1**), was demonstrated to be a competent pre-catalyst for H_2 production with neutral water as a substrate and solvent. Furthermore, this was expanded to include the use of **1** in nonaqueous solvent (acetonitrile) with TFA as a substrate. These experimental results were supported by DFT computational analysis, which revealed the important role of the ligand as electron reservoir in the reduction step as well as parallel but different reaction paths for the two hydrogen formation pathways.

Experimental:

General Methods

Reactions were performed using standard Schlenk techniques under a flow of N_2 gas. All solvents were sparged with nitrogen then dried by passage through a column of activated alumina using an apparatus purchased from Anhydrous Engineering. Deuterated solvents were

dried using activated molecular sieves. All other chemicals were purchased from Sigma-Aldrich and used without further purification. Dried acetonitrile was purchased from Sigma-Aldrich and stored on molecular sieves in a glovebox.

Electrochemistry

All cyclic voltammetry experiments were carried out in a single compartment cell of approximately 50 mL volume under an atmosphere of dinitrogen. Samples were prepared in open-air, sealed, connected to a Schlenk line, and purged with a nitrogen atmosphere. Measurements were carried out using a VersaSTAT (Princeton Applied Research) potentiostat. A conventional three electrode system was employed consisting of a glassy carbon electrode (diameter = 0.4 cm), used as the working electrode, a Pt wire, or a glassy carbon rod as the counter electrode, and an Ag/AgCl electrode was used as a reference electrode. For bulk electrocatalytic experiments, a glassy carbon rod (diameter = 0.4cm; length = 2cm) was used as the working electrode, a coiled Pt wire as the auxiliary electrode, referenced to Ag/AgCl electrode.

Complex Synthesis

Synthesis of complex 1 and additional computational details can be found here: https://doi.org/10.1039/d2cy01504h

Gas Chromatography analysis

Gas samples for the detection of H_2 were taken from the headspace of the 50 mL reaction flask using a an air-tight 250 µL volume syringe. The syringe was filled to the 250 µL mark and injected into a Shimadzu GC-2014 gas chromatogram with a thermal conductivity detector to identify the presence of H_2. Using known concentrations of H_2, a calibration curve was made using the area of the H_2 peaks that were detected by the GC-TCD.

References

(1) E. S. Wiedner, A. M. Appel, S. Raugei, W. J. Shaw and R. M. Bullock, Chem. Rev., 2022, 122, 12427–12474.

(2) L. Tong, L. Duan, A. Zhou and R. P. Thummel, Coord. Chem.Rev., 2020, 402, 213079.

(3) S. Roy, M. Bacchi, G. Berggren and V. Artero, ChemSusChem, 2015, 8, 3632–3638.

(4) V. S. Thoi, Y. Sun, J. R. Long and C. J. Chang, Chem. Soc. Rev., 2013, 42, 2388–2400.

(5) D. Z. Zee, T. Chantarojsiri, J. R. Long and C. J. Chang, Acc. Chem. Res., 2015, 48, 2027–2036.

(6) K. E. Dalle, J. Warnan, J. J. Leung, B. Reuillard, S. Karmel, Isabell and E. Reisner, Chem. Rev., 2019, 119, 2752–2875.

(7) A recent review of heterogenous electrocatalysts: C. Xu, A. R. Puente-Santiago, D. Rodríguez-Padrón, M. J. Muñoz-Batista, M. A. Ahsan, J. C. Noveron and R. Luque, Chem. Soc. Rev., 2021, 50, 4856–4871.

(8) P. V Bernhardt and L. A. Jones, Inorg. Chem., 1999, 38, 5086–5090.

(9) B. B. Beyene, S. B. Mane and C. H. Hung, Chem. Commun., 2015, 51, 15067–15070.

(10) P. Zhang, M. Wang, F. Gloaguen, L. Chen, F. Quentel and L. Sun, Chem. Commun., 2013, 49, 9455–7.

(11) C. Tsay and J. Y. Yang, J. Am. Chem. Soc., 2016, 138, 14174–14177.

(12) A. Begum, G. Moula and S. Sarkar, Chem. - A Eur. J., 2010, 16, 12324–12327.

(13) M. Beley, J. P. Collin, R. Ruppert and J. P. Sauvage, J. Am. Chem. Soc., 1986, 108, 7461–7.

(14) O. R. Luca, S. J. Konezny, J. D. Blakemore, D. M. Colosi, S. Saha, G. W. Brudvig, V. S. Batista and R. H. Crabtree, New J. Chem., 2012, 36, 1149.

(15) G. K. Rao, M. P. Jamshidi, J. I. G. Dawkins, W. Pell, I Korobkov and D. Richeson, Dalton Trans., 2017, 6518–6522.

(16) H. I. Karunadasa, C. J. Chang and J. R. Long, Nature, 2010, 464, 1329–1333.

(17) Y. Sun, J. P. Bigi, N. A. Piro, M. L. Tang, J. R. Long and C. J. Chang, J. Am. Chem. Soc., 2011, 133, 9212–9215.

(18) M. Frey, ChemBioChem 2002, 2002, 3, 153–160.

(19) W. Lubitz, H. Ogata, O. Ru and E. Reijerse, Chem. Rev., 2014, 114, 4081–4148.

(20) Z. Flisak and W.-H. Sun, ACS Catal., 2015, 5, 4713–4724.

(21) L. Chen, G. Chen, C. Leung, S. Yiu and C. Ko, ACS Catal., 2015, 5, 356–364.

(22) Z. Chen, T. Wang, T. Sun, Z. Chen, T. Sheng, Y. H. Hong, Z. A. Nan, J. Zhu, Z. Y. Zhou, H. Xia and S. G. Sun, Chinese J. Chem., 2018, 36, 1161–1164.

(23) E. C. Alyea and P. H. Merrell, Inorganica Chim. Acta, 1978, 28, 91–97.

(24) O. Luca, S. J. Konezny, E. K. Paulson, F. Habib, K. M. Luthy, M. Murugesu, R. H. Crabtree and V. S. Batista, Dalton Trans., 2013, 42, 8802.

(25) N. Elgrishi, K. J. Rountree, B. D. McCarthy, E. S. Rountree, T. T. Eisenhart and J. L. Dempsey, J. Chem. Educ., 2018, 95, 197–206.

(26) E. S. Rountree, B. D. McCarthy, T. T. Eisenhart and J. L. Dempsey, Inorg. Chem., 2014, 53, 9983–10002.

(27) A. M. Appel and M. L. Helm, ACS Catal., 2014, 4, 630–633.

(28) V. Fourmond, P.-A. Jacques, M. Fontecave and V. Artero, Inorg. Chem., 2010, 49, 10338–10347.

(29) D. H. Pool and D. L. Dubois, J. Organomet. Chem., 2009, 694, 2858–2865.

(30) U. J. Kilgore, J. A. S. Roberts, D. H. Pool, A. M. Appel, M. P. Stewart, M. R. Dubois, W. G. Dougherty, W. S. Kassel, R. M. Bullock and D. *J. Am. Chem. Soc.*, 2011, **133** , 5861 —5872

Chapter 4: Reduction of Nitrite with Earth Abundant Water Soluble Molecular Electrocatalysts

Overview

In this chapter, we explore the electrochemical reactivity of two earth abundant macrocyclic complexes. With inspiration from the redox-active diiminopyridine ligand backbone in chapter 3 and the water solubility of the complex, we decided to attempt to exploit these further. Our initial targets for investigating the reduction of nitrite are represented by 1 and 2a. *Calculations and associated figures were done by Joshua Brown and the initial synthesis of complex **2** was performed by Somayeh Norouziyanlakvan.

Introduction:

Due to the substantial increase in world population of the last few centuries, a need for more agricultural resources has skyrocketed. To feed the population's constant and growing need for food, the Haber-Bosch process was invented and industrialized for the primary use of synthesizing ammonia for use in fertilizers. However, because the Haber-Bosch process is producing such large amounts of ammonia, there has been a dramatic increase in man-made nitrogen content being introduced into the global nitrogen cycle. While the Haber-Bosch process is a necessity for the planet's growing population due to the significance of the ammonia produced for use in ammonia-based fertilizers, there have been detrimental side-effects on the planet's ecosystems due to the unnatural increase in nitrogen content in the nitrogen cycle.[1-4] Because of this, ecosystems can begin to experience eutrophication resulting in damage to aquatic life and bodies of water and potentially humans. As a potential remedy, scientists have begun conducting research into methods such as the electroreduction of nitrogen oxyananions

(NO_3^- and NO_2^-) to reduce the amount of manmade nitrogen content in the environment and to aid in understanding the nitrogen cycle and the transformations that occur within it.[5,24]

Recently, a number of nitrite-reducing transition metal catalysts particularly using Fe and Co metal centers have been reported.[6-11] With the importance of sustainably managing the concentration of waste water contaminants such as nitrite and nitrate, molecular catalysts are a promising route to explore. Specifically, exploring catalysts for the reduction of nitrite (NO_2^-) and the elucidation of its reaction mechanisms would bring valuable insight into the global nitrogen cycle.

Ligand Selection

A common characteristic of metal-centered complexes that participate in homogeneous nitrate and nitrite reduction reactions is the use of a redox-active moiety in the ligand design. Additionally, intramolecular proton shuttles, typically secondary amines which are bound to the metal, are incorporated into the ligand. Together, these two are speculated to reduce reaction barriers to allow for catalytic nitrite reduction to occur. [6,10] A recently published literature review of advancements in the field of electrocatalytic nitrite reduction listed a variety of different metal-ligand frameworks providing different product selectivity with no clear trend as to how it was achieved. However, rational catalyst design with characteristics such as electronic structure and conjugated pi-systems, spatial structures, etc. remains a key element in modifying reaction selectivity for homogeneous nitrogen oxyanion reduction catalysis.[5]

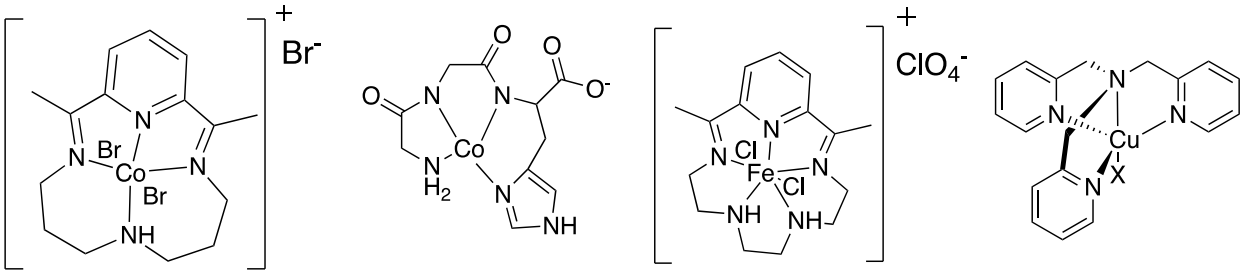

Scheme 1: Various reported homogeneous nitrite reducing electrocatalysts that incorporate an intramolecular proton shuttle and redox active moiety (excluding D which has only a redox-active moiety).[5]

When selecting a potential ligand to explore electrocatalytic nitrite reduction, several factors were considered such as synthetic difficulty, whether the resulting catalyst would be homogeneous or heterogeneous, and an associated target reaction product.

The work described in this chapter was inspired by our previous results for electrocatalysis from [Ni(κ^3-2,6-{PhNCMe}$_2$(NC_5H_3))Br_2], as described in Chapter 2, and the reported catalytic reduction ability of complexes **A** and **C.** These compounds share a similar 2,6-diimine pyridine backbone. This ligand family has a well-established history in homogeneous catalysis, and they can be synthetically accessed by a simple condensation reaction to form a variety of different structures. Furthermore, diiminopyridines (DIMPY) are non-innocent ligands that have been documented to be capable of acting as electron reservoirs due to their two characteristic highly delocalized and low-lying π^* orbitals which lead to bonding character similar to that of singlet biradical behaviour. This behaviour allows the DIMPY ligand to accept electrons from metal d-orbitals.[12-14] Additionally, the diiminopyridine ligand backbones have been demonstrated to produce catalysts that exhibit high product selectivity and high stability in a variety of catalytic transformations like hydrogenation and hydrosilylation reactions, HER, and polymerization reactions.[15-20] Finally, with respect to aqueous nitrite reduction, the diiminopyridine scaffold is attractive due to the fact that complexes of this ligand are documented to be soluble in water. Coordination of Ni(II) with the diiminopyridine ligand yields a square planar conformation which allows the metal ample access for coordination of the nitrite anion to the Ni center.[16,21,22]

Results & Discussion:

Synthesis and Structural Characterization of Complexes

By employing appropriate diamines in the condensation with 2,6-diacetylpyridine to generate Schiff base ligands, it is possible to prepare macrocyclic versions of the diiminopyridine ligands. In general, to promote the formation of the cycle, a metal center is used as a templating agent in this process. This general process is represented in Scheme 2. As anticipated, the metal templated reaction between Ni(II)Cl_2 and a stoichiometric amount of 2,6-diacetylpyridine and 3,3'-diamino-N-methyldipropylamine followed by anion exchange with perchlorate, resulted in a bright red violet precipitate of complex **1** (Scheme 3). Crystallization was achieved by layering diethyl ether on a solution of **1** dissolved in acetonitrile to yield bright red needle crystals.

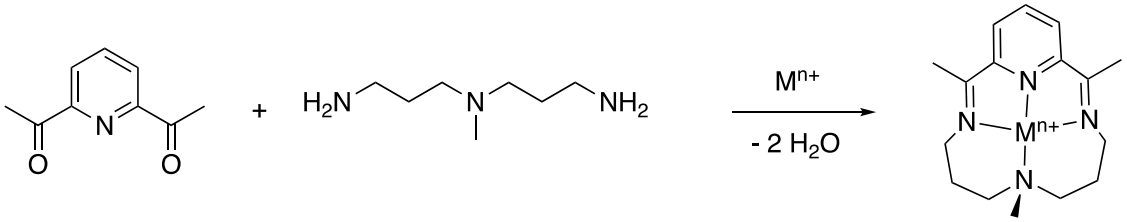

Scheme 2: Generic synthesis of a macrocyclic diiminopyridine ligand.

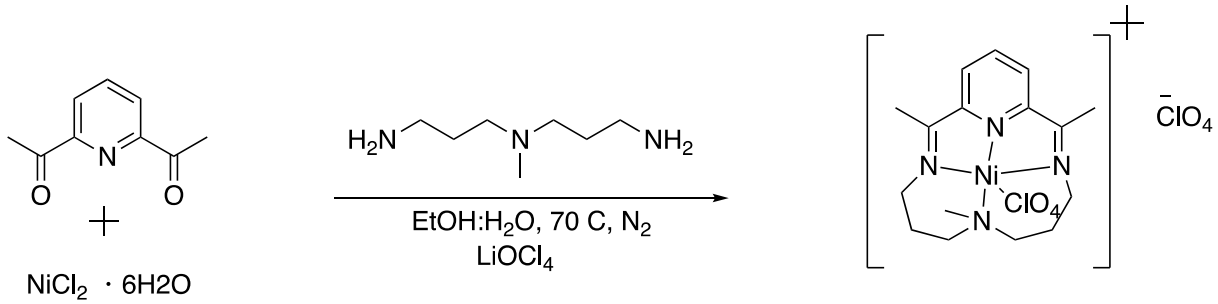

Scheme 3: Synthesis of Ni(II) (2,12-trimethyl-3,7,11,17-tetraazabicyclo [11.3.1]heptadeca-1(17),13,15-triene)$(ClO_4)_2$ **(1) (or NiDIMPYNME)**.

Figure 1 depicts the results of the X-ray structural analysis of complex **1** showing only the cationic metal complex portion of the structure. The perchlorate counterion is not shown. The Ni(II) complex consists of the expected tetradentate macrocyclic ligand that is coordinated

to the Ni center in a distorted square planar arrangement as seen in Table 1, the bond angles between O(6)-Ni(1)-N(1 through 4) add up close to 360 degrees. One perchlorate anion is coordinated to the Ni center perpendicular to the plane defined by the ligand. Interestingly, the bond between the Ni metal center and perchlorate anion has a length of 2.499 Å which is rather long. We speculate that the perchlorate is bound only in the solid state and dissociates immediately upon **1** dissolving in a solvent. This speculation is supported by DFT calculations (Figure 26) and will be discussed later.

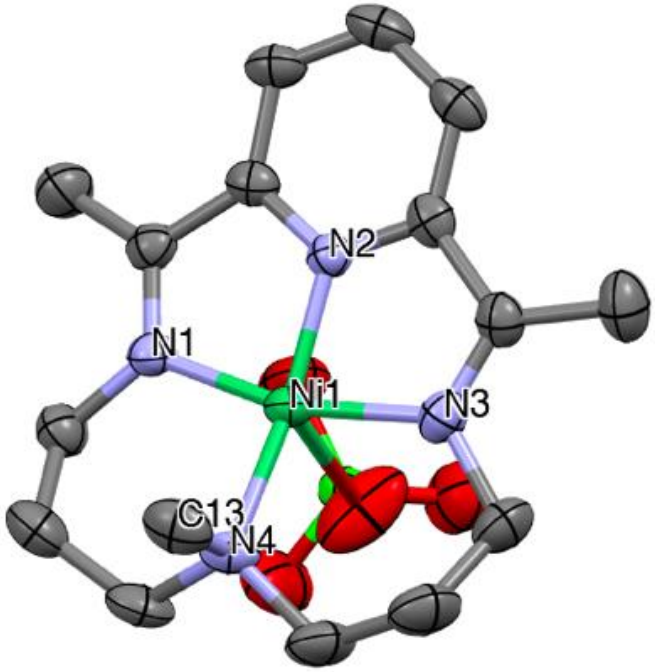

Figure 1: Structural representation for compound Ni(II) (2,12-trimethyl-3,7,11,17-tetraazabicyclo [11.3.1]heptadeca-1(17),13,15-triene)$(ClO_4)_2$ (**1**) obtained from single crystal X-ray analysis. Hydrogen atoms and the second perchlorate anion have been omitted for clarity.

Table 1: Comparison between SC-XRD experimental data and M06L optimized computed values for internuclear distances (Å) and bond angles (°).

Bond (Å)	**SC-XRD Experimental Bond Length (Å)**	**M06L Computed Bond Length (Å)**
Ni(1)-O(6)	2.499(4)	2.245
Ni(1)-N(1)	1.926(4)	1.941
Ni(1)-N(2)	1.830(4)	1.837
Ni(1)-N(3)	1.921(4)	1.941
Ni(1)-N(4)	1.947(4)	2.001
N(4)-C(13)	1.491(7)	1.474
Bond Angles (°)	**SC-XRD Experimental Bond Angles (°)**	**M06L Computed Bond Angles (°)**
O(6)-Ni(1)-N(1)	93.04	99.58
O(6)-Ni(1)-N(2)	106.07	112.58
O(6)-Ni(1)-N(3)	88.84	88.67
O(6)-Ni(1)-N(4)	88.69	87.36

A similar reaction was employed to target the Co(II) analogue of **1**. In this case the reaction between 2,6-diacetylpyridine and 3,3'-diamino-N-methyldipropylamine was carried out using $CoCl_2 6H_2O$ as the template species. The violet-coloured powder was crystallized by dissolving the product in a minimum amount of hot distilled water and left to cool and evaporate to leave deep red needles. (Scheme 4). This reaction has been previously reported in the literature and the authors reported that the result was a Co-methylene species that presumably arose from a CH deprotonation step. Unfortunately, the data reported by these authors was not complete and since this material was paramagnetic, we relied on single crystal X-ray analysis to determine the molecular structure of this reaction product.[23]

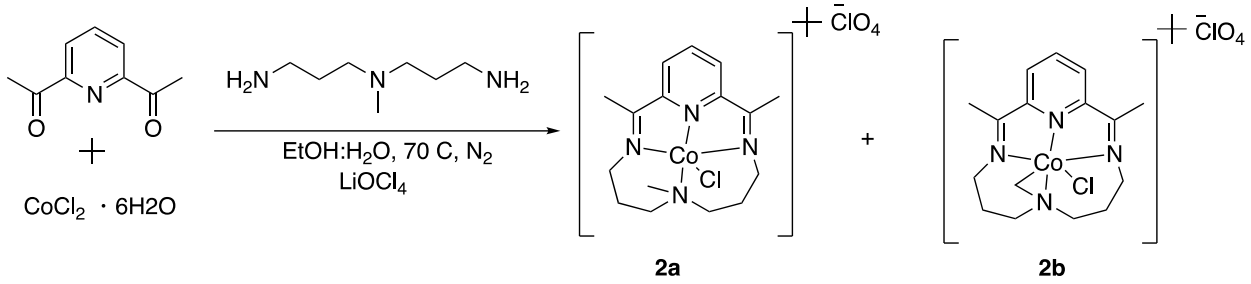

Scheme 4: Synthesis of **2a** & **2b (or CoDIMPYNMe)**.

The results of a single crystal X-ray analysis of this Co complex are displayed in Figures 2 and 3. In fact, the single crystal of this reaction product displayed two different Co structures, 2a being Co(II) and 2b Co(III). In both cases the Co complex is a cationic species with charge compensation from remote perchlorate counter anions. The first Co cationic complex, show in Figure 2, was the simple targeted macrocycle supported CoCl cation. Like complex **1**, the macrocyclic N_4 ligand was coordinated in a planar fashion to the Co(II) center. The coordination environment of the Co(II) is completed by a Cl^- ligand to give a distorted square pyramidal geometry which is supported by the SC-XRD experimental bond angles in Table 2 which add up close to 360° for the square plane of the bound N_4 ligand.

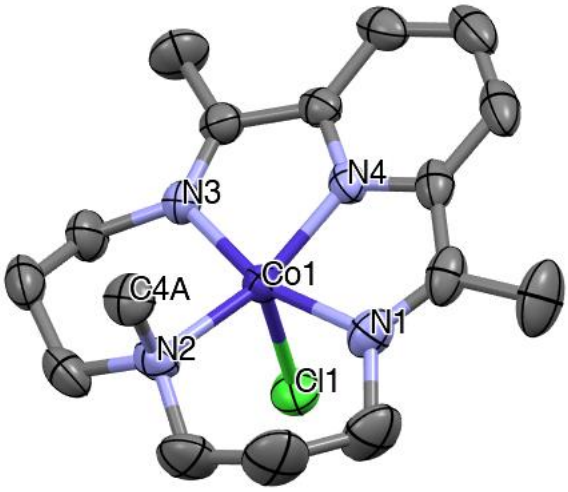

Figure 2. Structural representation for compound Co(II) (2,12-trimethyl-3,7,11,17-tetraazabicyclo [11.3.1]heptadeca-1(17),13,15-triene)(ClO_4)Cl (**2a**) obtained from single crystal X-ray analysis. Hydrogen atoms and the co-crystallized perchlorate anion have been omitted for clarity.

Table 2: Table of experimental SC-XRD values for internuclear distances (Å) and bond angles (°).

Bond (Å)	**SC-XRD Experimental Bond Lengths (Å)**
Co(1)-N(1)	1.938(2)
Co(1)-N(2)	1.966(2)
Co(1)-N(3)	1.934(2)
Co(1)-N(4)	1.834(2)
Co(1)-Cl(1)	2.358(6)
N(2)-C(4A)	1.511
Bond Angles (°)	**SC-XRD Experimental Bond Angles (°)**
Cl(1)-Co(1)-N(1)	92.36
Cl(1)-Co(1)-N(2)	98.58
Cl(1)-Co(1)-N(3)	91.43
Cl(1)-Co(1)-N(4)	103.35

The second Co complex, which was crystallized along with the first as a 50/50 mix, is shown in Figure 3. Unlike the first Co complex, the macrocyclic N_4 ligand is now coordinated with an additional methylene bridge such that N(2)-C(4A)-Co(1) makes a closed three-membered ring. Due to the addition of another anionic bonding entity, there is speculation that the oxidation state of the Co center has changed now from Co(II) to Co(III) and has a coordination environment like that of a distorted octahedron. However, further investigation into this matter yielded another potential result for this structure which would be an agostic interaction between a hydrogen atom

attached to C4A and the Co metal center. Comparing the bond distances between the M-C4A bonds for an agostic interaction and with a methylene bridge, one would expect them to be significantly different if one option is more favourable than the other. However, this was not the case as both M-C distances were similar at 1.968(7) Å for the potential structure with an agostic interaction, and 1.960(7) Å for the potential structure methylene bridge. Thus, currently we are uncertain on the structure and as to whether the Co metal center is Co(II) or Co(III).

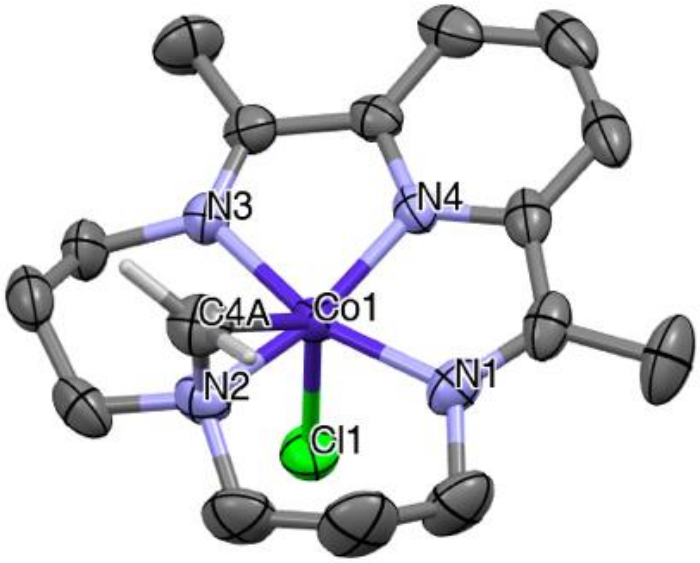

Figure 3. Structural representation for compound Chloro-2,12-dimethyl-3,7,11,17-tetra-azabicyclo[11.3.1]- heptadeca-1(17),2,11,13,15-pentaen-7-ylmethyl-cobalt(III)- perchlorate monohydrate (**2b**) obtained from single crystal X-ray analysis. Hydrogen atoms apart from those on C4A have been omitted for clarity. The unbound perchlorate anion has also been omitted for clarity.

Table 3: Table of experimental SC-XRD values for internuclear distances (Å) and bond angles (°).

Bond (Å)	**SC-XRD Experimental Bond Length (Å)**
Co(1)-N(1)	1.938(2)
Co(1)-N(2)	1.966(2)

Co(1)-N(3)	1.934(2)
Co(1)-N(4)	1.832(2)
Co(1)-Cl(1)	2.358(6)
Co(1)-C(4A)	1.960(7)
N(2)-C(4A)	1.402(6)
Bond Angles (°)	**SC-XRD Experimental Bond Length (°)**
Cl(1)-Co(1)-N(1)	92.36
Cl(1)-Co(1)-N(2)	98.58
Cl(1)-Co(1)-N(3)	91.43
Cl(1)-Co(1)-N(4)	103.35

Electrochemical Characterization & Electrocatalysis

With compounds 1 and 2a,b in hand, we set out to perform the electrochemical characterization and examine their potential as nitrite-reducing electrocatalysts. In acetonitrile, **1** displays two reversible reduction peaks at $E_{1/2}$ = -0.52 V and $E_{1/2}$ = -1.10 V (Figure 4). For both peaks the ΔE_p = 0.1 V. After initial characterization in CH_3CN, the electrochemistry of **1** was examined in aqueous media to test reactivity for NO_2^- reduction reactions.

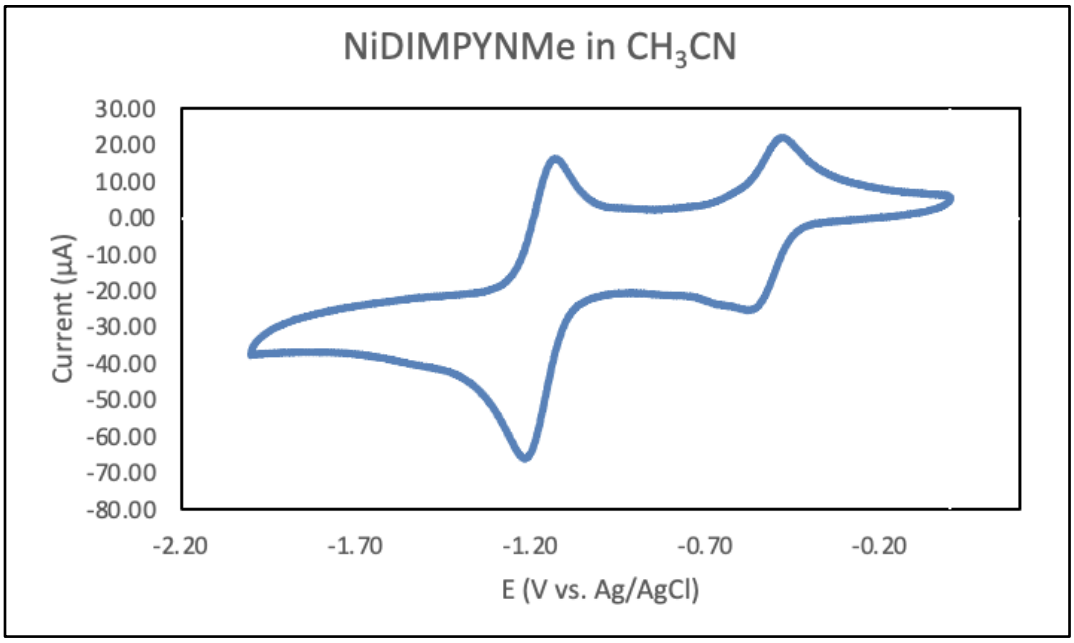

Figure 4: CV of **1** in CH_3CN under inert dinitrogen atmosphere with 0.1 M $TBAPF_6$ as the supporting electrolyte.

A similar set of CV experiments were performed on the complex mixture **2a,b**. Unfortunately, we have not separated the two co-crystallizing species and thus there are some limits on the electrochemical characterization. In any case, Figure 5 shows that under an inert dinitrogen atmosphere in acetonitrile, the **2a,b** mixture exhibited three reversible redox events at $E_{1/2}$ = -0.4 V, -1.0 V, and -1.52 V vs. Ag/AgCl.

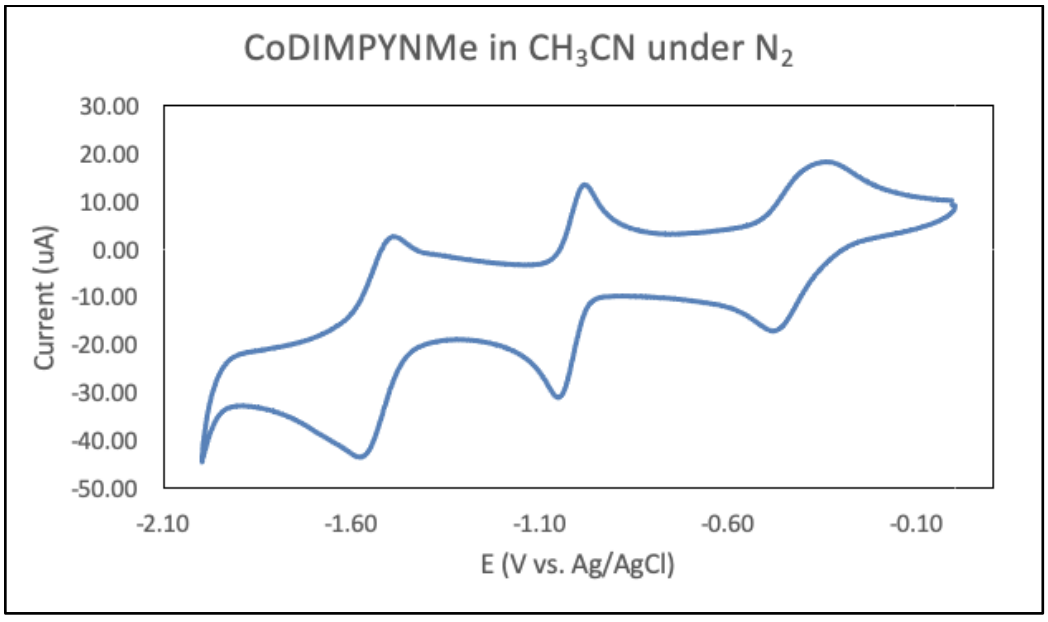

Figure 5. CV of **2a,b** in CH_3CN under inert dinitrogen atmosphere with 0.1 M $TBAPF_6$ as the supporting electrolyte.

Our goal was to examine the catalysis capabilities of these complexes for reduction of aqueous nitrite solutions. A key consideration before beginning this effort is to realize that the reduction reaction involves a proton-coupled step and, therefore, for a successful catalytic reaction the control of the reaction solution pH will likely be important. Specifically, a buffer derived from 4-morpholinepropanesulfonic acid (MOPS buffer) was chosen as a non-coordinating buffer and to target a pH of 7 (pKa = 7.02). The CV for **1** in water/MOPS (pH 7) is displayed in Figure 6. As indicated by the CV, complex **1** exhibites two irreversible reduction events at E = -0.89 V and -1.00 V.

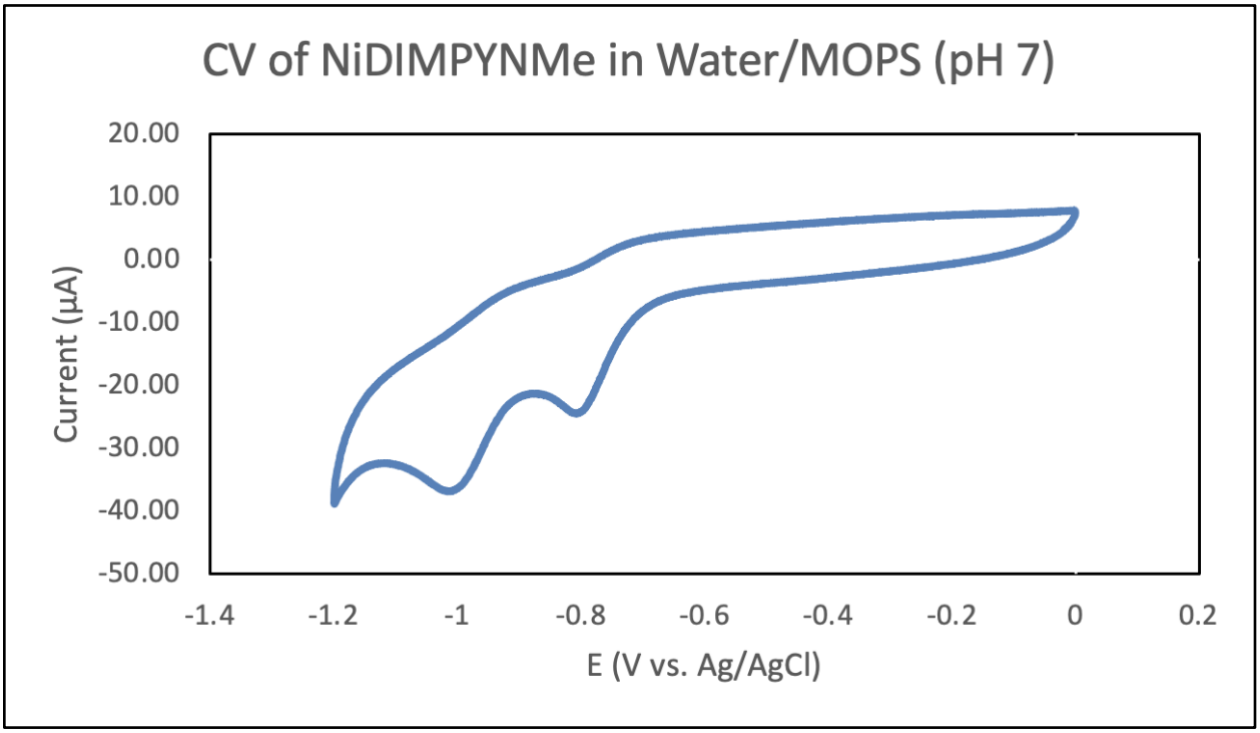

Figure 6: CV of **1** in water/MOPS (pH 7) under inert dinitrogen atmosphere with 0.1 M KCl as the supporting electrolyte.

The stability and homogeneity of these reductions was assessed by measuring the scan rate dependence of the current for the first and second reduction peaks (Figures 7 and 8) for complex **1** in water with 50 mM MOPS buffer. The results of these measurements are shown in Figures 7-

10. The linear relationship obtained for the square root of the scan-rate vs. peak current is consistent with the Randles-Ševčík equation and supports a diffusion-controlled process.[16]

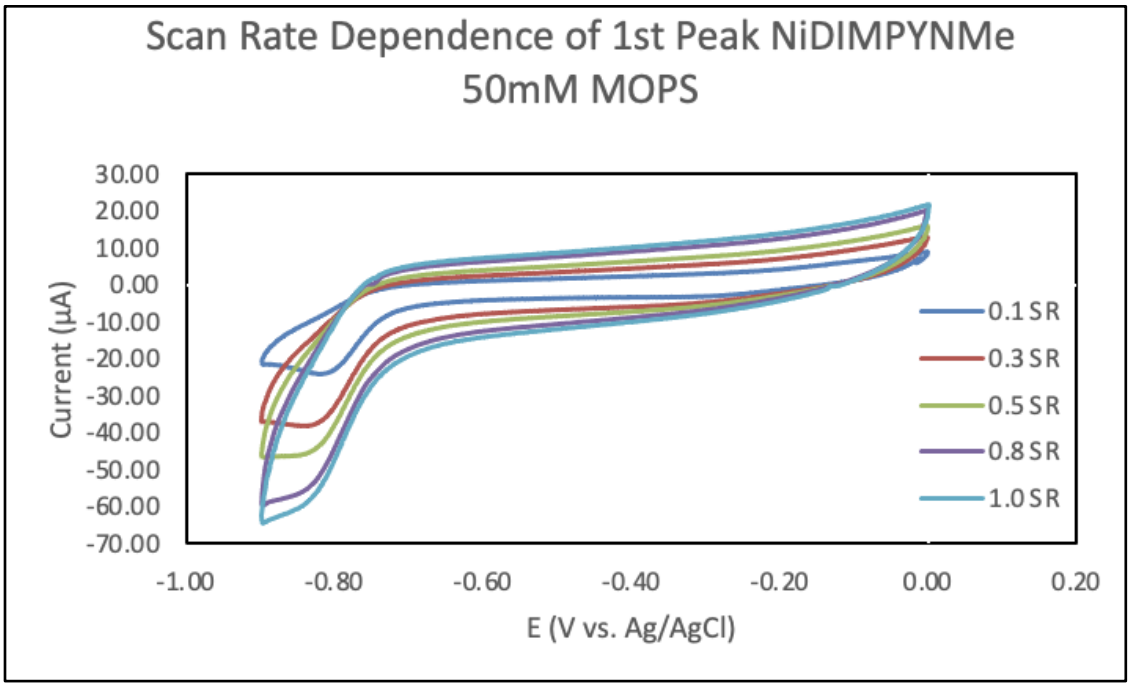

Figure 7: Scan rate dependence of the first reduction peak for complex **1** in water under inert dinitrogen atmosphere with 0.1 M KCl as the supporting electrolyte.

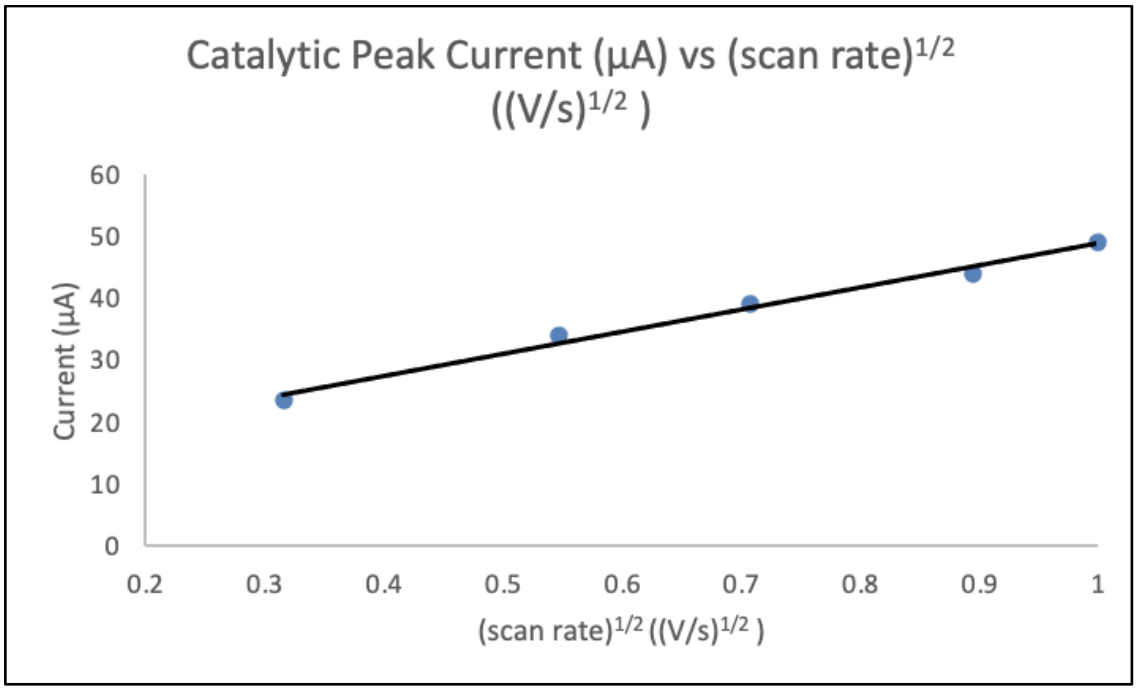

Figure 8: Plot of the square root of the scan rate $(V/s)^{1/2}$ of the first reduction peak for complex **1** vs. the peak current.

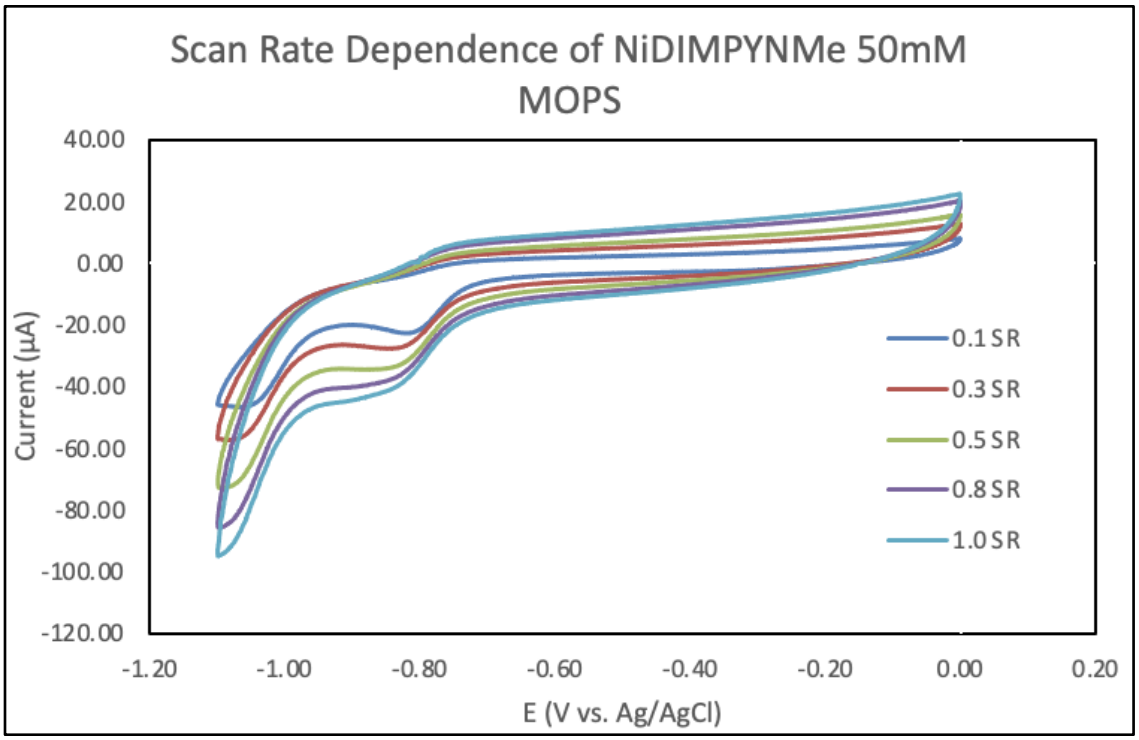

Figure 9: Scan rate dependence of the second reduction peak for complex **1** in water under inert dinitrogen atmosphere with 0.1 M KCl as the supporting electrolyte.

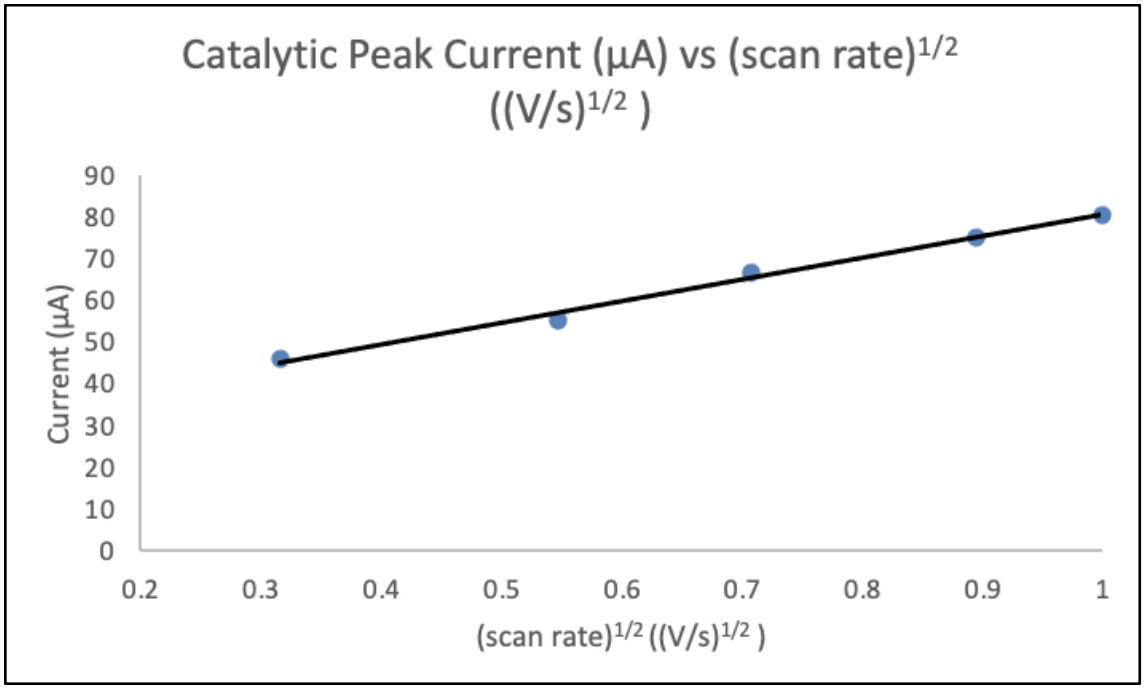

Figure 10: Plot of the square root of the scan rate $(V/s)^{1/2}$ of the second reduction peak for complex **1** vs. the peak current.

With these features established, the effect of incremental addition of $NaNO_2$ to a reaction cell containing 100 mM MOPS buffer and **1** was investigated. From Figure 11, after the initial addition of $NaNO_2$ into the system, there is a significant current enhancement at the second reduction event indicative of a catalytic process taking place.

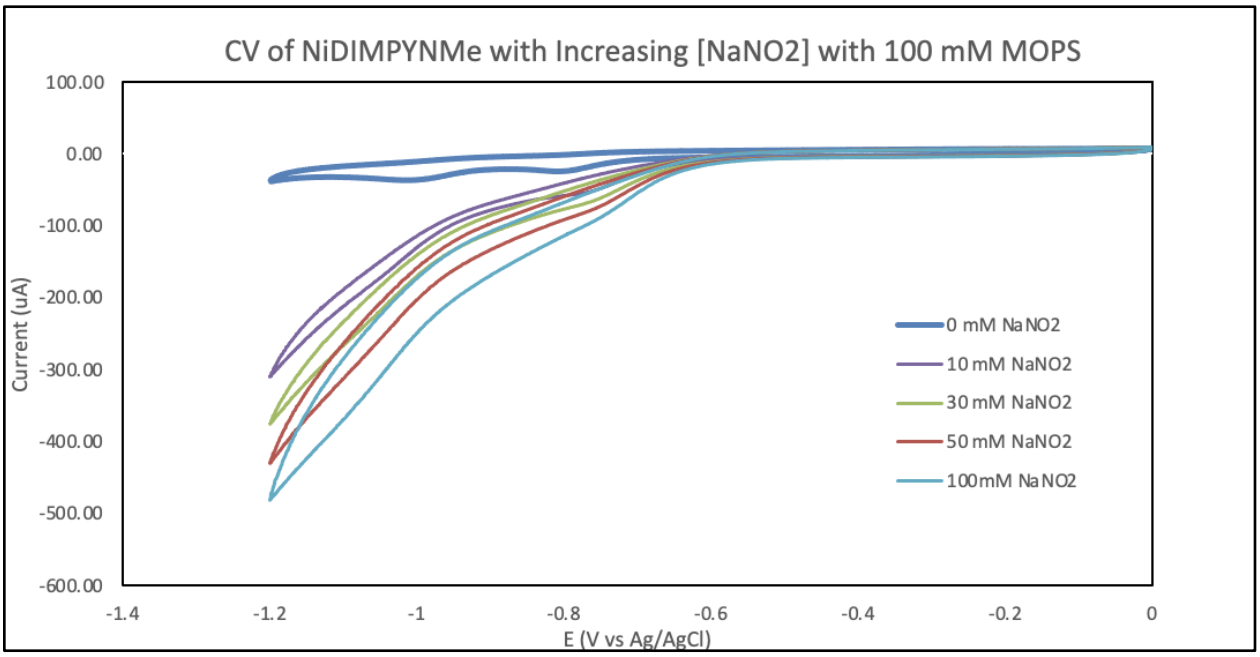

Figure 11: CV of **1** in water under inert dinitrogen atmosphere with 0.1 M KCl as the supporting electrolyte with increasing [$NaNO_2$] in a 100 mM MOPS buffered solution at pH 7.

Continued additions beyond 100 mM $NaNO_2$ to the reaction system resulted in only small current increases (Figure 12).Further addition of $NaNO_2$ led to a decline in current back to levels like that when 600 mM was added, it is expected at some point that saturation will be reached and there will no longer be current enhancement. With this observation it is clear that complex **1** is capable of electrocatalytically reducing nitrite; however there is a limit to its performance as a catalyst.

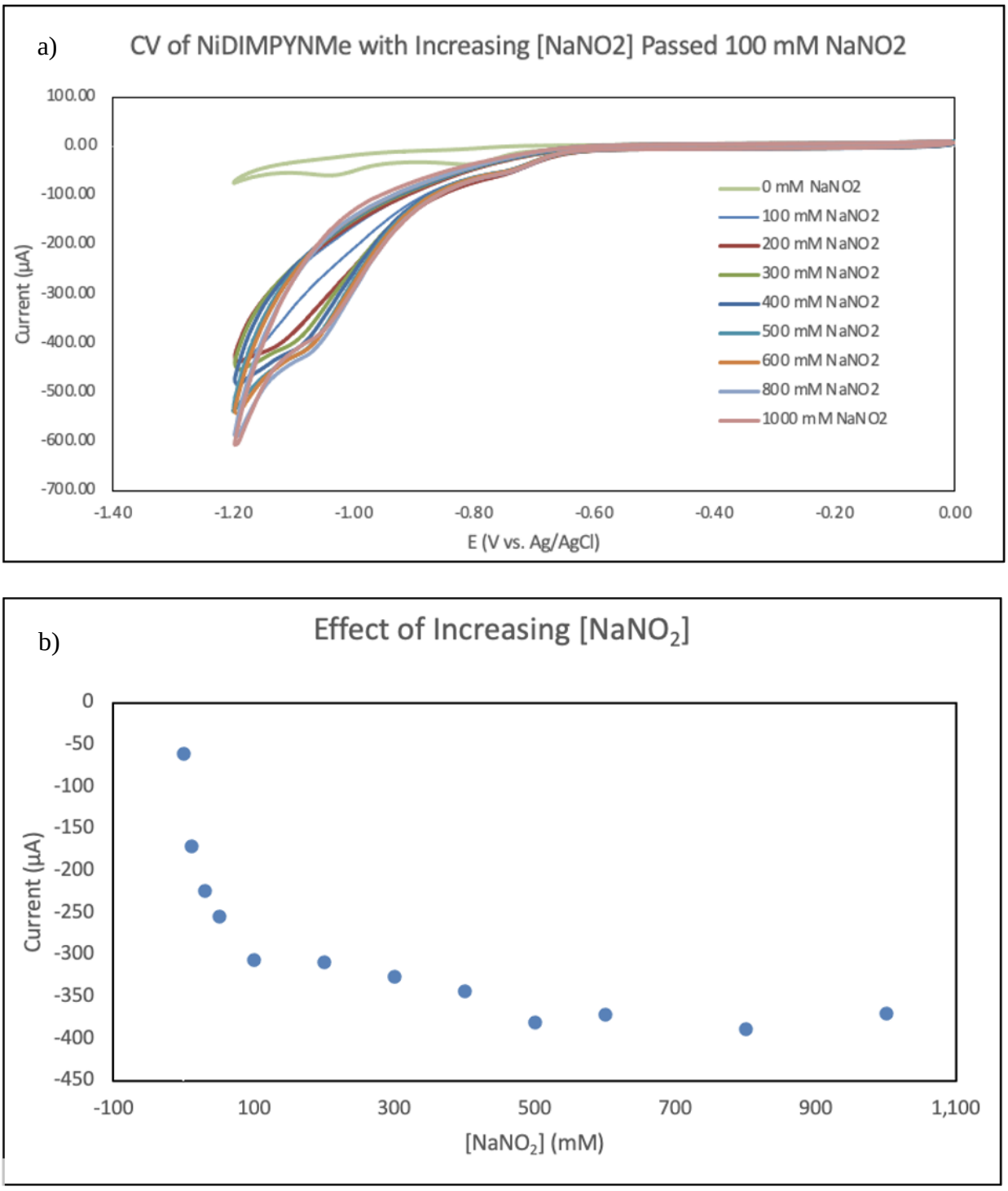

Figure 12: a) CV of **1** in water under inert dinitrogen atmosphere with 0.1 M KCl as the supporting electrolyte with increasing [$NaNO_2$] in a 100 mM MOPS buffered solution. b) Plot of the effect of how increasing the concentration of $NaNO_2$ affects current enhancement for **1**. Data values of current were taken at points corresponding to -1.05 V.

Scan rate dependence measurements were run on complex **1** under catalytic conditions consisting of 100 mM MOPS buffer and 10 mM $NaNO_2$ (Figure 13). The plot of the square root of the scan-rate vs. peak current (Figure 14) displayed a linear relationship, which is consistent with a diffusion-controlled process.[16]

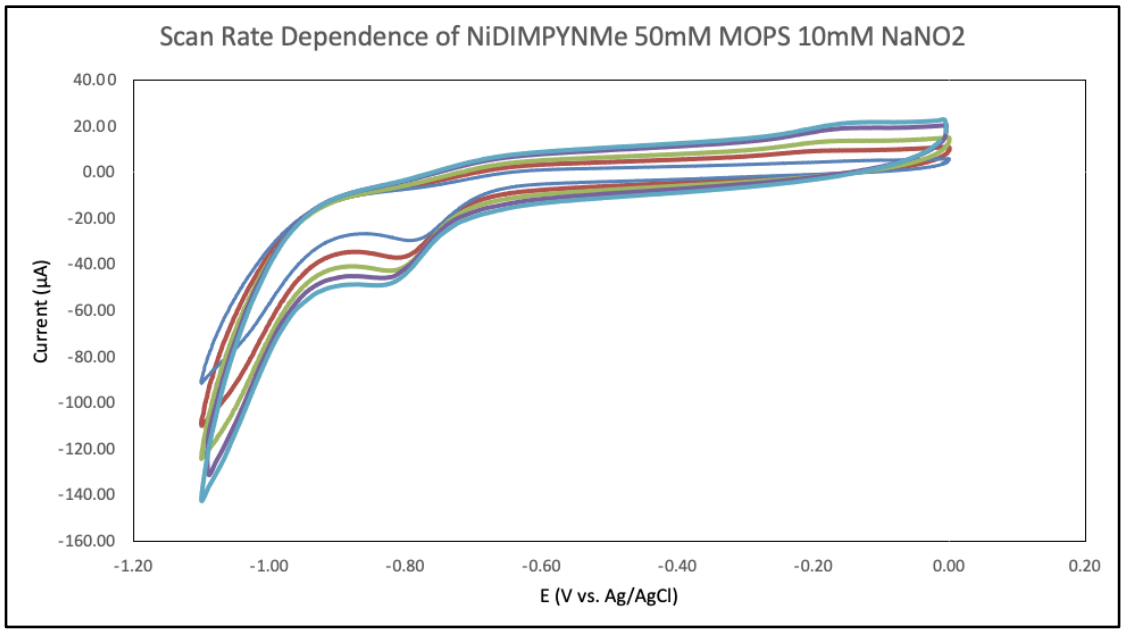

Figure 13: Scan rate dependence of the second reduction peak in a catalytic environment for complex **1** in water under inert dinitrogen atmosphere with 0.1 M KCl as the supporting electrolyte.

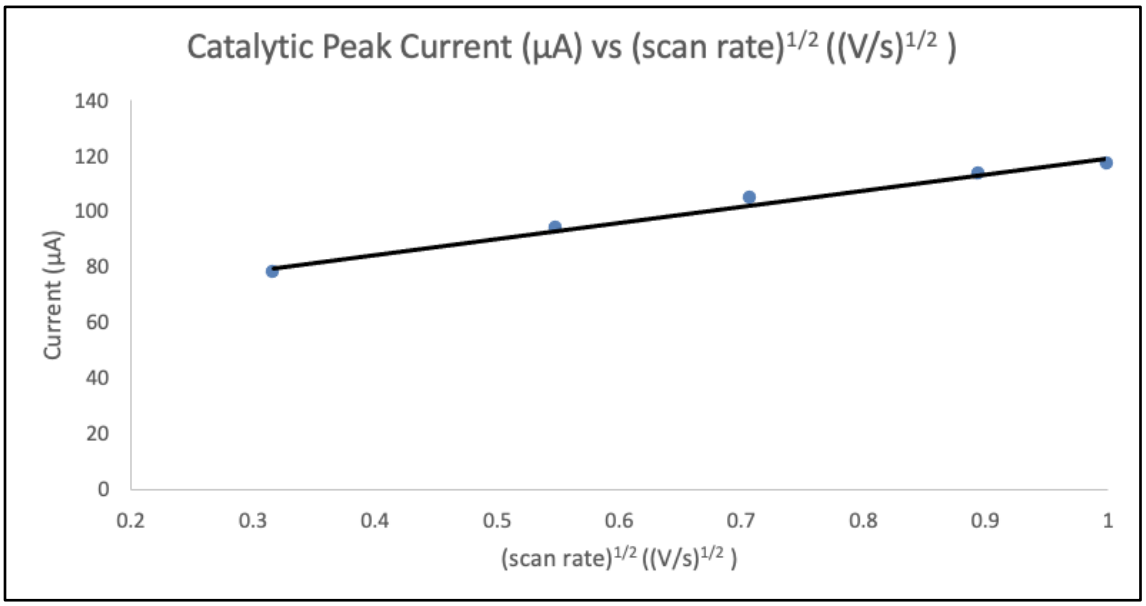

Figure 14: Plot of the square root of the scan rate $(V/s)^{1/2}$ of the second reduction peak in a catalytic environment for complex **1** vs. the peak current.

Further assessment of the reaction conditions was carried out through several control experiments, which were used to demonstrate the requirement of catalyst **1**, MOPS buffer, and substrate (sodium nitrite) in the reaction system. A cyclic voltammogram for a catalyst-free system of 100 mM MOPS and 100 mM $NaNO_2$ is shown in Figure 15. This figure documents that reduction at the GC electrode of this mixture appears at applied voltages exceeding -1.2V *vs* Ag/AgCl.

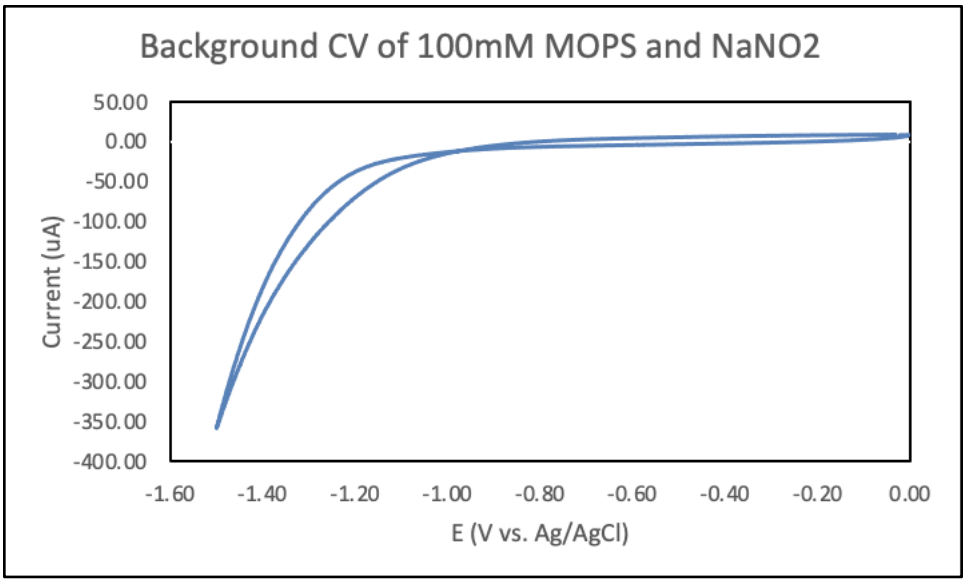

Figure 15: CV of in the absence of **1** in water under inert dinitrogen atmosphere with 0.1 M KCl as the supporting electrolyte with 100 mM MOPS and 100 mM $NaNO_2$.

Figure 16 shows the effect of incremental additions of MOPS buffer in an aqueous solution of **1** in the absence of nitrite. This data confirms that there is no enhancement in the reduction current for compound **1** due to the presence of MOPS buffer and supports a mostly innocent role for MOPS buffer in the reduction of **1**. However, the addition of MOPS does appear to initiate an anodic shift for both reduction peaks, thus enhancing the nitrite reduction kinetics by lowering the potential required for electron transport. This makes sense, since there is a direct relationship between pH and reduction potential. As pH increases (more basic and less

H^+ atoms available), the reduction potential shifts more positive. The requirement of MOPS for catalytic reduction of nitrite by **1** is shown by the data in Figure 17. These experiments demonstrated that there was very little current enhancement in the reduction when MOPS buffer is absent indicative of no catalytic activity.

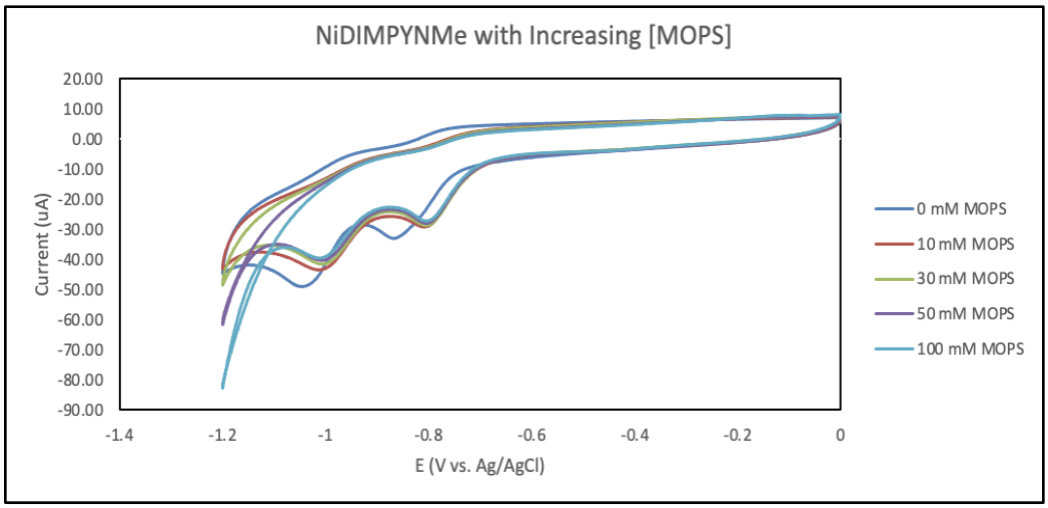

Figure 16: CV of **1** in water under inert dinitrogen atmosphere with 0.1 M KCl as the supporting electrolyte with increasing [MOPS] in the absence of $NaNO_2$.

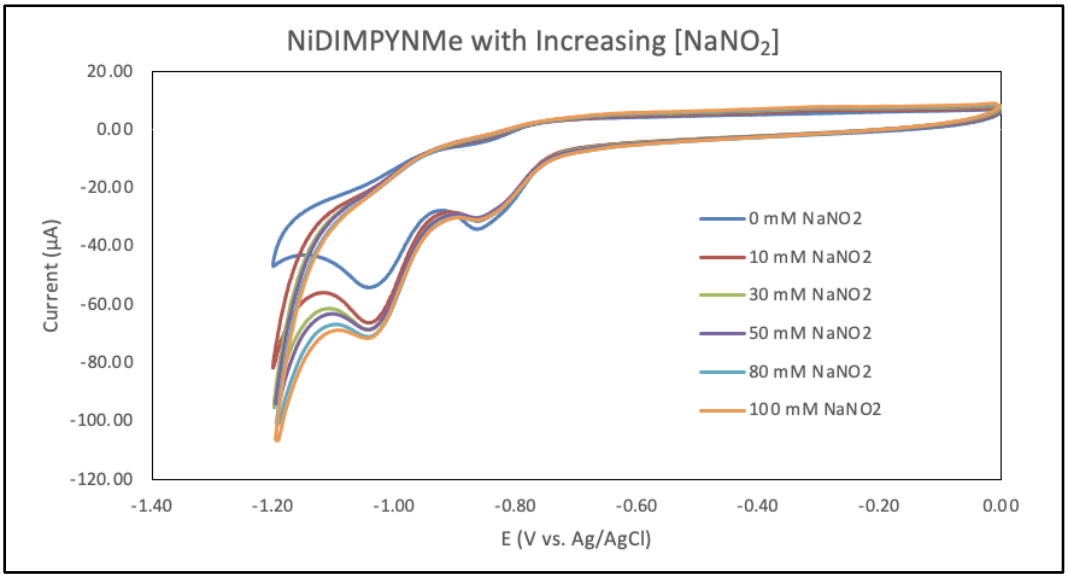

Figure 17: CV of **1** in water under inert dinitrogen atmosphere with 0.1 M KCl as the supporting electrolyte with increasing [$NaNO_2$] in the absence of MOPS.

The resulting CV for **2a,b** in water is displayed in Figure 18. As indicated by the CV, complex **2a,b** exhibits one reversible reduction event at E = -0.70 V and one irreversible reduction event at $E_{1/2}$ = -1.05 V. The stability and homogeneity of these reductions was assessed by measuring the scan rate dependence of the current for the first and second reduction peaks (Figures 20 and 21) for complex **2a,b** in water with 50 mM MOPS buffer. The results of these measurements are shown in Figures 19-21. The linear relationship obtained for the square root of the scan-rate vs. peak current is consistent with the Randles-Ševčík equation and supports diffusion-controlled processes.[16]

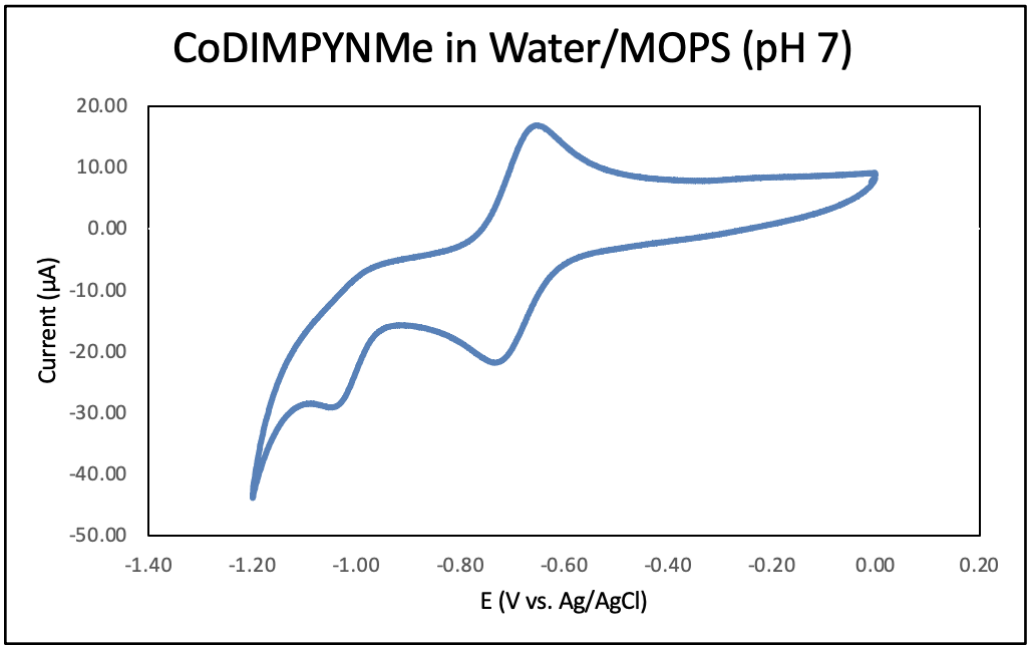

Figure 18: CV of **2a,b** in water under inert dinitrogen atmosphere with 0.1 M KCl as the supporting electrolyte.

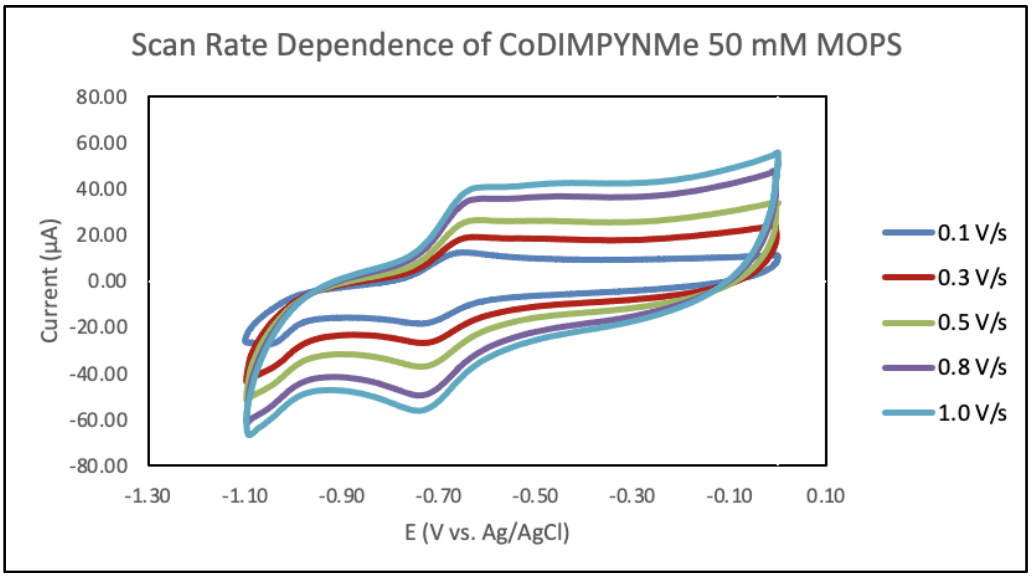

Figure 19: Scan rate dependence of the second reduction peak for complex **2a,b** in water under inert dinitrogen atmosphere with 0.1 M KCl as the supporting electrolyte.

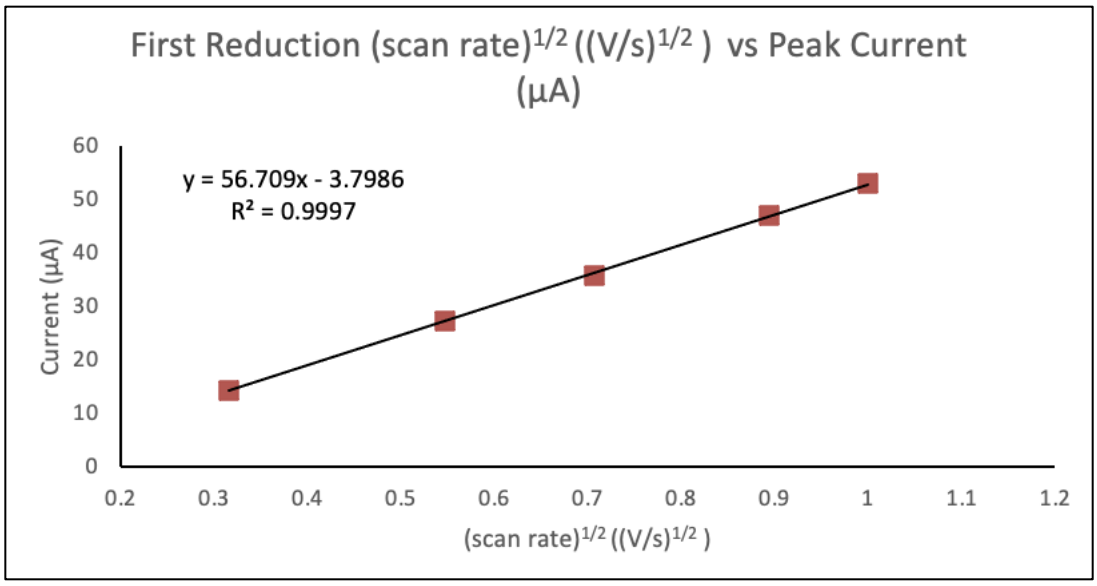

Figure 20: Plot of the square root of the scan rate $(V/s)^{1/2}$ of the first reduction peak in a catalytic environment for complex **2a,b** vs. the peak current.

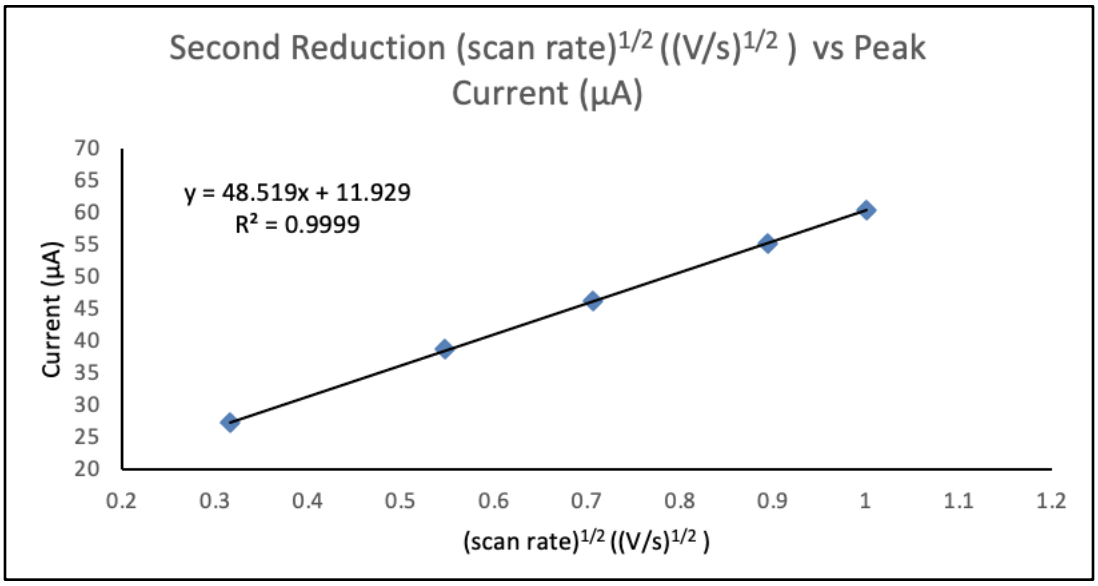

Figure 21: Plot of the square root of the scan rate $(V/s)^{1/2}$ of the second reduction peak in a catalytic environment for complex **2a,b** vs. the peak current.

After initial characterization, we next examined the effect of adding small increments of $NaNO_2$ to a reaction cell containing 100 mM MOPS buffer and **2a,b**. From Figure 22, there is a drastic increase in current as more $NaNO_2$ is added to the system. An excess of $NaNO_2$ 3:1 ratio of [$NaNO_2$] to [MOPS] was added and still exhibited enhancement in current, leading to the suggestion that the saturation point was not yet reached, and the catalyst can handle large equivalents of nitrite in the system.

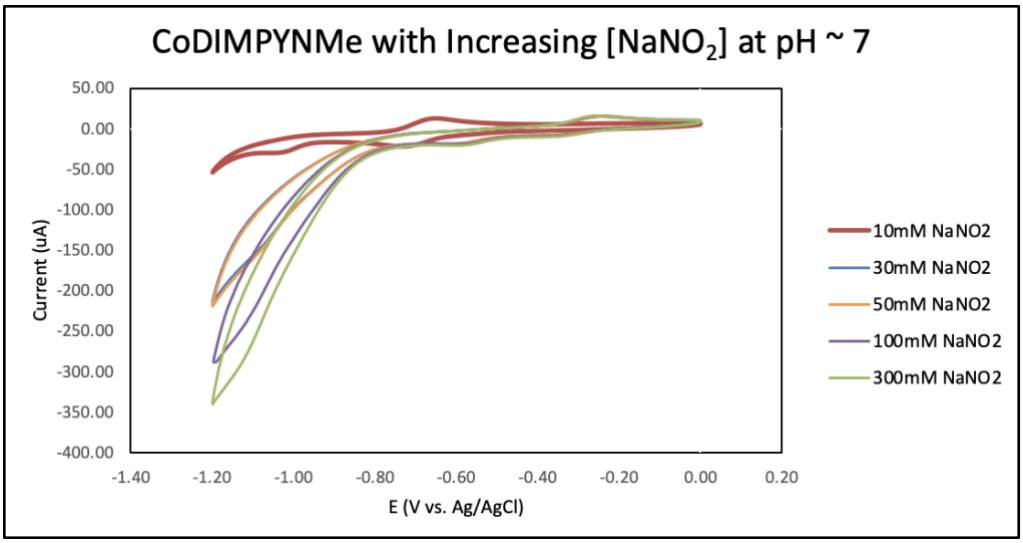

Figure 22: CV of **2a,b** in water under inert dinitrogen atmosphere with 0.1 M KCl as the supporting electrolyte with increasing [$NaNO_2$] in a 100 mM MOPS buffered solution at pH 7.

The preceding electrochemical characterization experiments of both **1** and **2a,b** demonstrated significant current enhancement in the presence of NO_2^- and MOPS buffer near pH 7 thus suggesting electrocatalytic reduction. With these clear signs of electrocatalytic behaviour, we were compelled to establish some more definitive answers on the product identities, selectivity, as well as activity and efficiency. To do so, we employed controlled potential coulometry (CPC) where a constant potential is applied to the reaction system for an extended period followed by analysis of the reaction products. The nitrogen cycle contains multiple transformations which can lead to several types of end products. In the gas phase, products such as NO, N_2O, and N_2 can be formed and in solution, products such as ammonia/ammonium (NH_3/NH_4^+) and hydroxylamine (NH_2OH) can be formed. The presence of gaseous products was analyzed using a GC/MSD to accurately discern the presence of NO, N_2O, and N_2. To determine whether N_2 was produced, a CPC experiment was done using inert argon gas in place of N_2. After analysis, it was concluded that no gaseous products formed. The presence of ammonium was analyzed using ^{14}N NMR and hydroxylamine by redox titration with [$K_3Fe(CN)_6$]. The results of these CPE experiments for the Ni complex **1** can be found in Table 4.

Table 4: Bulk results for reduction of nitrite using **1** at -1.05V vs. 3.0M KCl Ag/AgCl) with varying catalyst concentrations and times.[b] was done under inert argon gas, [c] was done at -0.98 V (vs. Ag/AgCl). Reactions unless otherwise noted contain 1.0 M MOPS buffer adjusted to pH 7.0, 1.0 M $NaNO_2$ and 0.1 M KCl as the supporting electrolyte.

Entry	[cat] (mM)	Time (hr)	µmol NH_4^+	FE NH_4^+ (%)	µmol NH_2OH	FE NH_2OH (%)	TON for NH_4^+	TON for NH_2OH
1	0.5	5	349	64	52	6.4	46.6	7
2	0.5	1	0	0	18	18	-	2.4
3	1	5	254	55	90	12	18.3	6

4	1	1	trace	0	8	8	-	0.5
5	2	5	266	57	17	2.4	8.9	0.5
7	1	18	1681	76	12	0.4	112	0.8
8[b]	1	5	314	69	90	12	20	6
9[c]	1	5	179	64	15	3.5	12	1
BKGRD	0	5	0	0	9	-	-	-
No Buffer	1	5	0	0	0	-	-	-

In the case of complex **1**, reactions were carried out for 1 or 5 hours at -1.05 V (s. Ag/AgCl in 15 mL solutions sparged with inert N_2 gas for 15 minutes. One CPC experiment (exp 9) was performed at a slightly lower potential of -0.98V to evaluate the effect of lower applied potential. Comparison between experiments 3 and 9 show a positive relationship between applied potential and formation of the reaction products. In general, an increased amount of both NH_4^+ and NH_2OH was observed when the applied potential was -1.05 V as opposed to -0.98 V. Notably, it appears that there was less selectivity for NH_4^+ in experiments at the more negative potential than with an applied potential of -0.98 V. Experiments 1, 3 and 5 were run to demonstrate the correlation between catalyst concentration and efficiency. The results indicate a lower catalyst concentration leads to a significant increase in TON, whereas a higher catalyst concentration leads to a decrease in TON indicating that an increase in catalyst concentration gave no additional product formation. To test the robustness of **1**, the conditions for experiment 5 were also run for 18 hours. To our surprise, 1681 µmol of NH_4^+ was produced with a TON of 112, a substantial increase in product formation and demonstration of the catalyst's capability of performing over long time periods. Understandably, the yield of NH_2OH is significantly lower since it is proposed that NH_2OH is one of the reaction intermediates between NO_2^- reduction to

NH_4^+ and so extended reaction times would naturally lead to an increase in selectivity and formation of NH_4^+.

During coulometry experiments the current is measured against time and this data is shown in Figure 23. A steady linear increase in the charge suggests a stable current flow meaning there is still substrate in solution available to be reduced. Surprisingly, increasing catalyst concentration displayed a slower electron transfer rate. This also correlates to the lower amount of product formation when 2 mM of **1** is used for experiments which can be seen in Table 4. Intuitively, it would be expected that by increasing [cat], more collisions between the substrate and the catalyst would occur; however this is not the case. This abnormality is currently under investigation.

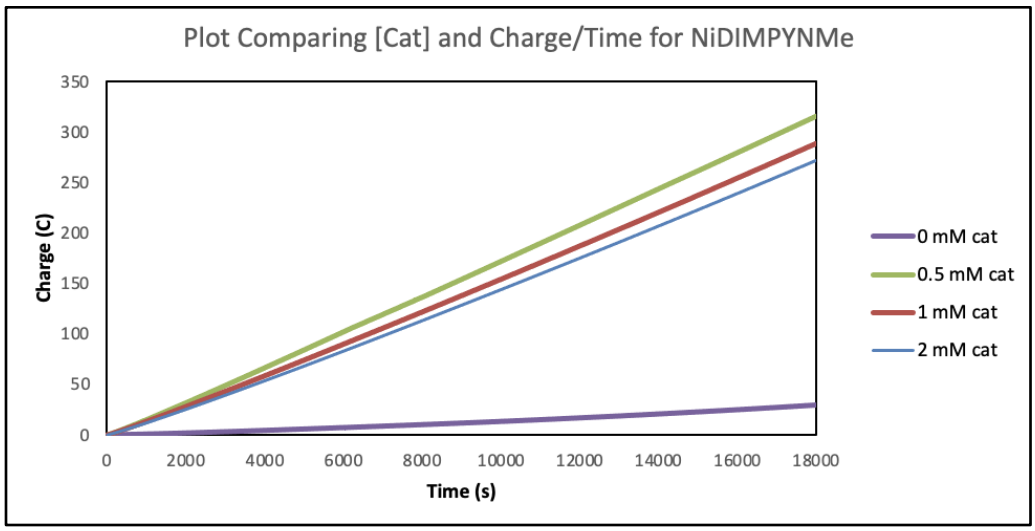

Figure 23: Plot comparing the concentration of **1** to the charge (C) produced over a 5 hour CPE experiment.

A similar set of CPC experiments was run for complex **2a,b** for which identical reaction conditions were used. The data is presented in Table 5.

Table 5: Bulk results for **2a,b** at -1.05V (V vs. 3.0M KCl Ag/AgCl) with varying catalyst concentrations and times. Reactions unless otherwise noted contain 1.0 M MOPS buffer adjusted to pH 7.0, 1.0 M $NaNO_2$ and 0.1 M KCl as the supporting electrolyte.

Entry	[cat] (mM)	Time (hr)	µmol NH_4^+	FE NH_4^+ (%)	µmol NH_2OH	FE NH_2OH (%)	TON for NH_4^+	TON for NH_2OH
10	0.5	5	206	68	54	11	27	7
11	0.5	1	0	0	36	49	-	2
12	1	5	219	67	108	22	14	7
13	1	1	0	0	27	56	-	3
14	2	5	99	76	27	13	3	3

When investigating the effect of catalyst concentration on efficiency, we found that with a 0.5 mM concentration of **2a,b** there was an increase in TON on the opposite side of the spectrum, an increase in catalyst concentration at 2 mM led to a significant decrease in TON (see Table 5). The amount of charge produced when 2 mM of catalyst is used is also significantly lower which further supports the claim that the catalyst is not as efficient with a higher concentration which results in lower product formation and TON.

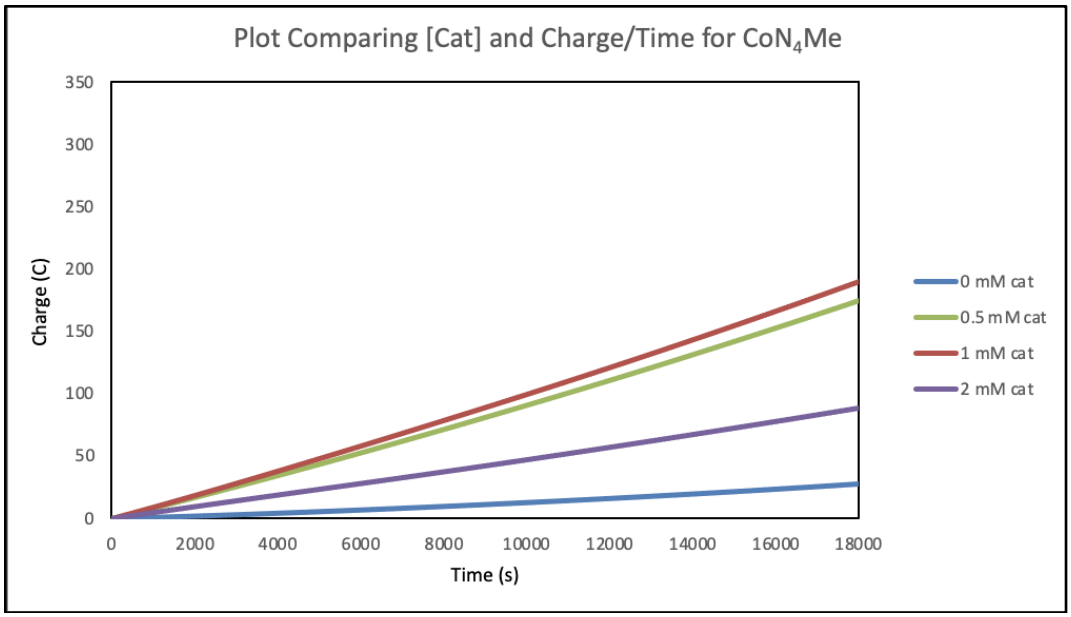

Figure 24: Plot comparing the concentration of **2a,b** to the charge (C) produced over a 5 hour CPE experiment.

Background CPC measurements were conducted in the absence of catalyst to ensure no product formation occurred due to the GCE and then in the absence of MOPS buffer to further solidify the argument that a buffered solution is a necessity for this reaction to occur. The investigation into this matter yielded positive results as no NH_4^+ nor NH_2OH was detected for both CPC measurements (Table 4).

Unfortunately, no experiments come without complications. During product identification, we found an unknown ^{14}N NMR peak at -2.8 ppm (see Figure 29). After performing multiple background identification experiments, we found that the peak at -2.8 ppm is due to the nitrate (NO_3^-) anion. The cause of this oxidation product occurring during a reduction reaction is still being investigated; however we speculate that the platinum electrode is oxidizing the nitrite (NO_2^-) anion during CPE experiments. For this reason, we also believe this may be a cause for lower Faradaic efficiency since the oxidized nitrite (now nitrate) may be getting reduced either at the electrode or by the catalyst which would affect the overall count of electrons and charge being contributed to the reactions. Another consideration when it comes to the low Faradaic efficiency of this reaction may be the $[K_3Fe(CN)_6]$ solution used to titrate the reaction mixture. This may have contributed to the low yield of NH_2OH because the $[K_3Fe(CN)_6]$ titrant solution was never made fresh, and the same batch was used throughout the course of the project. Although the literature does not say the solution must be prepared fresh nor does it degrade over time, the solution became discolored after a long period on the shelf.

To aid in the study of the nitrite reduction mechanism, we crystallized complex **1** with nitrite attached from a reaction mixture with typical catalytic conditions. A characteristic of the nitrite anion is its ability to coordinate via its N- (nitro) or O- (nitrito) atoms. N-vs O-coordination may influence nitrite reactivity. In the case of **1**, nitrite was found to bind through

the two oxygen atoms (Figure 25). An immediate downward bend in the non-conjugated portion of the ligand occurs when NO_2^- coordinates to the metal center likely due to steric repulsion which leads to the formation of an extremely distorted octahedral geometry.

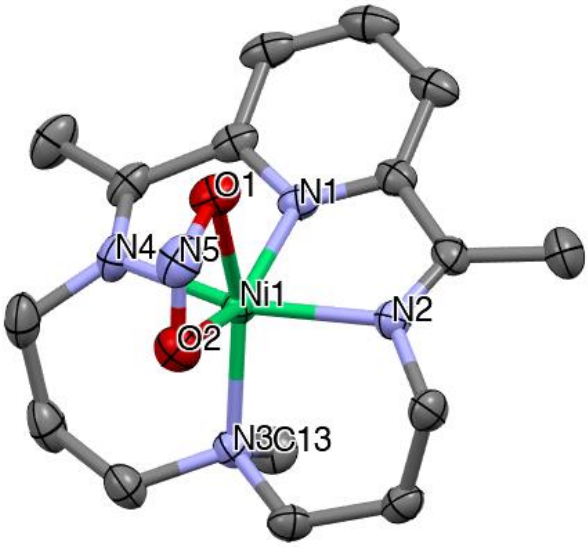

Figure 25: Structural representation for compound **1** with nitrite bound (**1-NO_2**) obtained from single crystal X-ray analysis. Hydrogen atoms and co-crystallized solvent have been omitted for clarity.

Table 6: Comparison between SC-XRD experimental data and M06L optimized computed values for internuclear distances (Å) and bond angles (°).

Bond (Å)	**SC-XRD Experimental Bond Length (Å)**	**M06L Computed Bond Length (Å)**
Ni(1)-O(1)	2.175(3)	2.810
Ni(1)-O(2)	2.087(2)	2.029
Ni(1)-N(1)	1.984(2)	1.825
Ni(1)-N(2)	2.081(2)	1.900
Ni(1)-N(3)	2.067(2)	2.132
Ni(1)-N(4)	2.072(2)	1.898
N(3)-C(13)	1.485(4)	1.467
Bond Angles (°)	**SC-XRD Experimental Bond Angles (°)**	**M06L Computed Bond Angles (°)**

O(1)-Ni(1)-N(1)	92.71	93.71
O(1)-Ni(1)-N(2)	94.22	79.94
O(1)-Ni(1)-N(3)	153.78	132.16
O(1)-Ni(1)-N(4)	93.49	101.34

Computational Analysis & Proposed Mechanism for NO_2^- Reduction

To better understand the products of the observed redox events and elucidate the nitrite reduction reaction mechanism, density functional theory (DFT) calculations were performed on the nickel complex in water using the polarizable continuum model (PCM) at the M06L level of theory.[25] Geometry optimization and vibrational frequency calculations were performed using def2-SVP as a basis set, followed by molecular energy computations with def2-TZVP. [26] Atomic coordinates were obtained from the crystal structure of **1**, initially with a perchlorate bound in the apical position (Figure 26). Relative Gibbs free energy calculations suggest that the perchlorate ligand is labile, indicating an exergonic process for the ligand leaving of -2.92 kcal/mol. Eliminating the perchlorate ligand from the structure removes the antibonding character that perchlorate contributes to the highest occupied molecular orbital (HOMO), ultimately stabilizing the electron configuration.

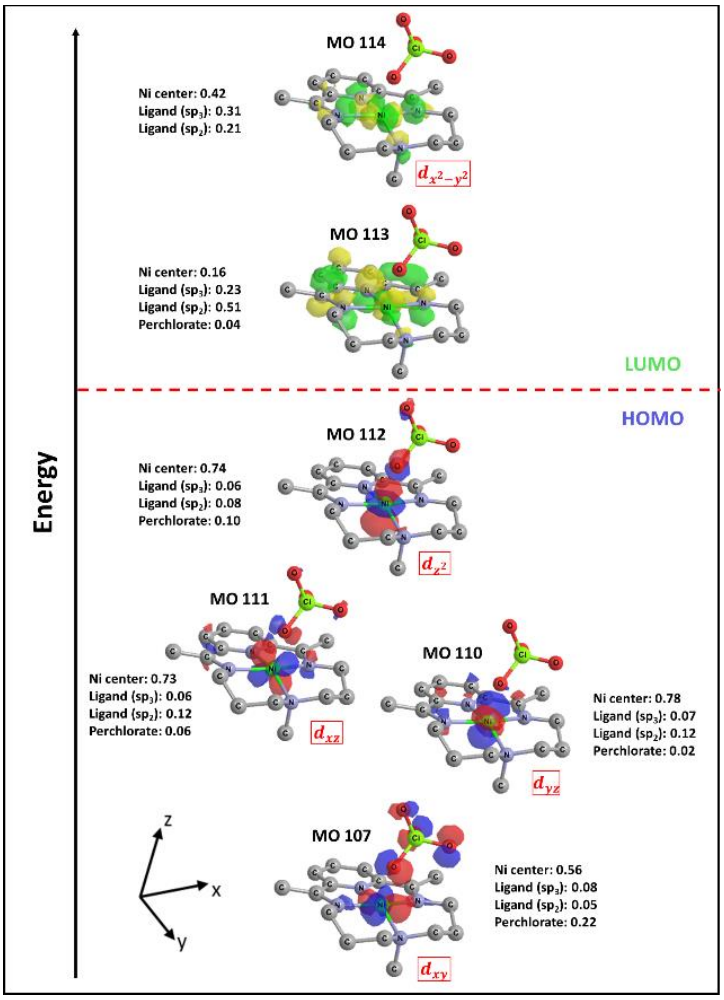

Figure 26: Selected molecular orbitals of complex **1** in water at the M06L level of theory with def2-TZVP basis set.

Further computations were performed on the complex without the bound perchlorate. Figure 26 displays some selected isosurface plots of the frontier molecular orbitals for the perchlorate-free complex containing significant d-orbital contribution. All d-orbitals expected in a square planar electron configuration are identified within the molecular orbitals (MOs) displayed in Figure 27, having minimal contributions from the surrounding ligand. In this figure the HOMO-1, HOMO-2, and HOMO-3 correspond with the d_{yz}, d_{xz}, and d_{xy} orbitals, respectively. The lowest occupied molecular orbital (LUMO) is composed mostly of p-orbitals on the pyridine portion of the ligand. The LUMO+1 contains contributions from the $d_{x^2-y^2}$ orbital. These calculations revealed the electron configuration to have a HOMO largely

consisting of the metal centered d_{z^2} orbital. Access to the ligand based LUMO upon subsequent reductions allows the ligand to act as a reservoir for the metal center, expanding the complexes' ability to stabilize multiple redox events, useful for electrocatalysis. [27]

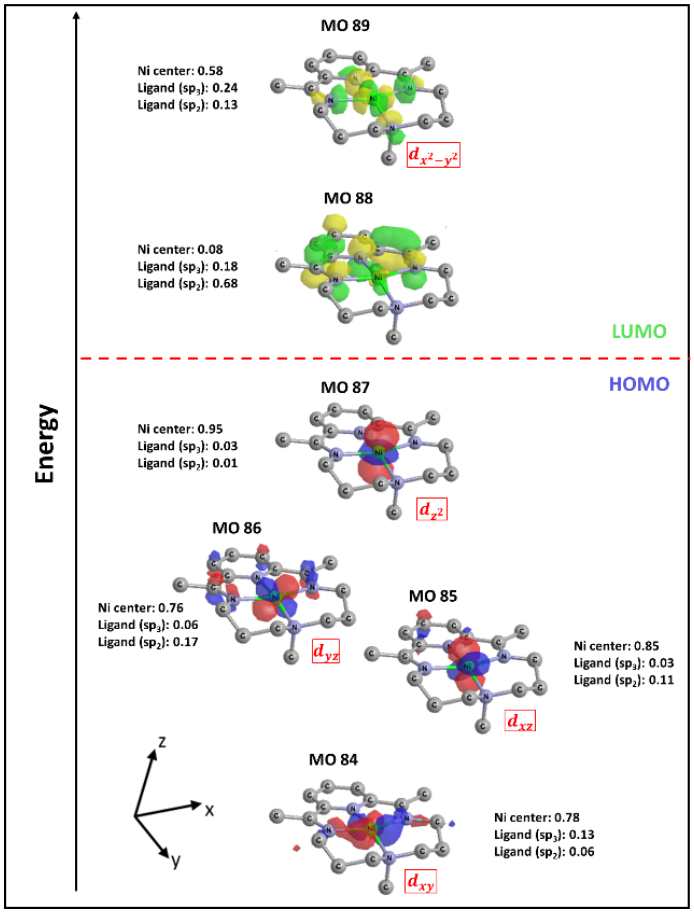

Figure 27: Selected molecular orbitals of complex 1 with perchlorate ligand removed in water at the M06L level of theory with def2-TZVP basis set.

Additional calculations were completed for the once- and twice-reduced complex and are shown in figures 28a and 28b. Isosurface plots for these species display a similar shape and vary only slightly in terms of MO contributions. The first two reductions displayed in Figure 6, the irreversible reductions at -0.89 V and -1.05 V, populate the MO largely consisting of π-orbitals on the pyridine portion of the ligand, as observed in Figures 25a and 25b. This MO also contains minimal contribution from the metal center, antibonding with d_{yz}. Addition of the first electron (Figure 28a), generates a doublet cation with 1+ charge. Adding another electron to the

configuration (Figure 28b), results in a neutral, singlet structure. The Ni-complex geometry for the simulated structures is largely unchanged through the subsequent reductions. MO88 (from Figures 28a and 28b) has a relative energy level between the d_{z^2} and $d_{x^2-y^2}$ orbitals that are expected in a square planar structure, ultimately preventing $d_{x^2-y^2}$ from becoming occupied and disfavouring a square planar geometry.

A) B)

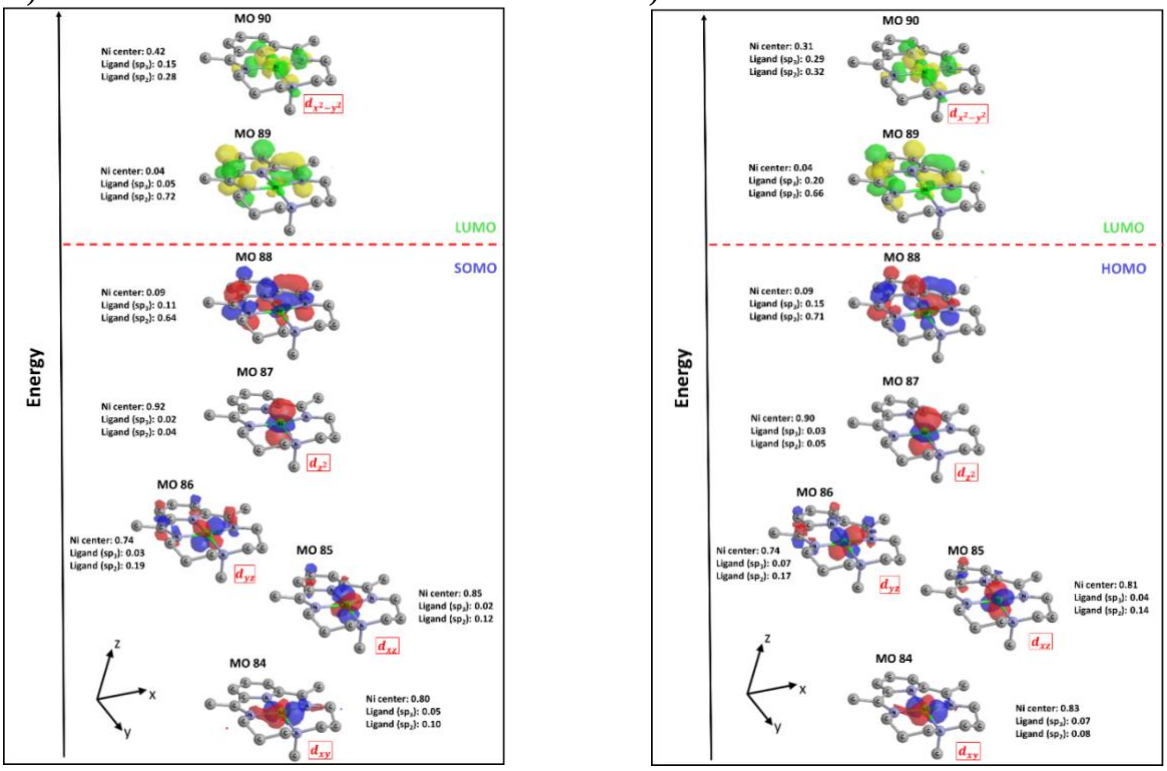

Figure 28: A) Selected molecular orbitals of complex 1 singly reduced with the perchlorate ligand removed in water at the M06L level of theory with def2-TZVP basis set. B) Selected molecular orbitals of complex 1 twice reduced with the perchlorate ligand removed in water at the M06L level of theory with def2-TZVP basis set.

The proposed NO_2^- reduction mechanism to form ammonium or hydroxylamine can be seen for **1** below in Figure 29. The figure was formed based on calculations, CPC experimental observations and results, and hypotheses made by other groups in the literature. Initially, as **1** is introduced to solution, the axial perchlorate ligand dissociates and opens a binding site to allow for NO_2^- to coordinate. Interestingly, M06L calculations suggest the NO_2^- binds through the N as opposed to binding through the two O atoms. To justify this, the Gibbs free energy was calculated, and the energy difference between coordination through the two O's vs coordination through the N is 2.30 kcal/mol. With such a small difference in energy, we can conclude that it is easily accessible to change from ONO coordination to coordination through the N. This is apparent when studying the mechanism, as all transformations occur while the N of NO_2^- is bound to the metal.

When the nitrite-bound complex is reduced, it reacts with water to be protonated. Interestingly, the redox-active pyridine ring accepts the first proton and subsequently acts as a proton shuttle for the remainder of the reduction reaction. Further reduction and protonation of the complex leads to the formation of a nitrosyl group (N=O) and the loss of H_2O. Ni-NO proceeds with an additional electron reduction and protonation to form Ni-HNO which is readily reduced by two electrons to form Ni-NH_2OH.

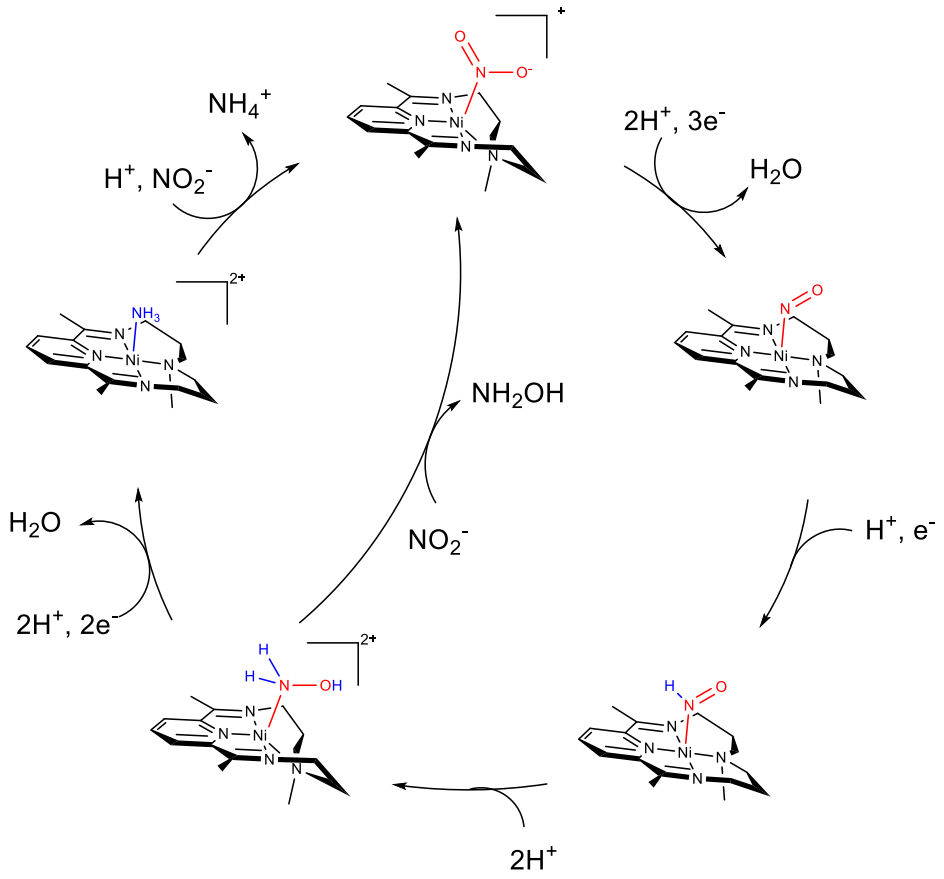

Figure 29: Proposed Electrocatalytic NO_2^- Reduction Mechanism by **1**. The second perchlorate anion is omitted for clarity. A more detailed proposed mechanism can be found in the Appendix.

From here the catalytic cycle either proceeds towards the formation of ammonia or branches off to have NH_2OH dissociate and restart the catalytic cycle. Proceeding with an additional reduction leads to the loss of a water and the formation of Ni-NH_3; afterwards NH_3 dissociates as the primary product. While in solution, NH_3 can receive a H^+ from H_2O and form the ammonium ion, NH_4^+, which is what is identified using 500 MHz ^{14}N NMR (Figure 30).

Conclusion and Future Work

To summarize this chapter, we prepared two nitrite-reducing catalysts 1 and 2a,b. When comparing between the two, 1 is capable of reducing NO_2^- to NH_4^+ and NH_2OH with a higher product yield and is capable of passing more charge over the course of 5 hrs. Both complexes have similar faradaic efficiencies, with both having high selectivity for the formation of NH_4^+ as

the primary product. Following bulk CPE measurements, calculations were conducted to propose a mechanism for the electrochemical reduction of NO_2^- by **1**. The calculations provided two distinct pathways which can be followed to show the formation of the two observed reaction products NH_2OH and NH_4^+. Calculations were also done to compare the experimental and computed bond lengths and angles for all complexes which were concluded to agree. For future work, more experiments should be conducted to determine the effects of varying pH in the system, and to optimize the faradaic efficiency of the reaction by troubleshooting the cause of the formation of nitrate in the reaction cell. The synthesis of reaction intermediates and using them for subsequent electrochemical bulk measurements to compare the results should also be explored to provide stronger evidence for the proposed mechanism.

Experimental:

General Methods

Reactions were performed using standard Schlenk techniques under a flow of N_2 gas. All solvents were sparged with nitrogen then dried by passage through a column of activated alumina using an apparatus purchased from Anhydrous Engineering. Deuterated solvents were dried using activated molecular sieves. All other chemicals were purchased from Sigma-Aldrich and used without further purification. Dried acetonitrile was purchased from Sigma-Aldrich and stored on molecular sieves in a glovebox.

Electrochemistry

All cyclic voltammetry experiments were carried out in a single compartment cell of approximately 50 mL volume under an atmosphere of dinitrogen. Samples were prepared in open-air, sealed, connected to a Schlenk line, and purged with a nitrogen atmosphere. Measurements were carried out using a VersaSTAT (Princeton Applied Research) potentiostat.

A conventional three electrode system was employed consisting of a glassy carbon electrode (diameter = 0.4 cm), used as the working electrode, a Pt wire, or a glassy carbon rod as the counter electrode, and an Ag/AgCl electrode was used as a reference electrode. For bulk electrocatalytic experiments, a glassy carbon rod (diameter = 0.4cm; length = 2cm) was used as the working electrode, a coiled Pt wire as the auxiliary electrode, referenced to Ag/AgCl electrode.

Calculations to determine whether a redox pair is reversible, quasi reversible or irreversible is shown below:

ΔE_p = anodic peak potential ($E_{p,a}$) – cathodic peak potential ($E_{p,c}$)

Reversible if $\Delta E_{p,rev}$ = 57/n mV where n = # of e^-

Quasireversible if $\Delta E_{p,rev} < \Delta E_{p,quasi} < 200/n$ mV

Irreversible if $\Delta E_{p,irrev} > 200/n$ mV

Computational Methods

Density functional theory (DFT) computations were performed on the nickel complex in water using the polarizable continuum model (PCM) at the M06L level of theory. Geometry optimization and vibrational frequency calculations were performed using def2-SVP as a basis set, followed by molecular energy computations with def2-TZVP. Atomic coordinates were obtained from its crystal structure, initially with a perchlorate bound in the apical position (Figure 1).

Complex Synthesis

Synthesis of **1**:

In a round bottom flask, 1.63 g (0.01 mol) of 2,6- diacetylpyridine was added to 140 mL of aqueous ethanol that contains 70 mL of ethanol. The solution was heated to 50℃ and stirred until

all the diacetyl dissolved. Then, 0.01 mol of $NiCl_2$ * 6 H_2O was added to the solution. The solution was mixed for 30 minutes with heating at 70℃. To the mixture, 0.01 mol of 3,3'-Diamino-N-methyldipropylamine is added followed by the addition of 0.8 mL of acetic acid. The mixture is stirred at 70℃ for 8 hours. The solvent was reduced by half on a rotary evaporator and left to cool to room temperature. The solution was cooled with an ice bath and 0.04 mol of LiClO4 was added and stirred for 2 hrs. The mixture was filtered on a sintered glass, washed with a minimum amount of ethanol followed by several washes with diethyl ether. The bright red powder was dried under vacuum and crystallized by layering a concentrated solution of **1** in acetonitrile with diethyl ether. Crystals of the **1**-NO_2 complex were grown by layering with an acetonitrile/water/diethyl ether solvent system. Crystals are purple in color and are shaped like needles.

Synthesis of **2**:

The synthesis of **2** is as described above however substituting $NiCl_26H_2O$ with $CoCl_26H_2O$. The violet-coloured powder was crystallized by dissolving the product in a minimum amount of hot distilled water and left to cool and evaporate off to leave deep red needles.

Product Identification & Quantification

Since the reaction solutions containing both **1** and **2a,b** are heavily coloured, the use of UV-Vis spectroscopy to identify and quantify the reaction products is not possible. We decided to pursue the use of ^{14}N NMR spectroscopy to identify ammonium (NH_4^+) and redox titration with $[K_3Fe(CN)_6]$ was done for NH_2OH consumption. A calibration curve (Figure 28) was made to quantify the amount of NH_4^+ by comparing peak areas of the external $MeNO_2$ standard with known concentrations of $[NH_4^+]$ compared to the peak area of a 1.0 M $MeNO_2$ standard in a capillary tube.

The reaction vessel was also tested for the formation of NO using the qualitative myoglobin test however no NO was seen to have been formed. GC-TCD also showed no formation of N_2 when CPE was performed under an inert argon atmosphere.

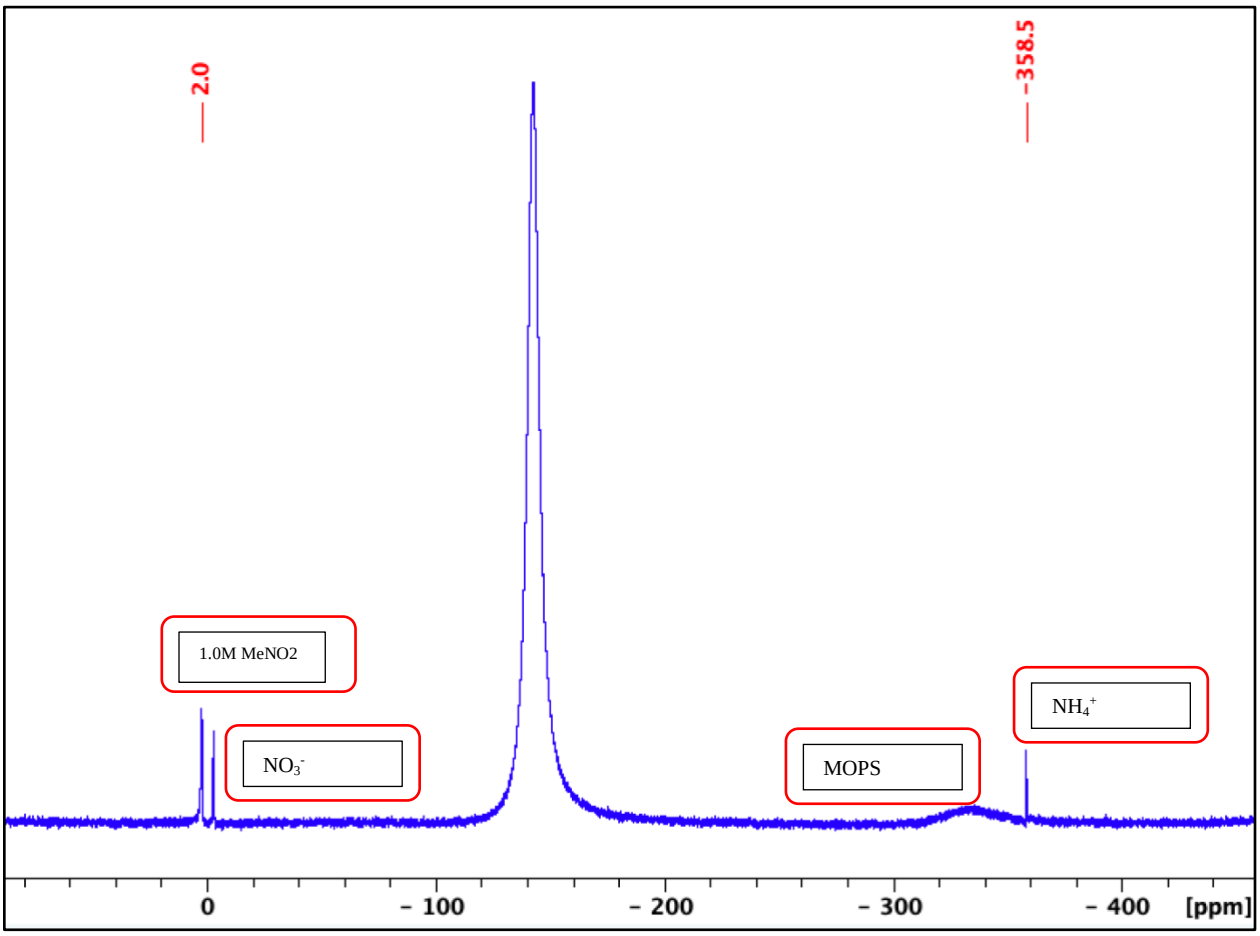

Figure 30: Nitrogen-14 NMR spectrum of a 0.5mL aliquot of the reaction solution and 0.2mL of acetonitrile-d3 with a 1.0M $MeNO_2$ external reference at 2.0ppm using a Bruker AVANCEIII 500MHz spectrometer with 600 scans. The broad peak at -330 ppm depicts the 1.0M MOPS buffer and the peak at -2.8 ppm depicts the nitrate anion (NO_3^-).

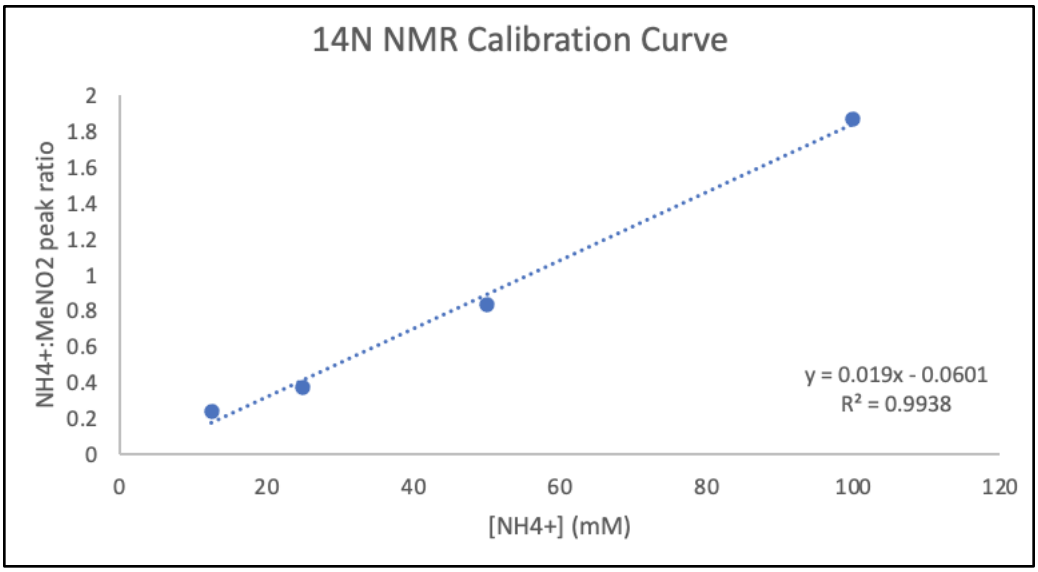

Figure 31: Calibration curve comparing peak areas of the external MeNO2 standard with known concentrations of [NH_4^+] compared to the peak area of a 1.0 M MeNO2 standard in a capillary tube.

References:

(1) Rafiqul, I.; Weber, C.; Lehmann, B.; Voss, A. Energy Efficiency Improvements in Ammonia Production—Perspectives and Uncertainties. *Energy* **2005**, *30* (13), 2487–2504. https://doi.org/10.1016/j.energy.2004.12.004.

(2) Schlögl, R. Catalytic Synthesis of Ammonia—A "Never-Ending Story"? *Angew. Chem. Int. Ed.* **2003**, *42* (18), 2004–2008. https://doi.org/10.1002/anie.200301553.

(3) Zeng, Y.; Priest, C.; Wang, G.; Wu, G. Restoring the Nitrogen Cycle by Electrochemical Reduction of Nitrate: Progress and Prospects. *Small Methods* **2020**, *4* (12), 2000672. https://doi.org/10.1002/smtd.202000672.
(4)Galloway, J. N.; Townsend, A. R.; Erisman, J. W.; Bekunda, M.; Cai, Z.; Freney, J. R.; Martinelli, L. A.; Seitzinger, S. P.; Sutton, M. A. Transformation of the Nitrogen Cycle: Recent Trends, Questions, and Potential Solutions. *Science* **2008**, *320* (5878), 889–892. https://doi.org/10.1126/science.1136674.

(5) Zhang, X.; Wang, Y.; Wang, Y.; Guo, Y.; Xie, X.; Yu, Y.; Zhang, B. Recent Advances in Electrocatalytic Nitrite Reduction. *Chem. Commun.* **2022**, *58* (17), 2777–2787. https://doi.org/10.1039/D1CC06690K.

(6) Xu, S.; Ashley, D. C.; Kwon, H.-Y.; Ware, G. R.; Chen, C.-H.; Losovyj, Y.; Gao, X.; Jakubikova, E.; Smith, J. M. A Flexible, Redox-Active Macrocycle Enables the Electrocatalytic Reduction of Nitrate to Ammonia by a Cobalt Complex. *Chem. Sci.* **2018**, *9* (22), 4950–4958. https://doi.org/10.1039/C8SC00721G.

(7) Stroka, J. R.; Kandemir, B.; Matson, E. M.; Bren, K. L. Electrocatalytic Multielectron Nitrite Reduction in Water by an Iron Complex. *ACS Catal.* **2020**, *10* (23), 13968–13972. https://doi.org/10.1021/acscatal.0c03600.

(8) Guo, Y.; Stroka, J. R.; Kandemir, B.; Dickerson, C. E.; Bren, K. L. Cobalt Metallopeptide Electrocatalyst for the Selective Reduction of Nitrite to Ammonium. *J. Am. Chem. Soc.* **2018**, *140* (49), 16888–16892. https://doi.org/10.1021/jacs.8b09612.

(9) Park, Y. J.; Peñas-Defrutos, M. N.; Drummond, M. J.; Gordon, Z.; Kelly, O. R.; Garvey, I. J.; Gullett, K. L.; García-Melchor, M.; Fout, A. R. Secondary Coordination Sphere Influences the Formation of Fe(III)-O or Fe(III)-OH in Nitrite Reduction: A Synthetic and Computational Study. *Inorg. Chem.* **2022**, *61* (21), 8182–8192. https://doi.org/10.1021/acs.inorgchem.2c00462.

(10) Partovi, S.; Xiong, Z.; Kulesa, K. M.; Smith, J. M. Electrocatalytic Reduction of Nitrogen Oxyanions with a Redox-Active Cobalt Macrocycle Complex. *Inorg. Chem.* **2022**, *61* (24), 9034–9039. https://doi.org/10.1021/acs.inorgchem.2c00199.

(11) Taniguchi, L.; Nakashima, N.; Yasukouchi, K. Reduction of Nitrate to Give Hydroxylamine at a Mercury Electrode Using Cobalt(III)–and Nickel(II)–Cyclams as Catalysts. *J. Chem. Soc., Chem. Commun.* **1986**, No. 24, 1814–1815. https://doi.org/10.1039/C39860001814.

(12) Knijnenburg, Q.; Gambarotta, S.; Budzelaar, P. H. M. Ligand-Centred Reactivity in Diiminepyridine Complexes. *Dalton Trans.* **2006**, No. 46, 5442–5448. https://doi.org/10.1039/B612251E.

(13) Reardon, D.; Conan, F.; Gambarotta, S.; Yap, G.; Wang, Q. Life and Death of an Active Ethylene Polymerization Catalyst. Ligand Involvement in Catalyst Activation and Deactivation. Isolation and Characterization of Two Unprecedented Neutral and Anionic Vanadium(I) Alkyls. *J. Am. Chem. Soc.* **1999**, *121* (40), 9318–9325. https://doi.org/10.1021/ja990263x.

(14) Enright, D.; Gambarotta, S.; Yap, G. P. A.; Budzelaar, P. H. M. The Ability of the α,A′-Diiminopyridine Ligand System to Accept Negative Charge: Isolation of Paramagnetic and Diamagnetic Trianions. *Angew. Chem. Int. Ed.***2002**, *41* (20), 3873–3876. https://doi.org/10.1002/1521-3773(20021018)41:20<3873::AID-ANIE3873>3.0.CO;2-8.

(15) Flisak, Z.; Sun, W.-H. Progression of Diiminopyridines: From Single Application to Catalytic Versatility. *ACS Catal.* **2015**, *5* (8), 4713–4724. https://doi.org/10.1021/acscatal.5b00820.

(16) Norouziyanlakvan, S.; Ferguson, J.; Richeson, D. Electrocatalytic Hydrogen Production from Neutral Water Using an Aqueous Ni(II) Pincer Complex. *Catal. Sci. Technol.* **2022**, *12* (24), 7494–7500. https://doi.org/10.1039/D2CY01504H.

(17) Hojilla Atienza, C. C.; Tondreau, A. M.; Weller, K. J.; Lewis, K. M.; Cruse, R. W.; Nye, S. A.; Boyer, J. L.; Delis, J. G. P.; Chirik, P. J. High-Selectivity Bis(Imino)Pyridine Iron Catalysts

for the Hydrosilylation of 1,2,4-Trivinylcyclohexane. *ACS Catal.* **2012**, *2* (10), 2169–2172. https://doi.org/10.1021/cs300584b.

(18) Bianchini, C.; Giambastiani, G.; Rios, I. G.; Mantovani, G.; Meli, A.; Segarra, A. M. Ethylene Oligomerization, Homopolymerization and Copolymerization by Iron and Cobalt Catalysts with 2,6-(Bis-Organylimino)Pyridyl Ligands. *Coordination Chemistry Reviews* **2006**, *250* (11–12), 1391–1418. https://doi.org/10.1016/j.ccr.2005.12.018.

(19) Nakayama, Y.; Maeda, N.; Shiono, T. Synthesis of Bis(Imino)Pyridine Complexes of Group 5 Metals and Their Catalysis for Polymerization of Ethylene and Norbornene. **2006**, *161*, 165–170. https://doi.org/10.1016/S0167-2991(06)80449-0.

(20) Cámpora, J.; Naz, A. M.; Palma, P.; Álvarez, E.; Reyes, M. L. 2,6-Diiminopyridine Iron(II) Dialkyl Complexes. Interaction with Aluminum Alkyls and Ethylene Polymerization Catalysis. *Organometallics* **2005**, *24* (21), 4878–4881. https://doi.org/10.1021/om050645d.

(21) Fabbrizzi, L.; Poggi, A. Tetra-Aza Macrocycles Containing a Pyridine Ring. The Oxidation and Reduction Behavior of Their Nickel(II) Complexes. *Inorganica Chimica Acta* **1980**, *39*, 207–210. https://doi.org/10.1016/S0020-1693(00)93656-9.

(22) Karn, J. L.; Busch, D. H. Nickel(II) Complexes of the New Macrocyclic Ligands Meso- and (+-)-2,12-Dimethyl-3,7,11,17-Tetraazabicyclo [11.3.1] Heptadeca-1(17),13,15-Triene. *Inorg. Chem.* **1969**, *8* (5), 1149–1153. https://doi.org/10.1021/ic50075a025.

(23) Poon, C.-K.; Wan, W.-K.; Liao, S. S. T. Structural and Mechanistic Studies of Co-Ordination Compounds. Part 17. Preparation and Acid Hydrolysis of Some Cobalt(III) Complexes Containing the Quadridentate Macrocycle 2,7,12-Trimethyl-3,7,11,17-Tetra-Azabicyclo[11.3.1] Heptadeca-1 (17),2,11,13,15-Pentaene: An Extra-Ordinary Hydrolysis Reaction. *J. Chem. Soc., Dalton Trans.* **1977**, No. 13, 1247–1251. https://doi.org/10.1039/DT9770001247.

(24) Einsle, O.; Messerschmidt, A.; Huber, R.; Kroneck, P. M. H.; Neese, F. Mechanism of the Six-Electron Reduction of Nitrite to Ammonia by Cytochrome *c* Nitrite Reductase. *J. Am. Chem. Soc.* **2002**, *124* (39), 11737–11745. https://doi.org/10.1021/ja0206487.

(25) Minenkov, Y.; Singstad, Å.; Occhipinti, G.; Jensen, V. R. The Accuracy of DFT-Optimized Geometries of Functional Transition Metal Compounds: A Validation Study of Catalysts for Olefin Metathesis and Other Reactions in the Homogeneous Phase. *Dalton Trans.* **2012**, *41* (18), 5526–5541. https://doi.org/10.1039/C2DT12232D.

(26) Elsby, M. R.; Kim, S. Y. H.; Steinmann, S. N.; Baker, R. T. Same Ligand, Three First-Row Metals: Comparing M-Amido Bifunctional Reactivity (Mn, Fe, Co). *Dalton Trans.* **2021**, *50* (41), 14542–14546. https://doi.org/10.1039/D1DT02637B.

(27) Berro, P.; Norouziyanlakvan, S.; Rao, G. K.; Gabidullin, B.; Richeson, D. Electrocatalytic Reduction of CO_2 to CO and HCO_2^- with Zn(II) Complexes Displaying Cooperative Ligand Reduction. *Chem. Commun.* **2021**, *57*(73), 9292–9295. https://doi.org/10.1039/D1CC03887G.

Appendix:

Table 7: Crystal Structure Data for **1**, **1-NO2**, and **2ab**.

	1	**1-NO2**	**2a,b**
Empirical formula	$C_{16}H_{24}Cl_2N_4NiO_8$	$C_{18}H_{27}ClN_6NiO_6$	$C_{16}H_{25.5}Cl_2CoN_4O_5$
Formula weight ($g \cdot mol^{-1}$)	530.00	517.61	483.73
Crystal system	orthorhombic	triclinic	monoclinic
Space group	$P\ n\ a\ 2_1$	$P\ \bar{1}$	$P\ 2_1/c$
a (A)	12.0427(5)	7.4118(4)	7.2183(2)
b (A)	13.9944(5)	12.5556(6)	20.4087(6)
c (A)	12.7175(5)	13.0820(7)	14.2211(4)
α (deg)	90	69.969(1)	90
β (deg)	90	81.164(1)	102.084(1)
γ (deg)	90	87.146(1)	90
V (A^3)	2143.28(14)	1130.18(10)	2048.58(10)
Z	4	2	4
T (K)	200(2)	200(2)	295(2)
ρ_{calcd} ($g \cdot cm^{-3}$)	1.643	1.521	1.568
μ (mm^{-1})	1.206	1.024	1.134
$2\theta_{max}$ (deg)	61.066	56.882	55.050
Total/unique reflections	11614/5524	16793/5678	15734/4694
Reflections [$I_o \geq 2\sigma(I_o)$]	4058	4608	3734
R_1, wR_2 [$I_o \geq 2\sigma(I_o)$]	0.0426, 0.0834	0.0454, 0.1225	0.0380, 0.0940
Goodness of fit	1.019	1.068	1.037

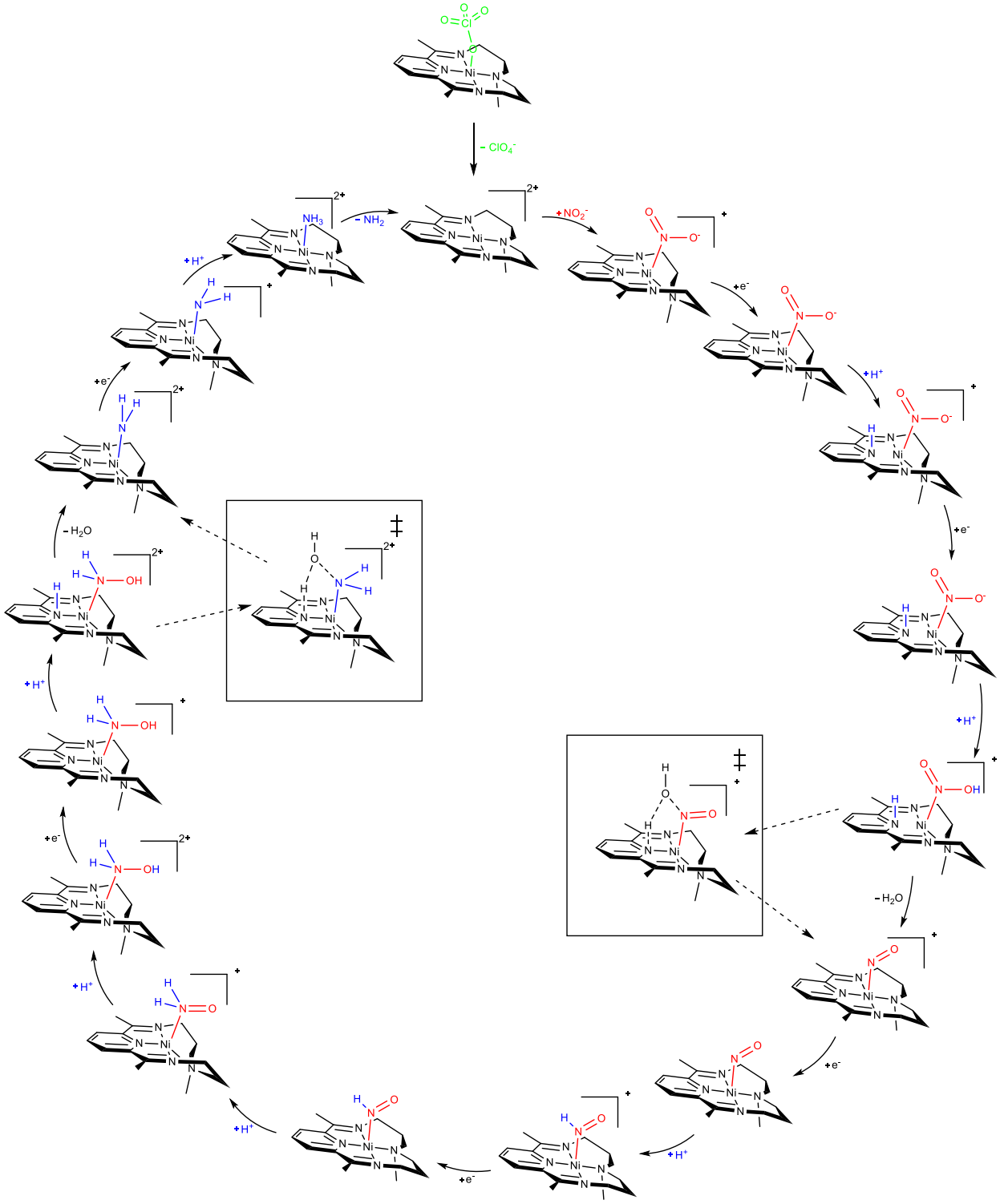

Figure 32: Detailed Proposed NO_2^- Reduction Mechanism by **1**.

Chapter 5: Thesis Conclusions

This thesis investigated three broadly targeted area of electrocatalysis using earth abundant metals as the catalyst center to promote sustainability. Chapter 2 focused on the reduction of CO_2 gas to value-added products and attempted to develop a new electrophotocatalytic system using a known Mn(I) electrocatalyst with a photocatalyst integrated into its alpha-diimine ligand. We synthesized the MnPhenNI complex, and attempted to exploit the use of tandem photoexcitation and electrochemical reduction of the integrated photocatalyst. The MnPhenNI complex was found to produce miniscule amounts of H_2 under blue light and subsequent electrochemical reduction. Unfortunately, the complex was found to degrade in the presence of UV light which is where the integrated photocatalyst absorbs light, indicating to us that the selected Mn(I) metal center should have been replaced with a different metal. The structure of the MnPhenNI complex was characterized by ^{1}H NMR and UV-Vis.

While the project highlighted in chapter 2 failed, there is room for improvement in the methods and catalyst design. Further investigation into the use of a more robust and well-established complex, such as one using a rhenium(I) complex highlighted by Castellano et al., or the recently published Cu(I) photosensitizer complex by Tschierlei et al. would be an avenue worth pursuing.[1,2] Also, utilization of spectroelectrochemistry to study the effect of the reduced complex prior to photoexcitation would bring valuable insight into any structural or electronic changes that may occur during experimentation.

In chapter 3, the focus was on the production of H_2 from water, which showcased a Ni(II) pincer complex capable of reducing water in the presence of phosphate buffer. The complex was fully characterized electrochemically and by SC-XRD. Under ideal conditions the complex was able to produce H_2 with a faradaic efficiency of 96%. DFT calculations were also performed

which gave valuable insight into the HER mechanism. Further work on this project could include pH studies, investigation into the use of other buffers and substrates, and CPC measurements using trifluoroacetic acid.

With the importance and popularity of the redox-active diiminopyridine ligand scaffolds, chapter 4 reintroduced them in the form of simple macrocycles with inspiration from the water-soluble, hydrogen generating complex from chapter 3. In chapter 4, the reduction of nitrite to useful chemical building blocks was investigated. The synthesis of two simple macrocycles with a Ni(II) and Co(II) center were electrochemically, and structurally characterized by SC-XRD. CPC experiments were performed and both catalysts showed selectivity towards ammonium as the primary product with hydroxylamine as the secondary product. DFT calculations were conducted and a proposed electrocatalytic reduction mechanism was presented to aid in the understanding of the various transformations that occur from nitrite to ammonium.

Advancements to be made in this project could include further investigation into the reactivity of the complexes highlighted in chapter 4 under different conditions such as varied pH, time, and varied catalyst concentration would shed light on the kinetics and reactivity of these catalysts. Furthermore, additional modification of these simple macrocycles with different substituents on the pyridine ring, and the N-methyl would provide potentially interesting interactions and routes for reaction optimization and selectivity alterations. Finally, the chemical synthesis and isolation of reaction intermediates such as the Ni-NH_2OH, Ni-HNO, Ni-NO, and Ni-NH_3 complexes by use of strong reducing agents would help further the understanding in the nitrite reduction mechanism.

References:

(1) Yarnell, J. E.; Deaton, J. C.; McCusker, C. E.; Castellano, F. N. Bidirectional “Ping-Pong” Energy Transfer and 3000-Fold Lifetime Enhancement in a Re(I) Charge Transfer Complex. *Inorg. Chem.* **2011**, *50* (16), 7820–7830. https://doi.org/10.1021/ic200974h.

(2) Yang, Y.; Doettinger, F.; Kleeberg, C.; Frey, W.; Karnahl, M.; Tschierlei, S. How the Way a Naphthalimide Unit Is Implemented Affects the Photophysical and -Catalytic Properties of Cu(I) Photosensitizers. *Front. Chem.* **2022**, *10*, 936863. https://doi.org/10.3389/fchem.2022.936863.